DISS. ETH No. 29401

Towards Multi-Material Strain and Crystal Orientation Mapping with Scanning Reflectance Anisotropy Microscopy

A thesis submitted to attain the degree of

DOCTOR OF SCIENCES of ETH ZURICH
(Dr. sc. ETH Zurich)

presented by

Joan Sendra Garcia

M. Sc. in Physics, ETH Zurich
born on 20.03.1993
citizen of Barcelona

accepted on the recommendation of:

Prof. Dr. Ralph Spolenak, examiner
Prof. Dr. Rachel Grange, co-examiner
Prof. Dr. Peter Zeppenfeld, co-examiner

2023

This document was typeset with the help of KOMA-Script and LaTeX using the kaobook class.

Published
First printed in June 2023.

An expert is a person who has made all the mistakes that can be made in a very narrow field.

– Niels Bohr

Acknowledgements

The completion of this PhD thesis is the culmination of the combined efforts and support of numerous people, to whom I owe immense gratitude.

First and foremost, I would like to thank Prof. Ralph Spolenak for giving me the opportunity to work in the Laboratory for Nanometallurgy group (LNM). Throughout these years he has provided guidance, unwavering support and endless ideas while simultaneously providing me with the freedom to choose my own paths. I am very grateful for his supervision, which has been key in defining the scientist I am today.

I extend heartfelt thanks to Prof. Peter Zeppenfeld and Prof. Rachel Grange for taking the time to take part in the thesis defense committee and reviewing my work. Their insightful feedback and constructive critique significantly enhanced the quality of this work.

Many thanks to the RAS subgroup – Micha, Marco, Henning, Ralph and students – and the breakfast club – Jose, Jelena, Fabian, Henning and students – for all the discussions that helped me face the countless challenges (really, way too many!) that arose during this work. Special thanks to Micha and Henning for all the mentoring and long discussions that provided invaluable help, without which it would not have been possible to carry out this PhD.

During my time at LNM I had the chance to work with many students. I would like to thank them and the contributions of the students I supervised, Nerea, Fabian Bill, Alexandre and Fabian Haake, which were essential for the achievements of this work. I am also very proud that Nerea and Fabian Haake went on to start a PhD at LNM and wish them the best of times. I would also like to thank all the support in the lab from Bea, Fabio, Till and Hansjakob that made this work possible.

I have had a wonderful time at LNM thanks to all its present and past members. The atmosphere in the lab has made this journey really special and I am glad to leave with many close friends. From events like ski retreats, conferences with rocky starts (and cancelled cities), pub quizzes and crazy DnD sessions to regular coffees and Coop rounds, I couldn't have asked for a better group. Many thanks to my officemates (including the blinds servant) for putting up with me. Many thanks to Carmen and Jelena for your support and listening to my rants all these years.

Last but not least, I want to give my thanks to my family, for which I am deeply grateful. Their continuous support has been the cornerstone of my journey, without which this achievement would not have been possible.

Abstract

Recent years have seen a growth in the fields of flexible electronics and MEMS. Due to their low power consumption and versatility, these technologies are increasingly being used in a wide range of applications, *e.g.* from biomedical to motion sensing in smartphones. Nonetheless, the multi-material components used in these devices and the mechanical demands they face pose significant challenges for their performance and reliability, increasing the need for mechanical characterization techniques. Moreover, the prevalence of strain engineering in semiconductor systems, due to its inherent enhancement of optical and electronic properties, has also made mechanical characterization a must in the design process of industrial semiconducting technologies.

The most commonly employed non-destructive strain mapping techniques, based on electron microscopy, x-ray diffraction or Raman spectroscopy, can provide high resolution and strain sensitivity. However, they are most often limited to specific materials or a significant resource investment. Instead, reflectance anisotropy spectroscopy (RAS) is an optical technique that offers multi-material class strain sensitivity, even higher than the aforementioned techniques. By measuring the reflectance difference along two orthogonal directions, RAS is able to acquire the near-normal incidence ellipsometric response of the sample, which is related to elastic strain by means of the elasto-optic effect. This thesis demonstrates the capabilities of an RAS microscope, termed scanning reflectance anisotropy microscopy (SRAM), that builds upon previously proposed microscopy setups in the literature achieving diffraction-limited resolution and high strain sensitivity as a multi-material platform.

Strain sensitivity is demonstrated for different material classes, including metals (gold) and semiconductors (crystalline and amorphous germanium), measuring the gold's average elasto-optic constant to be $\overline{P} = 0.18 - 0.30i$. SRAM achieves a strain sensitivity of up to 10^{-4} with sub-micron resolution. This is demonstrated by analyzing complex strain distributions, created by externally straining milled structures on thin films, and comparing to FEM simulations. Furthermore, SRAM is also a highly phase sensitive technique, with phase sensitivities of up to $4.7 \cdot 10^{-3}$ degrees, and can provide phase maps of, for example, metasurfaces. Plasmonic slot nanoantennas are employed as a model system to study symmetry breaking with dipolar transitions, achieving a strain sensitivity of $\kappa = -20.9$ meV/% and opening the door for strain markers in future studies. Furthermore, the influence of roughness

and crystal orientation on the SRAM signal is investigated. It is found that roughness is the main limiting factor of the sensitivity of the technique and strategies for circumventing such limitation are provided. Preliminary results also indicate a strong influence of crystal orientation, which could result in crystal orientation mapping with further research.

In summary, the versatility of SRAM to study the breaking of the lattice symmetry by simple reflectance measurements opens up the possibility to carry out non-destructive mechanical and optical characterization of multi-material components, such as wearable electronics and semiconductor devices. SRAM provides an additional strain mapping technique that can cover some of the limitations of traditional strain mapping techniques.

Zusammenfassung

In den letzten Jahren haben die Bereiche flexible Elektronik und MEMS einen grossen Aufschwung erlebt. Aufgrund ihres geringen Stromverbrauchs und ihrer Vielseitigkeit kommen diese Technologien in vielen Anwendungen unseres Alltags zum Einsatz, z. B. in der Biomedizin oder zur Bewegungserfassung in Smartphones. Die in diesen Geräten verwendeten Komponenten bestehen aus mehreren Materialien und sind des Gebrauchs mechanischer Belastung ausgesetzt. Dies stellt eine grosse Herausforderung für ihre Leistung und Zuverlässigkeit dar, was den Bedarf an mechanischen Charakterisierungsverfahren erhöht. Darüber hinaus ist die mechanische Charakterisierung ein Muss im Designprozess industrieller Halbleitertechnologien, denn Dehnung wird in diesen Materialien gezielt herbeigeführt, um eine Verbesserung der optischen und elektronischen Eigenschaften zu erreichen.

Die gebräuchlichsten zerstörungsfreien Dehnungsmessverfahren, die auf Elektronenmikroskopie, Röntgenbeugung oder Raman-Spektroskopie basieren, bieten eine hohe Auflösung und Sensitivität gegenüber Dehnungen. Sie sind jedoch meist auf bestimmte Materialien beschränkt oder erfordern einen erheblichen Ressourceneinsatz. Stattdessen ist die Reflexionsanisotropie-Spektroskopie (RAS) ein optisches Verfahren, das eine höhere Dehnungssensivität für mehrere Materialklassen bietet als die vorhergenannten Methoden. Durch die Messung der Reflexionsdifferenz entlang zweier orthogonaler Richtungen kann die RAS die ellipsometrische Antwort der Probe bei nahezu normalem Einfall erfassen. Das RAS Signal wird durch den elasto-optischen Effekt mit der elastischen Dehnung in Verbindung gebracht. In dieser Arbeit werden die Fähigkeiten eines RAS-Mikroskops, der so genannten Raster-Reflexions-Anisotropie-Mikroskopie (SRAM), demonstriert, das auf zuvor in der Literatur vorgeschlagenen Mikroskopie-Setups aufbaut und eine beugungsbegrenzte Auflösung sowie eine hohe Dehnungsempfindlichkeit als Multimaterial-Plattform erreicht.

Die Dehnungssensibilität wird für verschiedene Materialklassen nachgewiesen, darunter Metalle (Gold) und Halbleiter (kristallines und amorphes Germanium), wobei die durchschnittliche elasto-optische Konstante von Gold mit $\overline{P} = 0.18 - 0.30i$ gemessen wird. SRAM erreicht eine Dehnungsempfindlichkeit von bis zu 10^{-4} mit einer Auflösung im Submikrometerbereich. Dies wird durch die Analyse komplexer Dehnungsverteilungen demonstriert, die durch externe Dehnungen von gefrästen Strukturen auf dünnen Schichten

entstehen, und durch den Vergleich mit FEM-Simulationen bestätigt. Darüber hinaus ist SRAM auch eine hochgradig phasenempfindliche Technik mit einer Phasenempfindlichkeit von bis zu $4.7 \cdot 10^{-3}$ Grad und kann Phasenkarten z. B. von Metaoberflächen liefern. Plasmonische Schlitz-Nanoantennen werden als Modellsystem zur Untersuchung von Symmetriebrechungen bei dipolaren Übergängen eingesetzt, wobei eine Dehnungsempfindlichkeit von $\kappa = -20.9$ meV/% erreicht wird und dadurch die Tür für materialunabhängige Dehnungsmarker in zukünftigen Studien öffnet. Darüber hinaus wird der Einfluss von Rauheit und Kristallorientierung auf das SRAM-Signal untersucht. Es zeigt sich, dass die Rauheit der wichtigste begrenzende Faktor für die Empfindlichkeit der Technik ist, und es werden Strategien zur Umgehung dieser Beschränkung vorgestellt. Vorläufige Ergebnisse deuten auch auf einen starken Einfluss der Kristallorientierung hin, was bei weiteren Forschungen zu einer Kartierung der Kristallorientierung führen könnte.

Zusammenfassend lässt sich sagen, dass die Vielseitigkeit von SRAM zur Untersuchung des Bruchs der Gittersymmetrie durch einfache Reflexionsmessungen die Möglichkeit eröffnet, eine zerstörungsfreie mechanische und optische Charakterisierung von Komponenten aus mehreren Materialien durchzuführen, wie z. B. tragbare Elektronik- und Halbleitergeräte. SRAM bietet eine zusätzliche Dehnungsabbildungstechnik, die einige der Einschränkungen herkömmlicher Methoden ausgleichen und ergänzen kann.

Contents

Acknowledgements **v**

Abstract **vii**

Zusammenfassung **ix**

Contents **xi**

1 Introduction **1**
- 1.1 Motivation . . . 1
- 1.2 Aim of the thesis . . . 2
- 1.3 Reader's guide . . . 3

2 Theory **5**
- 2.1 Principles of RAS . . . 5
- 2.2 Strain sensitivity of RAS . . . 7
- 2.3 Strain sensitivity of Raman spectroscopy . . . 10
- 2.4 Plasmonic nanoantennas . . . 11
  - 2.4.1 Babinet's reciprocity principle . . . 13

3 Materials and methods **15**
- 3.1 Sample procedures . . . 15
- 3.2 Analysis . . . 16

4 Principles of SRAM **19**
- 4.1 Review of spatially resolved RAS techniques . . . 19
  - 4.1.1 Existing μRAS setups . . . 20
- 4.2 Scanning Reflectance Anisotropy Microscopy . . . 24
  - 4.2.1 Design . . . 25
  - 4.2.2 Sensitivity . . . 27
  - 4.2.3 Resolution . . . 30
- 4.3 Influence of sample topography . . . 32
  - 4.3.1 Film edges . . . 32
  - 4.3.2 Roughness . . . 37

5 Strain sensing **41**
- 5.1 Strain sensing with RAS . . . 41

5.2 Crystalline semiconductors . . . 44
5.2.1 Strain Sensitivity . . . 44
5.2.2 Strain Mapping . . . 46
5.3 Metals . . . 48
5.3.1 Strain Sensitivity . . . 48
5.3.2 Strain mapping . . . 50
5.4 Amorphous semiconductors . . . 52
5.4.1 Strain Sensitivity . . . 52
5.4.2 Strain Mapping . . . 54

6 Characterization of Nanoantennas 57
6.1 RAS on nanoresonators . . . 57
6.2 Design . . . 60
6.3 Nanoantenna characterization with SRAM . . . 61
6.3.1 Array size sensitivity . . . 63
6.4 Strain markers . . . 66
6.5 SRAM as a phase characterization technique . . . 68

7 Crystal orientation 71
7.1 RAS on Copper . . . 71
7.2 Influence of crystal orientation on RAS . . . 76
7.2.1 Single crystal measurements . . . 76
7.2.2 Out of plane rotation . . . 78
7.2.3 In-plane rotation . . . 81
7.3 Grain mapping with SRAM . . . 84
7.3.1 Unstrained copper plate . . . 84
7.3.2 Strained thin films . . . 86

8 General discussion 89
8.1 Main findings . . . 89
8.2 On-going issues . . . 94
8.3 Outlook . . . 96
8.4 Conclusions . . . 98

APPENDIX 101

A RAS signal derivation 103

References 107

Declaration 125

List of Abbreviations 127

List of Figures 129

Introduction 1

1.1 Motivation

1.1 Motivation 1
1.2 Aim of the thesis . 2
1.3 Reader's guide . . . 3

In October of 1950, Bardeen and Shockley published their seminal work on deformation-potential theory that, for the first time, linked strain-induced shifts at the band edge to the strain tensor [1]. This fundamental work, soon validated experimentally for uniaxially stressed silicon [2], introduced a new field in solid state physics: strain-engineering [3].

Today, strain-engineering enables the enhancement of the optoelectronic properties of semiconductor materials, e.g. increasing photoluminescence [4, 5], absorption [6], photo [7] and electrocatalysis [8], and carrier mobility [9] among others. Furthermore, elastic strain is applied to improve magnetic [10] properties or even raise the transition temperature of superconducting and ferroelectric materials [11].

Strain-engineering, which also implies accurate strain control, is particularly important in the field of flexible and wearable electronics [12, 13] and micro electro-mechanical systems [14]. These systems, often used in health care and monitoring devices, comprise a wide range of materials with very different mechanical properties, including polymers, metals and semiconductors, while having to perform under harsh mechanical deformation conditions [15, 16]. The requirement to withstand such conditions has made strain-engineering a critical point in the design process of such complex electro-mechanical devices, thus making mechanical and failure analysis of the utmost importance.

However, current non-destructive strain analysis techniques require a lot of resources, such as time, funds and special equipment, and are often limited to a single class of materials. For example, synchrotron x-ray diffraction offers high resolution and strain sensitivity but requires beam time. Raman spectroscopy is a popular vibrational spectroscopic technique for standard semiconductors but is not suitable for strain measurements on metallic or Raman inactive samples.

Classical reflectance anisotropy spectroscopy (RAS) is a near-normal incidence ellipsometric technique that measures the normalized difference of Fresnel coefficients along two orthogonal directions (equation 1.1, able to directly probe anisotropy of the band structure at optical frequencies [17–19]. With its high sensitivity, reflectance differences down to $\Delta r/r \sim 10^{-5}$ can be measured, RAS is especially suited to detect breaking of the lattice symmetry due to strain [20–23] or crystal orientation. As such, RAS is sensitive to strain in crystalline materials, *e.g.* semiconductors and metals, as well as polymers [24] as long as their resonances are within the range of the RAS setup. In particular, when measuring the yield strength of ultra-thin films, RAS has proved itself to complement x-ray diffraction due to its smaller probing volume, offering higher signal to noise ratio for a 50 nm thick film, and faster acquisition times, allowing higher strain rates [25].

$$\frac{\Delta r}{r} = 2\frac{r_x - r_y}{r_x + r_y}. \tag{1.1}$$

Despite the promising potential, classical RAS is fundamentally limited due to its low spatial resolution. Typical setups exhibit a probing spot of a couple of millimetres as increasing the angle of incidence for focusing poses problems due to the high polarization sensitivity of the technique [26, 27]. To compensate this short-coming, various setups have been proposed [28–32] but the remarkable potential of this technique as versatile multi-material platform for strain mapping remains unexplored.

1.2 Aim of the thesis

Figure 1.1 displays the schematic of the new RAS microscope proposed in this thesis based on the use of a supercontinuum laser, which would allow to achieve diffraction-limited resolution while simultaneously providing broad spectral bandwidth. The aim of this thesis is to advance the capabilities of scanning reflectance anisotropy microscopy (SRAM) and develop the technique as a powerful tool for material characterization and strain mapping, enabling the characterization of strain distributions in complex material systems. Furthermore, the thesis also investigates the fundamental influence of microstructure, such as surface morphology and crystal orientation, on the signal of the microscope.

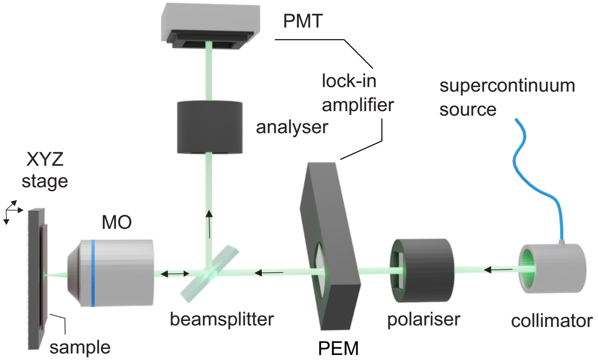

Figure 1.1: Proposed design of a RAS microscope based on a supercontinuum laser. PEM - photoelastic modulator, MO - microscope objective, PMT - photomultiplier tube.

1.3 Reader's guide

The thesis is organized in eight chapters, including this introduction, with chapters 5 and 6 largely based on the publication *"Scanning Reflectance Anisotropy Microscopy Multi-Material Strain Mapping"* [33]. A brief overview of the chapter structure is as follows:

- **Chapters 2 & 3:** These chapters provide an overview of the theoretical framework and experimental techniques applied in this work. For readers not familiarized with RAS, a read of chapter 2 is recommended.
- **Chapter 4:** This chapter provides a review of RAS microscopy, the improvements that SRAM brings to the field and a thorough characterization of the SRAM setup.
- **Chapter 5:** A demonstration of strain mapping for three different materials, gold, crystalline germanium, and amorphous germanium, is provided.
- **Chapter 6:** An exploration into the use of nanoantennas as a model system for strain induced symmetry breaking and a demonstration of the phase sensitivity of the setup.
- **Chapter 7:** This chapter is an escapade into the influence of crystal orientation in copper on the SRAM signal
- **Chapter 8:** Lastly the main findings of this thesis are discussed and a quick outlook into future research is given.

Theory 2

2.1 Principles of RAS 5
2.2 Strain sensitivity of RAS 7
2.3 Strain sensitivity of Raman spectroscopy 10
2.4 Plasmonic nanoantennas 11
2.4.1 Babinet's reciprocity principle 13

This chapter introduces the fundamental concepts needed to understand the working principles behind the experiments carried out in further chapters. A very brief overview of the technique this thesis is based upon, reflectance anisotropy spectroscopy, is presented, as well as a its relation to mechanical strain through the elasto-optic effect. Finally, given their intrinsically anisotropic response, plasmonic nanorod antennas provide an excellent system to test the microscope presented in this thesis as a phase sensitive characterization technique. To that end, a short description of the interaction of light with plasmonic nanoantennas is given.

2.1 Principles of RAS

Reflectance anisotropy spectroscopy (RAS) was conceived in 1985 by Aspnes *et al.* [18, 34] as an optical probe for monitoring surfaces during semiconductor growth. As has been stated in Chapter 1, RAS measures the normalized difference between the Fresnel coefficients along two orthogonal directions at near-normal incidence (see equation 1.1). Therefore, RAS probes and gives insight of the anisotropy and symmetry breaking in the electronic band structure at optical frequencies.

Since then there have been mainly two different setups proposed; a rotating analyzer scheme [18] and a phase modulation scheme [35]. The phase modulation scheme presents many advantages over the rotating analyzer scheme, such as speed, sensitivity and ease of alignment, and is currently the most popular implementation. Figure 2.1 shows a typical RAS setup based on a photoelastic modulator (PEM). A PEM is a birefringent crystal (such as silica or calcium fluoride) that is mechanically stressed close to its resonance frequency by using a piezoelectric transducer. This results in a time modulated waveplate, which introduces modulated retardation and results in phase modulated polarized light (as long as the incident light's axis of polarization differs from the optical axis of the PEM).

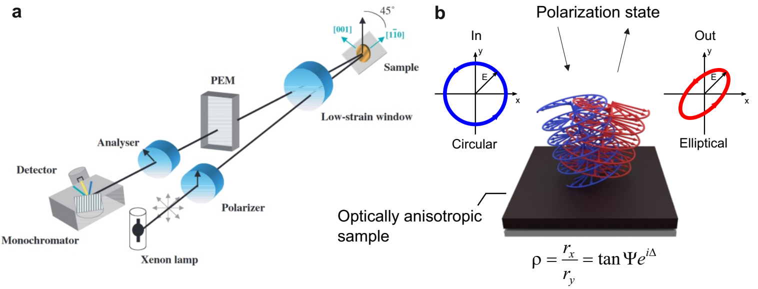

Figure 2.1: a Schematic of a typical phase modulated RAS setup in the polarizer-sample-photoelastic modulator (PEM)-analyzer configuration. The setup includes a low-strain window as RAS is often employed in vacuum environments. **b** Illustration of the measurement principle of RAS for a modulation state where the incident light is circularly polarized. In case of an optically anisotropic sample (in plane), the change in phase and amplitude of the out-going light can be represented by the sample's ellipsometric properties (Ψ, Δ) on the polarization state of the probing beam. **a** Reprinted from [19] with permission from the Institute of Physics.

The setup consists of a broad band source (generally a Xenon or Tungsten lamp), a polarizer (usually a high extinction rate polarizing prism), the photoelastic modulator, an analyzer and a detector scheme; monochromator, photomultiplier tube (PMT) and lock-in amplifier. Linearly polarized light is reflected by the sample at near-normal incidence and undergoes a small shift due to anisotropy at the sample plane. This shift is then phase modulated by the PEM and subsequently transformed into an intensity modulation by the analyzer. The intensity at the detector can be expressed as

$$I \propto 1 + 2\Re\left(\Delta r/r\right) \sum_{m=0}^{\infty} J_{2m}(\Gamma_0)\cos(2m\omega t) + 2\Im\left(\Delta r/r\right) \sum_{m=0}^{\infty} J_{2m+1}(\Gamma_0)\sin\left[(2m+1)\omega t\right], \tag{2.1}$$

where J_n is the nth-order Bessel function, ω the operating frequency of the photoelastic modulator and Γ_0 the modulation amplitude chosen such that $J_0(\Gamma_0) = 0$, and $\Delta r/r$ is given by $\Delta r/r = 2\left(r_x - r_y\right)/\left(r_x + r_y\right)$. By using a lock-in amplifier one can extract $\Re\left(\Delta r/r\right)$ and $\Im\left(\Delta r/r\right)$ from the first and second harmonic components. A full derivation of equation 2.1 using a transfer matrix analysis of the polarization elements in the setup [36] can be found in Chapter 8.4a. As can be seen from equation 2.1, the design of the RAS setup allows to directly probe Δr, making the setup much more sensitive than techniques in which differential reflectance is calculated with separate experiments using linearly polarized light. The use of lock-in amplifiers has led to RAS reaching sensitivities of $\Delta r/r \sim 10^{-5}$.

While $\Re\,(\Delta r/r)$ is typically the value reported in classical RAS measurements, it does not provide an intuitive understanding of the sample's optical properties. Instead, from $\Delta r/r$ one can calculate the ellipsometric parameters,

$$\rho = \frac{r_x}{r_y} = \frac{2 - \Delta r/r}{2 + \Delta r/r} = \tan \Psi e^{i\Delta}, \tag{2.2}$$

with $2\,(\Psi - \pi/4) \simeq \Re\,(\Delta r/r)$ and $\Delta \simeq \Im\,(\Delta r/r)$ for small $\Delta r/r$ [37]. Here, (Ψ, Δ) are the ellipsometric parameters (derived from r_p/r_s) at near-normal incidence and provide a straightforward description of the effect the in-plane optical anisotropy of a material has on the reflected light (see Figure 2.1b). Since RAS is effectively a near-normal incidence technique, circumventing the angular dependence of the Fresnel coefficients, Ψ and Δ directly quantify the anisotropic optical properties of the sample, making RAS a phase-sensitive technique.

RAS is a versatile technique that has been employed for a wide variety of purposes. These include monitoring thin film growth [38–41], determining optical axis orientation [42, 43], studying magneto-optical properties [44–46] or strain sensing [17, 22, 25] among others. For an in depth review of reflectance anisotropy spectroscopy see reference [19].

2.2 Strain sensitivity of RAS

Usually, the electric displacement field in the presence of both an electric field and stress is defined as

$$D = d\sigma + \varepsilon E \quad , \tag{2.3}$$

where d is the piezo-electric tensor and ε is the dielectric permittivity tensor. However, in reality the permittivity also depends on both stress and electric field due to higher order contributions, such that

$$D = d\sigma + \varepsilon E + aE^2 + b\sigma^2 + c\sigma E + \ldots \quad , \tag{2.4}$$

where a, b and c are the coefficients describing the second order effects. The dielectric permittivity, defined as $\varepsilon = (\partial D/\partial E)_\sigma$, is then

$$\varepsilon = \varepsilon' + aE + c\sigma + ... \quad . \tag{2.5}$$

ε' represents the unperturbed permittivity and the second order contributions (first order with respect to the permittivity) are the electro-optic effect, $a = \left(\partial^2 D/\partial E^2\right)_\sigma$, and the elasto-optic effect, $c = \partial^2 D/\partial\sigma\partial E$. Of particular interest in this thesis is the elasto-optic effect, which governs the dependence of the dielectric permittivity (or refractive index) on stress. While the elasto-optic effect is of very small magnitude, as it is a second order effect, the high sensitivity of RAS allows to characterize the change in permittivity due to stress and act as a strain sensing technique. Generally, elasto-optic tensor is defined via the change in relative dielectric impermeability $(1/\varepsilon)$ as

$$\Delta\varepsilon_i^{-1} = \frac{1}{\varepsilon} - \frac{1}{\varepsilon'} = p_{ij}\epsilon_j = \pi_{ij}c_{jk}\sigma_k \tag{2.6}$$

with ϵ_j being the components of the strain tensor, c_{jk} the elastic stiffness tensor and π_{ij} the piezo-optic tensor. Symmetry arguments have been used to reduce index notation to $i, j = 1, 2, ..., 6$, see reference [47] for more information on these. For small strains, equation 2.6 can be approximated to

$$\Delta\varepsilon_i = -\varepsilon'^2 p_{ij}\epsilon_j \quad . \tag{2.7}$$

For a cubic material ($m3m$), such as silicon and germanium, the elasto-optic tensor has three independent components, p_{11}, p_{12} and p_{44}. In the case were the direction of observation is one of the principal crystal axis, e.g. [001], the difference in dielectric permittivity and reflectance can be written as

$$\Delta\varepsilon = \Delta\varepsilon_{[100]} - \Delta\varepsilon_{[010]} = -\varepsilon'^2\left(p_{11} - p_{12}\right)\left(\epsilon_1 - \epsilon_2\right) \quad , \tag{2.8}$$

where $\epsilon_1 = \epsilon_{xx}$ and $\epsilon_2 = \epsilon_{yy}$. This expression allows to link the strain state of a crystal to the RAS signal. For small anisotropy in the dielectric function (ε_1, $\varepsilon_2 = \varepsilon_1 + \Delta\varepsilon$, $\Delta\varepsilon \ll \varepsilon_1$), the optical response can be written as [19]

$$\frac{\Delta r}{r} = \frac{\Delta\varepsilon}{\sqrt{\varepsilon'}\left(1 - \varepsilon'\right)} \quad , \tag{2.9}$$

such that, when combining equations 2.8 and 2.9, one obtains the expression

$$\frac{\Delta r}{r} = -\frac{\varepsilon'^{3/2}}{1-\varepsilon'}\left(p_{11}-p_{12}\right)\left(\epsilon_1-\epsilon_2\right) \quad . \tag{2.10}$$

It is straightforward conclude from equation 2.10 that the relation between RAS signal and the difference in strain along the two measurement axis is linear. The sensitivity of the technique is, therefore, a function of the unperturbed dielectric function and of the elasto-optic tensor's components. Since both these tensors are dependent on the light frequency ω, the strain induced RAS signal is also dependent on ω and presents resonances at the same critical points as ε and p.

For polycrystalline materials with the elasto-optic tensor can be rotated via a tensor transformation

$$p'_{ijkl} = a_{im}a_{jn}a_{ko}a_{lp}p_{mnop} \quad . \tag{2.11}$$

Note that the reduced notation p_{ij} cannot be used when transforming a fourth rank tensor. As each grain has a particular crystal orientation and size, the unperturbed permittivity for grain k is $\varepsilon'^{(k)}$, the transformation tensor is $a^{(k)}$ and the area weight is $w^{(k)}$ such that

$$\Delta\varepsilon_{ij} = -\sum_k \varepsilon'^{(k)2} w^{(k)} a^{(k)}_{im} a^{(k)}_{jn} a^{(k)}_{ro} a^{(k)}_{sp} p_{mnop}\epsilon_{rs} \quad . \tag{2.12}$$

Equation 2.12 can be used to calculate the RAS signal for samples with a limited number of grains inside the probing spot, provided the components of p_{mnop} are known. When the grain size is significantly smaller than the probing spot such calculation becomes too complex. Instead, assuming the grain distribution is isotropic, equation 2.12 can be simplified to an average value such that, when combining with equation 2.9 one obtains the expression

$$\frac{\Delta r}{r} = -\frac{\varepsilon'^{3/2}}{1-\varepsilon'}\overline{P}\left(\epsilon_1-\epsilon_2\right) \quad . \tag{2.13}$$

where $\overline{P}$ is now the elasto-optic constant. $\overline{P}$ depends not only on material but also on texture and can vary depending on sample fabrication.

2.3 Strain sensitivity of Raman spectroscopy

Raman spectroscopy is a non-destructive analytical technique that provides information on the phononic response of a sample by exploiting the Raman effect [48]. This effect occurs due to coupling between electronic and phononic energy levels, causing an interaction between the incident photon and the vibrational modes of the sample, resulting in scattering at shifted frequencies. The energy shift and amplitude of the Raman resonance is a fingerprint of the sample's chemical composition and structure, allowing for its identification and analysis. Raman spectroscopy is used for a wide variety of applications [49, 50] and, in particular, for strain sensing [51]. This section provides a very brief description of the strain sensitivity of Raman spectroscopy for semiconductors with a (100) out of plane crystal orientation following references [52, 53].

The Raman scattering efficiency is determined by the Raman tensors $\boldsymbol{R_j}$, which represent the phonon polarization directions, and the incident (e_i) and scattered (e_s) light polarization polarization

$$I \propto \sum_{j=1}^{3} \left| e_i \cdot \boldsymbol{R_j} \cdot e_s \right|^2 \quad . \tag{2.14}$$

For an arbitrary crystal orientation one would have to rotate the Raman tensors but, for an O_h crystal with (100) out of plane orientation, the following Raman tensors apply

$$\boldsymbol{R_1} = \begin{pmatrix} 0 & 0 & 0 \\ 0 & 0 & d \\ 0 & d & 0 \end{pmatrix} \quad , \quad \boldsymbol{R_2} = \begin{pmatrix} 0 & 0 & d \\ 0 & 0 & 0 \\ d & 0 & 0 \end{pmatrix} \quad , \quad \boldsymbol{R_3} = \begin{pmatrix} 0 & d & 0 \\ d & 0 & 0 \\ 0 & 0 & 0 \end{pmatrix} \quad , \tag{2.15}$$

with the indices 1,2 and 3 corresponding to the x,y and z directions. This means that the longitudinal optical phonon (determined by $\boldsymbol{R_3}$) is the only mode that can be probed for a (100) crystal orientation at normal incidence. For a more accurate description one would have to take the numerical aperture of the objective lens into account as it cause a small component of out-of-plane polarization. However, assuming purely in-plane polarization is a good approximation for qualitative measurements.

To calculate the Raman shift due to strain the secular equation is solved, which includes the phonon deformation potential tensor $\boldsymbol{K}$

$$\left(\boldsymbol{K} - \omega^2 \boldsymbol{I}\right) \cdot q = 0 \quad , \tag{2.16}$$

where q are the eigenvectors and ω the eigenfrequencies. For small strains the secular equation can be simplified to

$$\begin{vmatrix} p\varepsilon_{11} + q(\varepsilon_{22} + \varepsilon_{33}) - \lambda & 2r\varepsilon_{12} & 2r\varepsilon_{13} \\ 2r\varepsilon_{12} & p\varepsilon_{22} + q(\varepsilon_{11} + \varepsilon_{33}) - \lambda & 2r\varepsilon_{23} \\ 2r\varepsilon_{13} & 2r\varepsilon_{23} & p\varepsilon_{33} + q(\varepsilon_{11} + \varepsilon_{22}) - \lambda \end{vmatrix} = 0 \tag{2.17}$$

with p, q and r being the independent components of the deformation potential tensor for an O_h crystal. The eigenfrequencies are defined with $\lambda_i = \omega_i^2 - \omega_0^2 \simeq \Delta\omega_i 2\omega_0$, where $\Delta\omega_i = \omega_i - \omega_0$ is the Raman shift. Considering a strain state without off-diagonal components the solution to the secular equation is then

$$\Delta\omega_3 = \frac{1}{2\omega_0}\left[p\varepsilon_{33} + q(\varepsilon_{11} + \varepsilon_{22})\right] \quad . \tag{2.18}$$

The Raman shift is then a function of the strain in the three principal axes in case of no off-diagonal components. It is clear that a single phonon mode's Raman shift is not enough to decouple the strain components a obtain a thorough mechanical characterization of the sample. This becomes even more complicated when the numerical aperture of the objective is taken into account, although then other modes might be proved. In general, FEM simulations are needed to calculate the expected Raman shift.

2.4 Plasmonic nanoantennas

Localized surface plasmons (LSP) are collective oscillations of electrons that occur at the surface of metallic nanoparticles or nanostructures [54]. When light interacts with these nanoparticles it can excite LSPs, which results in a strong enhancement of the electromagnetic field in the vicinity of the nanoparticle. This phenomenon has a range of important applications in fields such as sensing [55] and catalysis [56]. LSPs are highly sensitive to the size, shape, and composition of the nanoparticles, as well as to the surrounding environment, making them a versatile tool for a wide range of applications [57].

These oscillations can excite different modes depending on the shape and size of the nanoparticle, *e.g.* dipolar or a quadrupolar modes. A mode is characterized by the electric charge distribution on the nanoparticle or nanostructure, which has a strong influence on its optical properties, such as the frequency and amplitude of the resonance or the directionality of the scattered light [58]. While the near-field distribution around the antenna can be calculated using classical antenna theory, *i.e.* obtaining the vector potential $\boldsymbol{A}$ through integration of the Green's function $G(\boldsymbol{r},\boldsymbol{r'})$ [59], in practice FEM are usually employed to simulate the optical response of metallic nanoantennas.

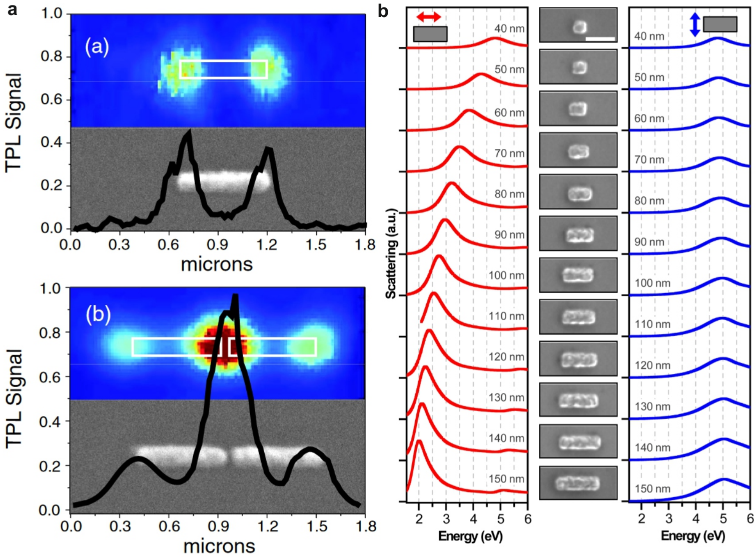

Figure 2.2: Modes of nanorod antennas and length dependence of the resonance frequency. **a** Electric field intensity of a single nanoantenna (top) and a dimer antenna (bottom) mapped using two-photon induced luminescence. The single nanoantenna shows a dipolar distribution, with a pole at each end of the antenna, while the dimer shows a maximum enhancement at the gap between antennas. **b** Evolution of the resonance peak as a function of rod length, showing a red shift for larger wavelengths.**a** Reprinted from [60] with permission from the American Physical Society. **b** Reprinted with permission from [61]. Copyright 2012 American Chemical Society.

Figure 2.2a shows the field distribution of a nanorod antenna and an antenna dimer measured with two-photon induced luminescence [60]. As one can see, the fundamental mode for the single antenna presents a dipolar charge distribution, with the antenna divided in two opposite charged poles, which can be modeled as a Lorentz oscillator. As expected, the resonance frequency is determined by the dimensions and refractive index of the antenna and red shifts for longer antennas (see Figure 2.2b) [61].

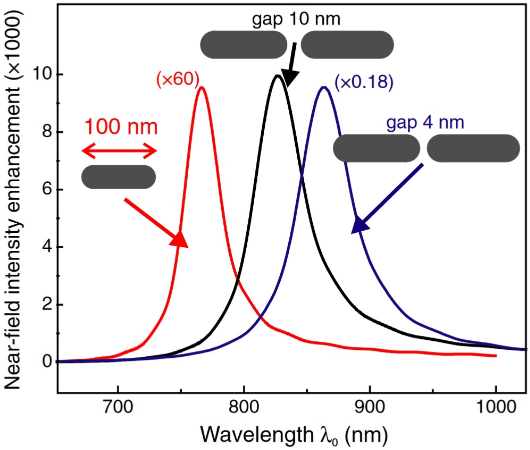

Figure 2.3: Gap influence on the resonance frequency of nanorod dimer antennas. The dimer system is red shifted with respect to the single nanoantenna, with a wider gap blue shifting the resonance towards the single antenna case. Reprinted from [62] with permission from the IOP Publishing.

Bringing two nanorod antennas together red shifts the resonance [62], due to the total longitudinal dimension increasing, and the fundamental mode is no longer dipolar (see Figure 2.2a). The gap size influences the strength of the resonance, as the field confinement is dependent on the optical path between the individual antennas, as well as the frequency, with the expected red shift for larger gaps (Figure 2.3). Nonetheless, the gap between nanoantennas needs to be significantly smaller than the length of each antenna to have a strong influence.

2.4.1 Babinet's reciprocity principle

Babinet principle states that the diffraction from a solid object presents the same intensity distribution as diffraction from its hollow analogue (usually an aperture) [63]. Interestingly, this can be applied to plasmonic nanoantennas as well. In such case, antennas built into the substrate, as is the case of the nanoslot antennas presented later in chapter 6, show the same modes as standard nanoantennas but with the electric and magnetic field's role reversed (Figure 2.4). This does not affect the resonance, which is characterized by the same frequency and lineshape.

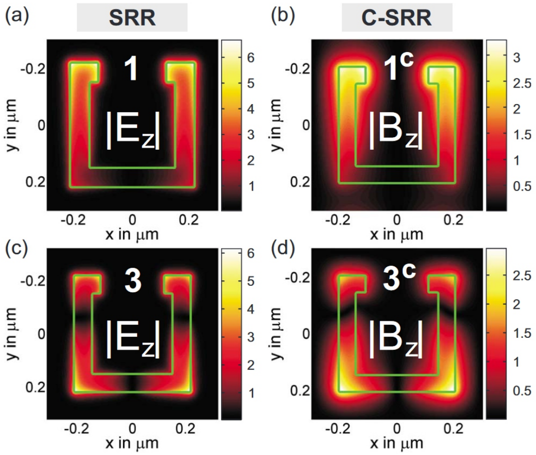

Figure 2.4: Babinet's principle for optical nanoantennas. Electric and magnetic field distribution for the first and third order eigenmodes for a solid split ring resonators (SRR) and its hollow Babinet complementary resonators (C-SRR). The calculated distributions show how the roles of the electric and magnetic field are reversed for Babinet antennas. Reprinted from [63] with permission from the American Physical Society.

Materials and methods 3

This chapter outlines the experimental procedures and techniques employed throughout this thesis so that results can be reproduced.

3.1 Sample procedures 15
3.2 Analysis 16

3.1 Sample procedures

Thin film deposition

Gold (99.99% MaTeck GmbH) films are deposited with a magnetron sputtering machine (PVD Products Inc.) with a chamber pressure of $5 \cdot 10^{-7}$ Torr, argon plasma pressure of 3 mTorr and 200 W magnetron power onto two different substrates. 500 nm films are deposited onto a 50 μm thick polyimide film (Kapton E, DuPont de Nemours Inc.) for the double wedge experiments. The Kapton E films are cleaned by ultrasonicating for 10 min in aceton, ethanol, and isopropanol, rinsing with isopropanol and drying overnight in vacuum. For the nanoantennas experiments, 100 nm gold films are deposited on a silicon nitride wafer and then template stripped (see the following subsection).

Germanium (99.999% Kurt J. Lesker) films are deposited with an evaporator (Kurt J. Lesker) at a deposition temperature of 1350-1400°C, a substrate temperature of 230°C (preheated for 2 hours) and a chamber pressure between 10^{-7} and 10^{-6} Torr.

Template stripping

The template stripping is carried out after film deposition on silicon nitride wafers following reference [64]. The films are stripped in a hot-press transfer process with polycarbonate pellets (Makrolon, Bayer AG) at 240 °C and 20 kN with the films getting cooled under pressure to prevent wrapping [65].

Copper crystals

Copper ingots (OF 99.99%, Bikar Metale GmbH) are melted on a graphite crucible in a tube furnace (Nabertherm GmbH) at 1150°C for 90 min in argon atmosphere and subsequently cooled to 950°C during 240 min with the sample off-centered in the tube to achieve directional solidification. The samples are then cut (IsoMet 4000, Buehler AG), grinded and polished. The polishing steps are are follows

- Polishing with 250 nm diamond particles (Struers GmbH, Denmark) in a lubricant solution (Blue, Struers).
- Polishing with a non-crystallizing colloidal 20 nm silica particle suspension (MasterMet 2, Buehler AG).
- Etching for 25 s with an equal part solution of water, 25% ammonia and 3% hydrogen peroxide.
- Polishing with 20 nm silica particles.

The copper plates samples (OF 99.99%, Bikar Metale GmbH) are prepared by annealing at 700°C for 40 hours at 10^{-9} Torr chamber pressure and followed by the first two steps in the polishing procedure described above. The final polishing step is done with a broad ion beam at 75° and 6 kV for 60 min.

3.2 Analysis

Raman spectroscopy

The Raman scans on the Germanium micro-bridges were carried out following reference [66] using a commmercial Raman microscopy setup (LabRAM HR Evolution UV-VIS-NIR, Horiba Ltd.) with a 1800 gr/nm and 500 nm blaze grating and a 532 nm single wavelength laser (1500 mW Nd:Yag, Cobolt Samba). The same objective as in the SRAM setup (LMPLFLN50X, Olympus) was used with a single accumulation of 1 s integration time per point. The obtained spectra were fitted with a Lorentzian function to calculate the Raman shift from the unstrained c-Ge peak at 300.7 cm^{-1}. Raman spectra of the amorphous germanium films are taken with WITec CRM200 setup with a 2400 gr/nm grating (500 nm blaze) and laser wavelength 532 nm.

Reflectance anisotropy spectroscopy

RAS measurements are carried out following reference [64] with a PEM based setup assembled by the Institute of Experimental Physics (Johannes Kepler University Linz, Austria). Spectra are taken with a spacing of 0.02 eV in the range 1.5 eV to 5.5 eV (Xenon lamp), time constant $\tau_c = 0.05$ s and integration time 1 s. The films are cut in stripes of 3 mm by 30 mm, with a gauge length of 25 mm, and strained with a micro-tensile stage from Kammrath and Weiss. SRAM measurements are carried out with the setup described in depth in Chapter 4 using a manual tensile stage actuated with a micrometer screw with a graduation of 10 μm per division (150-801ME, Thorlabs Inc.). As the film has a gauge length of 25 mm, that translates to a strain resolution of ±0.02%

Other analysis techniques

AFM measurements (Cypher S, Asylum Research) are taken with ultra-high frequency aluminium coated silicon tips (Arrow UHF, NanoAndMore GmbH) with a tip height of 3 μm and resonance frequency in the 0.7 to 2.0 MHz range. For the samples with anisotropic roughness, the height to height correlation function is calculated

$$H_r(r) = \langle |h(x-r) - h(x-r)|^2 \rangle \quad , \tag{3.1}$$

where r is the displacement vector from point x. The correlation length τ is found by fitting the heigh to height correlation function with the following Gaussian equation

$$G_x(r) = \sigma^2 e^{r^2/\tau_x^2} \tag{3.2}$$

where σ is the root mean square deviation.

XRD measurements of germanium thin films are taken with a commercial setup on H-2H Bragg-Brentano configuration (X'Pert MRD, Panalytical), with a Cu Ka1 source (k=1.540598 Å), 0.008° step size and 80 s integration time per step.

EBSD analysis is performed at 25 kV and 15 mm working distance with a high performing camera (Hikari, EDAX) in a standard electron microscope (Quanta 200F, Thermo Fisher Scientific).

Principles of SRAM 4

4.1 Review of spatially resolved RAS techniques 19
4.1.1 Existing μRAS setups 20
4.2 Scanning Reflectance Anisotropy Microscopy 24
4.2.1 Design 25
4.2.2 Sensitivity 27
4.2.3 Resolution 30
4.3 Influence of sample topography . 32
4.3.1 Film edges 32
4.3.2 Roughness 37

This chapter introduces RAS microscopy; the advances in the field since it was first proposed as well as the setup proposed in this thesis. The advantages and disadvantages of existing setups are discussed and used as a basis for a detailed explanation on the design of the scanning reflectance anisotropy spectroscopy setup presented herein. A characterization of the setup sensitivity and resolution is provided as well as a thorough discussion on the artefacts introduced by RAS microscopy with measurements carried out with the setup.

4.1 Review of spatially resolved RAS techniques

The concept of RAS microscopy (μRAS) was first introduced by Koopmans *et al.* [67]. They inserted RAS optics into a standard confocal microscope (Figure 4.3c), namely polarizers and PEM, in order to map the anisotropy in semiconductor quantum wells. While such a simple idea might seem straightforward, it introduces complications in the acquisition of RAS spectra, mainly because of the increased angle of incidence. Under normal incidence ($\theta = 0$) both Fresnel coefficients, $r_p(\theta)$ and $r_s(\theta)$ for parallel (TM) and perpendicular (TE) polarizations, are identical. However, r_s and r_p start diverging for $\theta \neq 0$ (Figure 4.1), thus performing RAS with a large angle of incidence introduces an ellipsometric component to the signal that is not inherent to the sample's anisotropy. Using an objective lens for focusing purposes significantly increases the angle of incidence, hence contributing undesired ellipsometric artefacts to the signal.

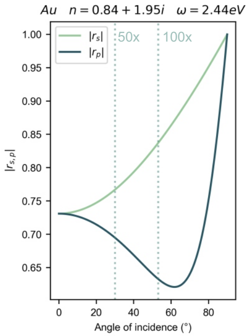

Figure 4.1: Modulus of the Fresnel reflectance coefficients for gold at 2.44 eV as a function of angle. The incidence angles of the two objectives used in this work are indicated with vertical lines.

However, Koopmans *et al.* [26] and Shen *et al.* [27] demonstrated that these artefacts can be compensated by the symmetry of the system. Since RAS presents a 2-fold

(4-fold in the absolute value of amplitude) symmetry by design and an objective lens maintains cylindrical symmetry upon illumination of the sample, the intensity at the focal place exhibits a $x^2 - y^2$ symmetry, as can be seen in Figure 4.2. Upon integration over the beam profile the ellipsometric artefacts are compensated and the signal yield is net-zero for isotropic samples

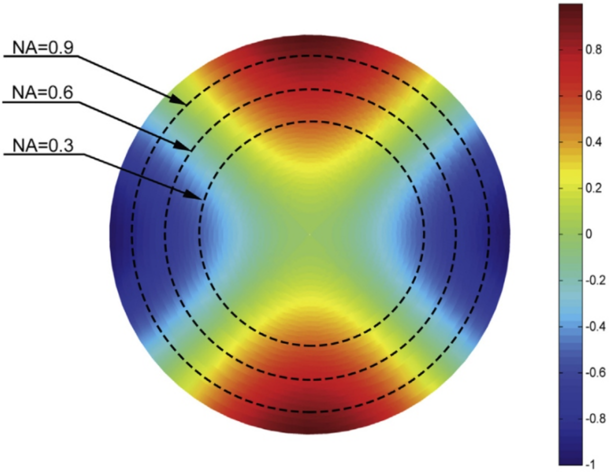

Figure 4.2: Calculation of the RAS signal at the focal plane after an objective lens as a function of numerical aperture. The analysis was performed following the vectorial ray tracing theory by Richards and Wolf [68]. The $x^2 - y^2$ symmetry of the beam that cancels out the RAS signal is easily appreciated. Reprinted from [27] with permission from Elsevier.

Depolarization aberrations also introduce artefacts for higher numerical apertures. However, these are also compensated for in phase-modulated setup schemes upon integration over the beam profile [26]. This means, as expected, that both ellipsometric and depolarization artefacts are minimized when using low numerical aperture objective lenses and a trade-off between sensitivity and resolution exists. Furthermore, the use of beamsplitters induces additional artefacts, due to the 45°angle of incidence, that can be corrected with a calibration curve of the setup.

4.1.1 Existing μRAS setups

Since RAS microscopy was first performed by Koopmans *et al.*, there have been mainly four different setup schemes proposed. Figure 4.3 shows an example that represents each kind of setup that has been suggested up till now. The setups can be categorized into two distinct groups; camera-based (**a,b**) and laser-based setups (**c,d**).

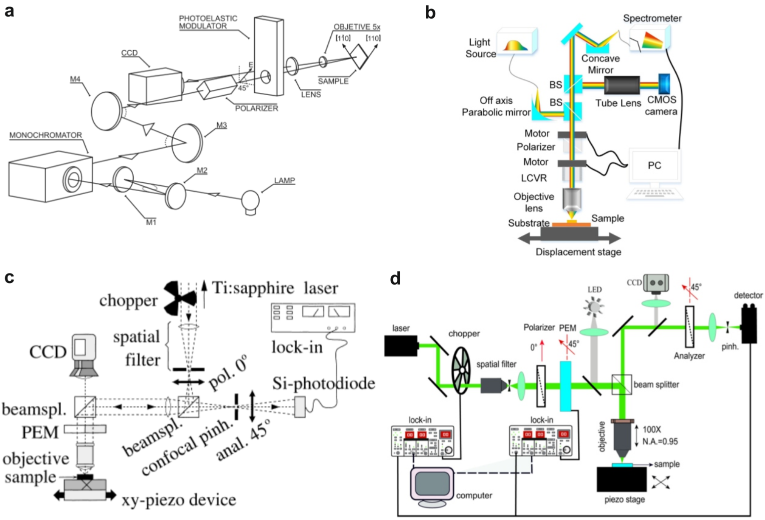
a
PHOTOELASTIC MODULATOR
OBJETIVE 5x
[110]
[110]
CCD
E
45°
SAMPLE
LENS
POLARIZER
M4
M3
MONOCHROMATOR
M2
LAMP
M1
b
Spectrometer
Light Source
Concave Mirror
BS
BS
Tube Lens
CMOS camera
Off axis Parabolic mirror
Motor
Polarizer
Motor
LCVR
PC
Objective lens
Substrate
Sample
Displacement stage
c
chopper
Ti:sapphire laser
spatial filter
lock-in
CCD
pol. 0°
Si-photodiode
beamspl.
PEM
beamspl.
confocal pinh.
anal. 45°
objective
sample
xy-piezo device
d
LED
CCD
45°
detector
laser
chopper
Polarizer PEM
0°
45°
spatial filter
Analyzer
pinh.
beam splitter
lock-in
lock-in
objective
100X
N.A.=0.95
sample
computer
piezo stage

Figure 4.3: Example of the four different μRAS setups that have been previously proposed. These can be divided in camera-based setups (**a,b**) and laser based setups (**c,d**). **a** First camera based setup proposed by Lastras-Martinez *et al.*, reprinted from [31] with permission from Optica. **b** LCVR setup adapted for microscopy with the use of a camera, reprinted from [27] with permission from Elsevier. **c** First microscopy setup based on a double beam splitter proposed by Koopmans *et al.*, reprinted from [26] with permission from AIP. **d** Single beam splitter configuration proposed by Huang *et al.*, reprinted from [29] with permission from Optica.

Camera based setups

Camera-based setups have the advantage of not inserting polarization altering optics (beamsplitter) between the polarizer and analyzer, thus reducing sources of artefacts that could decrease sensitivity. The use of a camera also allows to directly capture images, avoiding the need to scan the sample and greatly increasing the speed of data acquisition. Figure 4.3a shows the first camera based setup proposed by Lastras-Martinez *et al.* [31]. They inserted a low magnification 4-f system into the beam path and substituted the PMT by a camera. This has the advantage that both ellipsometric and beamsplitter-induced artefacts are minimal.

However, the lack of a lock-in amplifier means that amplitude modulations cannot be detected. The authors instead consider the beam to be unpolarized (due to the frame rate of the camera compared to the resonance frequency of the PEM) when the PEM is on while inhibiting the PEM results in a fully linearly polarized beam. Subtracting an image in each configuration yields the absolute value of the RAS signal $\Delta R/R$ with a reported resolution of 2.5 μm. This means the noise introduced by the camera is significant compared to the signal and severely limits the sensitivity of the setup — to the point where the authors used pixel binning resulting in reduced spatial resolution of 10 to 20 μm.

Lastras-Martinez *et al.* have used this setup to study semiconductor materials with anisotropy stemming from growth on a step graded layer [69], strain induced by directional mechanical polishing [31, 70, 71], and quantum wells [72]. They also reportedly employed a nanoRAS setup based on scanning near-field optical microscopy [73] but offered no description of the setup. A later publication [74] described a similar setup but with a non-RAS contrast mechanism. Therefore, currently a nanoRAS setup is not yet considered to have been successfully implemented.

Shen *et al.* [27] adapted the camera setup introduced by Lastras-Martinez to their liquid crystal variable retarder (LCVR) design (Figure 4.3b), which substitutes the PEM and lock-in amplifier for a variable retarder and a least squares regression scheme. The setup allows the use of both a camera and a spectrometer in a beamsplitter configuration. Scanning the sample while collecting spectra with the spectrometer results in a hyperspectral image of the sample. In contrast, taking an image with the camera avoids scanning the sample but, since the light reaching the camera is not monochromatic, yields an integration over the whole spectral range. This setup design offers the possibility for fast measurements with the use of a camera or slower measurements with a higher information yield when using the spectrometer. Furthermore, commonly to camera setups, the placement of the beamsplitter before the polarization optics reduces the sources of artefacts.

However, even if a high magnification objective is used, the setup still relies on a lamp as a light source. Therefore, when using the spectrometer as a detector the resolution of the setup is limited by the extended nature of the light source, achieving a reported resolution of 25 μm (50x objective) or 10 μm (100x objective) [27]. While the setup introduces significant artefacts, see Figure 4.4, a calibration procedure that uses a modified collection algorithm is able to reduce these.

Instead, employing the CCD camera greatly improves resolution, theoretically up to the diffraction limit. However, an imaging system relies on collecting light reflected from the sample at different angles, breaking the symmetry of the system at individual pixels and introducing spatial artefacts [75].

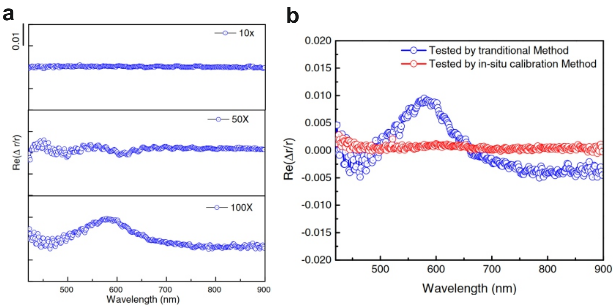

Figure 4.4: a Spectra taken using different objectives in the LCVR setup. As can be observed, the artefacts introduced by the 50x and 100x objectives ($\simeq 10^{-2}$) are of significant magnitude compared to typical RAS signals. **b** Comparison of spectra taken with the 100x objective before and after the custom calibration algorithm. Reprinted from [27] with permission from Elsevier.

Furthermore, since the phase delay of the LCVR cannot be tuned for each camera pixel, the artefact correction algorithm cannot be employed. Therefore, only a 5x objective lens with limited numerical aperture is used resulting in a 3 μm spatial resolution. The setup has been employed for lithography structures characterization [75] and for characterization of 2D materials [27, 28, 76–81].

Laser-based setups

The first ever proposed μRAS setup was based on a Ti:sapphire laser and is depicted in Figure 4.3c [26, 67]. The setup consisted on a double beamsplitter microscope configuration with RAS optics (polarizers and PEM) inserted in the beam path and a silicon photodiode connected to a lock-in amplifier as a detector.

There are a couple of points that are important to remark about such a setup. The first one is the tunability of Ti:sapphire lasers, typically within (but not completely covering) the wavelength range between 650 nm (1.91 eV) and 1100 nm (1.12 eV). Such a tunability theoretically enables spectral acquisition at diffraction limited resolution. However, while the authors mention the tunability of the laser, they do not make use of its spectral bandwidth.

The second one is the use of two beamsplitters instead of a single beamsplitter microscope configuration. Koopmans *et al.* do not mention the reason behind such a choice but the assumption is that the intention is to compensate phase artefacts introduced by the beamsplitter. It is unclear how this is achieved, especially considering they placed the first polarizer and beamsplitter inside the spatial filter of the laser. Furthermore, the PEM is placed right before the objective to minimize polarization contributions of the other optical elements of the setup. This results in the laser beam going twice through the PEM, thus the first polarizer and the PEM have to be perfectly aligned to avoid double modulation.

Koopmans *et al.* used both a specific alignment procedure to minimize double modulation by the PEM as well as a compensation procedure using an isotropic mirror to reduce artefacts introduced by the other optical elements in the setup. In such way they managed to measure RAS signals in the order of 10^{-4} when characterizing semiconducting quantum wells [26]. A later implementation of this setup by Lastras-Martinez *et al.* [32] was used to map polishing induced defects on GaAs, seemingly achieving 10^{-3} sensitivity and resolution on the order of 1 μm (these are estimated values as they were not reported by the authors).

Koopmans's setup can be modified to a single beamsplitter configuration with the RAS optics inserted in the beam path of a standard microscope [30], as is shown in Figure 4.3d [29]. This results in a simpler implementation, alignment and artefact correction and has been proven to maintain the RAS sensitivity of the original setup [30]. Unfortunately, no setup apart from Koopmans' has been implemented with a tunable laser. These setups have been mainly used to characterize topographic features, including defects on InN and InGaN films [29, 82], and nanometric height steps on lithography patterned Si [30].

Overall, imaging systems provide a wide spectral range when using a monochromator while maintaining fast acquisition times and being demonstratively simpler to implement, e.g. the lack of a second polarizer and beamsplitter and use of low numerical aperture objectives increases the tolerance to alignment errors. As a trade-off, laser setups are more sensitive, offer higher signal to noise ratio and, most importantly, enable higher resolution at the cost of slower acquisition.

4.2 Scanning Reflectance Anisotropy Microscopy

As has already been commented in Chapter 1, in order for RAS to be employed in micro-mechanical studies it is essential to improve spatial resolution, if possible sub-micron resolution. Such spatial resolution has so far only been achieved in laser setups, with camera setups limited to a few μm at best. The LCVR camera setup could also potentially achieve high resolutions for studies that do not need cutting edge sensitivity since its beamsplitter-objective configuration is not fundamentally limited to low numerical apertures.

Nonetheless, both laser setups and the LCVR camera setup cannot perform spectroscopy. Current laser setups are restricted by the single wavelength nature of the source, which limits the range of materials and applications that RAS microscopy can access, while the LCVR camera setup is limited by the lack of a monochromator when used in imaging mode. The LCVR setup does provide images that are an integration of the spectral bandwidth of the source, hence enabling measurement of a wider range of materials. However, the RAS signal stemming from strain-induced symmetry breaking is usually on the order of 10^{-3} [20], which would be outside the sensitivity limit of a high numerical aperture LCVR setup. Furthermore, the real part of the signal $\Re\{\Delta r/r\}$ stemming from non-equibiaxial strain yields a zero value upon integration.

To harvest the full potential of RAS microscopy, and given the capabilities of the presented setups, it is a good assumption that the ideal solution would be the use of a tunable laser, similarly to the original setup built by Koopmans *et al.*. That would allow to extend the spectral range of laser setups while maintaining the high spatial resolution and signal to noise ratio. For that purpose, we propose a supercontinuum laser as a wide range tunable source [83]. Supercontinuum lasers can access a broad spectral bandwidth, including the visible and near infrared regions of the spectrum, with a high spatial coherence, making them an ideal candidate for microscopy. To distinguish the new setup introduced here from other existing setups in the literature with different capabilities, we name the new technique Scanning Reflectance Anisotropy Microscopy (SRAM).

4.2.1 Design

The setup design is based on references [29, 30] as the single beamsplitter scheme is simpler compared to Koopmans' design [67] while keeping RAS sensitivity. Figure 4.5 shows a schematic drawing of the main elements of the setup (aligning mirrors and apertures have been excluded).

The light source is a supercontinuum laser (SuperK EXR-20, NKT Photonics) with continuum generation ranging from 485 nm to 2400 nm and a total power of 2000 mW in the visible region (350 nm - 850 nm). An acusto-optic tunable filter (SuperK SELECT, NKT Photonics) is used as a monochromator between 485 nm to 700 nm wavelengths, resulting in a linewidth ranging between 2 nm and 5 nm depending on wavelength. There is also the option

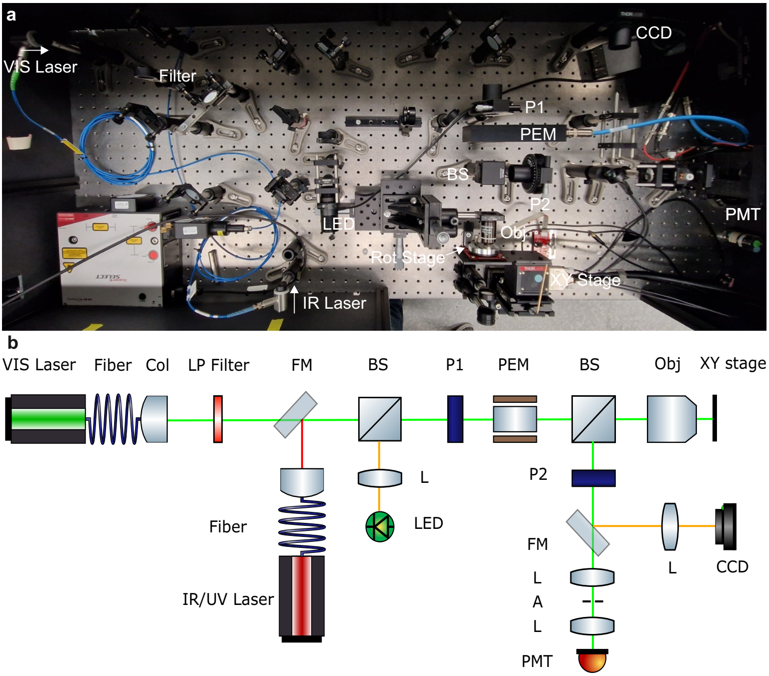
a
VIS Laser
Filter
CCD
P1
PEM
BS
P2
LED
Obj
Rot Stage
XY Stage
PMT
IR Laser
b
VIS Laser
Fiber
Col
LP Filter
FM
BS
P1
PEM
BS
Obj
XY stage
L
LED
P2
Fiber
FM
L
CCD
L
A
L
IR/UV Laser
PMT

Figure 4.5: Picture (**a**) and schematic (**b**) of the SRAM setup based on a typical beamsplitter microscope configuration with RAS optics inserted in the beam path. Abreviations: Col - collimator, FM - flip mirror, LP filter - low pass filter, BS - beamsplitter, P - polarizer, PEM - photoelastic modulator, L - lens, A - aperture, PMT - photomultiplier tube.

of using an acusto-optic filter for the IR region as well as a UV extension (based on second harmonic generation). Spectra taken with these extensions are not discussed on this thesis but are included in Figure 4.5 for completion since they appear in the setup picture. As the repetition rate of the laser is in the MHz range and much larger than the resonance frequency of the PEM (≃50 kHz), the laser is considered to act as a continuous-wave laser.

The output of the laser is coupled into an optical fiber, which spatially filters unwanted modes and secondary lobes. A low pass filter (710 nm edge wavelength, Thorlabs Inc.) is added to filter out the remaining higher wavelength modes that are not filtered out by the fiber. An off-axis parabolic metallic mirror (RC04APC-F01, Thorlabs Inc.) is employed in order to maintain perfect collimation over the wide spectral range of the setup.

The polarization optics of the setup comprise a photoelastic modulator (FS50 PEM100, Hinds Instruments Inc.) and two Rochon prisms (α-BBO, Edmund

Optics Ltd.) with an extinction ratio smaller than 10^{-5} that act as polarizer and analyzer. The microscope is set in a Polarizer (45°) - PEM - Sample (45°) - Analyzer (0°) configuration, with the orientation angle of the polarization axis of each element with respect to the PEM's axis given in brackets, and the alignment procedure outlined in reference [37] was followed. It is important to note, given the orientation of the PEM with respect to the lab reference frame, the setup measures the difference in reflectance between the axes at ±45°with respect to the scanning stage frame.

The beamsplitter (BSW10R, Thorlabs Inc.), objective lens and lens-aperture system (LA4148 - SM1D12D - LA4148) before the detector add the microscope functionality to the setup. Three different non-polarizing beamsplitters were tried, including a cube beamsplitter and a polka-dot plate beamsplitter, and the visible plate beamsplitter was found to yield less artefacts. To reduce the effect of ghosting introduced by the beamsplitter, a filtering system with two lenses and an aperture is introduced before the photomultiplier. An imaging system with an LED and CCD camera is used for objective alignment and navigation on the sample.

The objective lens used in this thesis is an infinity corrected 50x objective (LMPLFLN50X, Olympus) with a numerical aperture of 0.5 and a working distance of 10.6 mm. Its long working distance and small back aperture, ensuring a filling factor of 1, help minimize misalignment artefacts. The LMPLFLN50X is also a semiapochromat objective, which is a good correction for chromatic aberration, with a flat transmission line in the range of the microscope. To study the effect of higher numerical apertures, a 100x objective lens of the same family (LMPLFLN100X, Olympus) with a numerical aperture of 0.8 and working distance of 3.3 mm is used.

Finally, the PMT (R10699, Hamamatsu) output current and the reference signal of the PEM are read by a lock-in amplifier (MFLI500, Zurich Instruments Ltd.) to measure the real and imaginary part of the SRAM signal. Unless otherwise indicated, spectra in this thesis are taken with a phase-locked loop time constant of 0.05 s, integration time of 1 s and in constant dc current mode with a target current of 12 μA. The wavelength step size is 2 nm and a Savitzky-Golay filter [84] with window length 11 and 3rd order polynomial is applied to smooth the data.

4.2.2 Sensitivity

To assess the sensitivity of the setup, a hyper-spectral image of a silicon (100) wafer, which is isotropic and should yield no SRAM signal, is performed.

Figure 4.6 shows the recorded mean signal and standard deviation as a function of photon energy (eV) of both real and imaginary parts with no objective in the beam path (**a**), with the 50x objective (**b**, 0.5 NA) and with the 100x objective (**c**, 0.8 NA). Table 4.1 shows the maximum and minimum values for the mean and standard deviation of the spectra.

Table 4.1: Mean and standard deviation values of 100 spectra taken on a silicon (100) wafer, for both real and imaginary parts of the SRAM signal, with no objective, the 50x objective and the 100x objective.

		Real		Imaginary	
		Mean	std	Mean	std
0x	Max	$1.1\cdot10^{-2}$	$3.0\cdot10^{-4}$	$1.3\cdot10^{-3}$	$5.0\cdot10^{-5}$
	Min	$9.4\cdot10^{-3}$	$1.5\cdot10^{-4}$	$8.6\cdot10^{-4}$	$2.3\cdot10^{-5}$
50x	Max	$1.3\cdot10^{-2}$	$3.4\cdot10^{-4}$	$5.6\cdot10^{-3}$	$1.4\cdot10^{-4}$
	Min	$1.0\cdot10^{-2}$	$2.0\cdot10^{-4}$	$3.2\cdot10^{-3}$	$8.2\cdot10^{-5}$
100x	Max	$1.0\cdot10^{-2}$	$6.0\cdot10^{-4}$	$-2.1\cdot10^{-4}$	$3.0\cdot10^{-4}$
	Min	$8.0\cdot10^{-3}$	$4.4\cdot10^{-4}$	$-9.3\cdot10^{-4}$	$1.6\cdot10^{-4}$

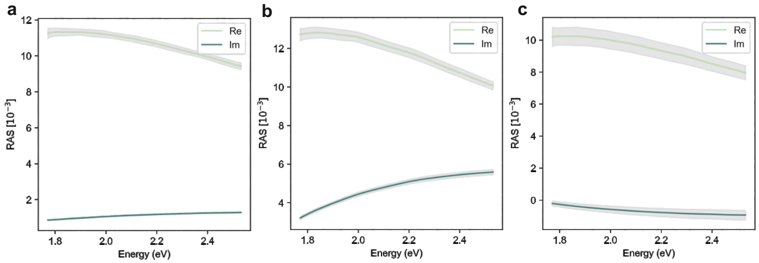

Figure 4.6: Average (green) and standard deviation (grey) of 100 spectra taken on a Si (100) wafer with no objective (**a**), with the 50x objective (**b**) and with the 100x objective (**c**).

A few observations can be made about the presented data. First and foremost, the lineshape of the mean spectrum is not flat, even when no objective lens is used. This is an artefact particular to RAS microscopy, as the standard deviation is an order of magnitude smaller than the mean deviation. It was observed as well that the exact lineshape would change with objective alignment while the mean value being higher for real than imaginary part stays consistent with both numerical aperture and objective alignment. One can then infer that the artefact signal is influenced by two components. The first component is constant with wavelength with a mean value $\sim 10^{-2}$ and $\sim 10^{-3}$, for real and imaginary part respectively, and is introduced by the beamsplitter, since it is present without the addition of the objective. Then there is a second component of smaller magnitude that is introduced by the objective lens and is dependent on alignment and numerical aperture. As expected, the error increases with numerical aperture for both real and imaginary part.

The second observation is that the real part of the SRAM signal presents a higher standard deviation than that of the imaginary part, between 2 to 3 times higher depending on wavelength. Since the mean value of the real part is significantly higher than in the imaginary part, the error stays proportionally similar between both parts of the signal. Interestingly, this seems to be the opposite to typical classical setups where the imaginary part is noisier [19]. In classical setups the imaginary part is affected by the birefringence of the vacuum quartz window as well as leakage in the polarizer and the real part is affected by misalignment of the polarizer with respect to the PEM. Misalignment of the sample and analyzer result in a different expression for real and imaginary part [85].

In the case of the SRAM setup there is no birefringent window to increase the noise in the imaginary part and it is possible that optical components have significantly improved since references [19, 85] where published, overall decreasing the noise in the imaginary part. In contrast, misalignment of the polarizer is still present in the SRAM setup and could be the cause of the increased noise in the real part of the signal compared to the imaginary part and add to the effect of the beamsplitter — although at a smaller scale.

Finally, the light source in SRAM also outputs lower power with decreasing wavelength as the limit of the continuum generation is approached, similarly to classical setups but in the visible range instead of in the UV. A lower dc current leads to a higher voltage supply to the PMT and to a noisier measurement. Since RAS relies on evaluating the quotient between two current measurements, an increase in noise could potentially also lead to the spectra's mean value increase. However, the laser provides higher signal to noise ratio than lamps and the decrease in intensity is only noticeable for samples with high roughness or absorption. This can be seen in the noise measurements presented in Figure 4.6 where the standard deviation increases with decreasing wavelength for the imaginary part but does the contrary for the real part.

Overall, the SRAM setup achieves a sensitivity in the order of 10^{-4}, at worst $6.0 \cdot 10^{-4}$. This is one order of magnitude lower than the limit sensitivity of classical setups but similar to koopman's setup [26], though over a wider spectral range, and improving over the other setups discussed in section Section 4.1.

Calibration

Calibration of the setup can be carried out by subtracting the data acquired with the sample oriented at 0°and at 90°[29]. However, this is impractical for scans, where image correlation would be needed and data acquisition is relatively slow. Instead, a calibration curve on a silicon wafer (or a region of the sample that presents no intrinsic anisotropy) is taken each time that objective alignment is changed. Subtracting the calibration curve from the acquired data allows to record the proper spectral lineshape. This can be seen in Figure 4.7, where the SRAM spectra taken on a sputtered 500 nm gold film on polyimide as a function of strain before (**b**) and after calibration (**a**) are shown. More details on the fabrication and characterization of the films are given in Chapter 5.

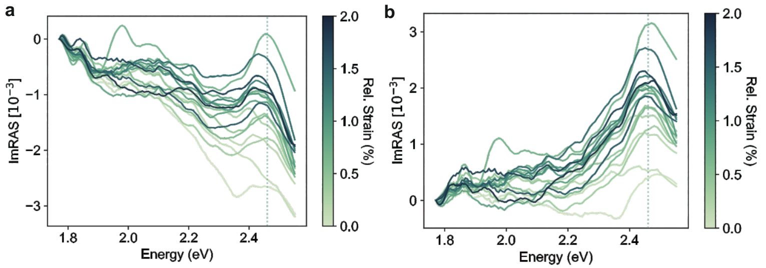

Figure 4.7: Effect of calibration on the spectral line shape of SRAM. Spectra of a sputtered 500 nm gold film on polymide for sequential externally applied uniaxial tension before calibration (**a**) and after calibration (**b**)

4.2.3 Resolution

The point spread function (PSF) is the image of a point source by an optical microscope or, in other terms, the system's impulse response. The PSF is an important tool for measuring the resolution of an optical microscope, which is defined as the ability of a microscope to distinguish two closely spaced objects as separate entities. While there are several criteria for calculating the resolution limit of a microscope, a practical approximation very close to Abbe's criterion [86] is the use of the microscope PSF's full width half maximum.

Therefore, in order to measure the PSF of the SRAM setup, an anisotropic point source is needed. A sub-diffraction slot antenna (width: 50 nm, length: 100 nm) milled on a template stripped gold film presents a dipolar transition that can be measured by the setup and can be employed to measure the PSD of the microscope. More details on the fabrication of the antennas and their characterization can be found in Chapter 6.

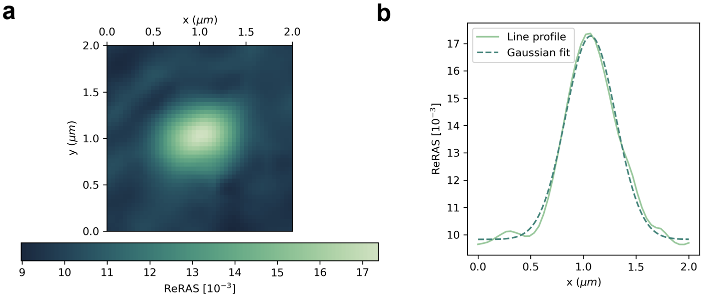

Figure 4.8: a Single wavelength scan of a single nanoantenna at 2.39 eV, linearly interpolated after a 45°rotation. The resulting signal is a convolution of the point spread function of the nanoantenna and the point spread function of the focused light. Since the nanoantenna could be interpreted as a point like structure, the signal is close to the point spread focused beam. **b** Line profile of the scan in **a** fitted with a gaussian function. The full width half maximum of the fitted gaussian is 560 nm.

Figure 4.8 shows the SRAM map of a single slot antenna at its resonance frequency (**a**) and the resulting intensity profile (**b**). As expected, a Gaussian function provides a very good fit to the intensity profile, from which a full width half maximum of 560 nm is calculated. Comparing to Abbe's criterion, given by

$$d = \frac{\lambda}{2NA} \tag{4.1}$$

and yielding a resolution limit of 520 nm, the measured point spread function is slightly higher. However, it is important to note that, while the antenna has a sub-diffraction length, it can not be fully considered a point source. Therefore, the resulting SRAM map is a convolution of the PSF of the microscope with that of the antenna's and is strictly an upper limit to the setup's resolution. Considering the size of the antenna (50 nm by 100 nm) and the difference between the measured PSF and Abbe's criterion (40 nm) as well as the good fit by the gaussian function, it is safe to state that the microscope is diffraction-limited.

4.3 Influence of sample topography

As is mentioned in Section 4.1 and can be seen in Figure 4.2, RAS microscopy relies on compensating non-zero angle of incidence induced artefacts upon integration over the beam profile. This has the known consequence of surface features that break the symmetry of the beam at the focal plane giving rise to an anisotropy signal [26, 30]. While such phenomena are also present in classical RAS [87], the effect is heightened for RAS microscopy because of the reduced focal spot.

4.3.1 Film edges

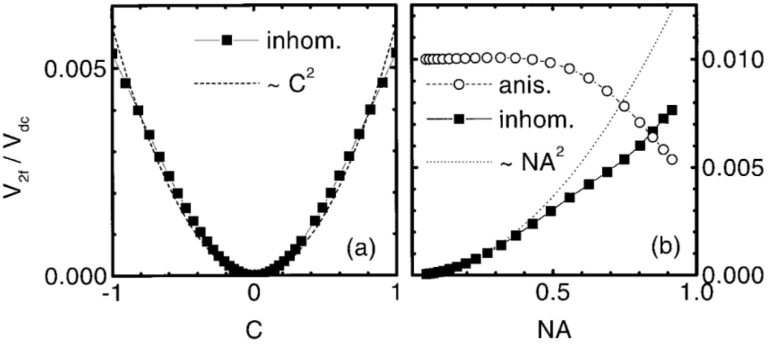

Figure 4.9: Effect of a step in dielectric function, defined as $C = (\varepsilon_L - \varepsilon_R)/(\varepsilon_L + \varepsilon_R)$ as a function of C at fixed NA=0.24 **a** and as a function of NA at fixed C=0.33 **b**. Reprinted from [26] with permission from Wiley.

Figure 4.9 shows the RAS signal induced by a step inhomogeneity in the dielectric function defined as $C = (\varepsilon_L - \varepsilon_R)/(\varepsilon_L + \varepsilon_R)$. As expected, the anisotropy signal increases both as a function of dielectric function mismatch and as a function of numerical aperture, with a quadratic dependence on C.

As already mentioned, inhomogeneities in the dielectric function can also stem from surface topography. A step edge will induce depolarization of the scattered light and result on a non-zero RAS signal. Figure 4.10 shows the RAS signal induced by a lithographically fabricated step edge on a thin film as a function of step height [30]. It can be seen that the spurious signal is proportional to the step height.

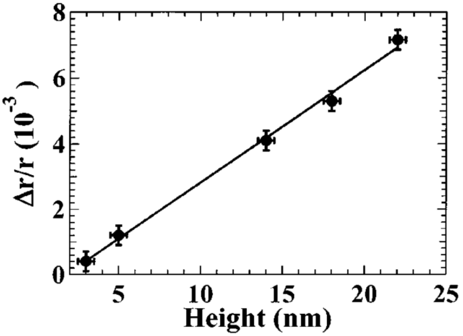

Figure 4.10: Influence of step height on the RAS signal of a step edge on a silicon wafer. Reprinted from [30] with permission from the American Institute of Physics (AIP).

However, the authors do not observe a meaningful decrease in signal when the edge step is oriented at 45° with respect to the measurement angles of the setup. Given the $x^2 - y^2$ symmetry of the system, one would expect a signal at 45° to vanish. The authors claim the scattering depolarization origin of the signal is not due to anisotropy and, thus, not affected by step orientation.

In order to probe the edge influence on the SRAM signal, an ellipse is FIBed on a 50 nm gold film sputtered on a silicon wafer. Figure 4.11 shows a scan of the ellipse at 532 nm and a step size of 250 nm with the 50x objective. As one can observe, the anisotropy signal vanishes when the tangent of the ellipse's edge is oriented at 45° with respect to the measurement axis of the setup, for both imaginary and real part. This is sustained by the theory and measurements established in references [26, 27, 29] but in contradiction to the measurements discussed before in reference [30].

Interestingly, in the case of the ellipse there is a presence of both anisotropy inducing phenomena discussed in this section, *i.e.* a step in dielectric function from gold to silicon and depolarization at a topographic step edge. Since there is no signal at 45° , that would indicate that both phenomena share a $x^2 - y^2$ symmetry. Regardless of the origin of the signal at a topographic step, which could be due to depolarization or plasmonic interactions, ultimately the effect can be modelled as a change in effective dielectric function and, as such, should follow the symmetry of the system. Otherwise, it would imply that a feature that is oriented at 45° with respect to the x and y axes results in different r_x and r_y.

One can also observe that the edge gives rise to different profiles for the real

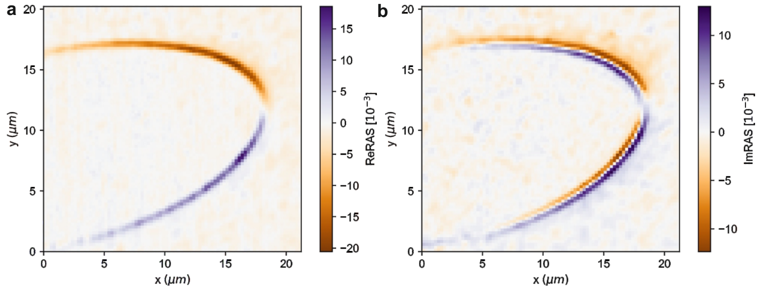

Figure 4.11: SRAM scan of an ellipse FIBed on a sputtered 50 nm Au film on a silicon wafer. The scan was performed at λ = 532 nm and with a pixel size of 200 nm. **a** Real part and **b** imaginary part.

and imaginary part of the signal. While the real part shows a similar profile to references [29, 30], the imaginary part shows a distinctive profile. This is the first time the imaginary part of the RAS signal for an edge has been reported so it cannot be compared to existing literature.

Taking a closer look at the calculated beam profile in Figure 4.2 can give some insight into the measured profiles for both real and imaginary parts. Figure 4.12 shows a very simplified schematic of the resulting signal profile after the beam scans over an edge for the two cases in discussion. When considering depolarization, the edge scatters a portion of the beam in a random polarization and the scattered light does not contribute to a net anisotropy signal. Therefore, as depicted in Figure 4.12b, the edge depolarization is considered to contribute by subtraction of the affected area. Figure 4.12c shows the sign of the resulting RAS signal when integrating over the beam profile for three different edge positions and Figure 4.12 shows the inferred edge profile from the three points.

In contrast, in the case of simple discontinuity in the dielectric function, the edge is not considered as a scattering object. Instead, the deviation between $r_s(\theta)$ and $r_p(\theta)$ as a function of angle depends on the dielectric function and, thus, differs at different points of the beam. This results in the integration over the beam profile not compensating the artefacts and results in a net anisotropy signal. A simplified way of representing such interaction is to divide the beam profile in two areas at each side of the edge, integrate over each area and add the resulting signals. Both sides will yield the same lineshape for the edge profile but the side with a higher deviation between r_s and r_p will have a higher influence on the resulting signal. Analogous to the depolarization case, Figure 4.12 e,f show the sign of the RAS signal for

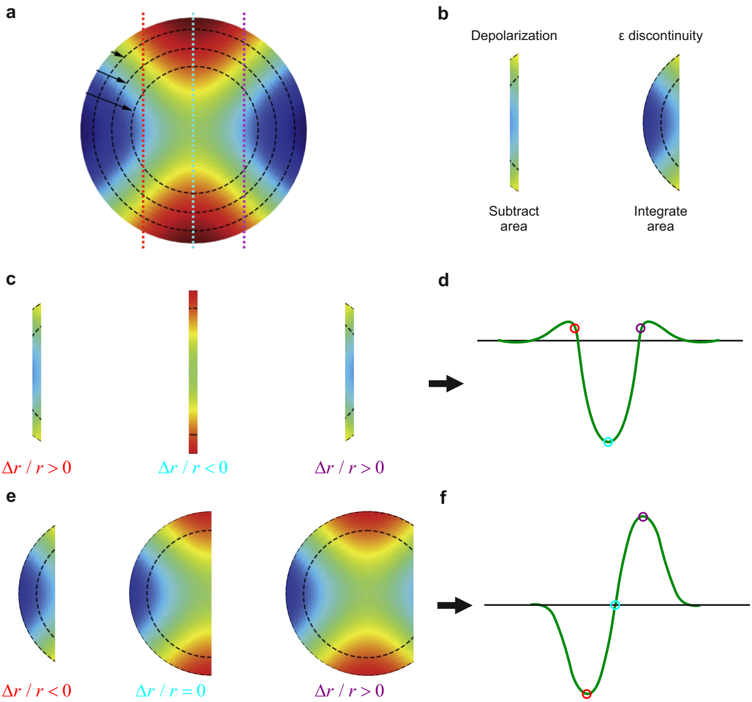

Figure 4.12: Simplified explanation on the origin of the RAS signal induced by an edge. **a** RAS signal profile as a function of numerical aperture, see Figure 4.2 for a more extensive explanation, reprinted from [27] with permission from Elsevier. **b** Schematic on how the edged induced RAS signal is calculated for two possible cases; depolarization and ε discontinuity. **c,d** Sign of the depolarization induced signal at three different positions indicated in **a** and the corresponding inferred signal profile. **e,f** ε discontinuity induced signal represented in an analogous way to **c,d**.

three different points and the inferred edge profile.

It is easily seen that the real part presents a similar lineshape to the inferred depolarization profile and similarly for the imaginary part to that of the dielectric function discontinuity. While the hypothesis presented here is a very simplified idea, from these results one could argue that the depolarization due to scattering at a step edge has a stronger effect on the real part of the RAS signal. Further calculations/simulations are needed in order to confirm such an explanation.

Taking advantage of the hyperspectral functionality of the SRAM setup can give some insight into the effect of the edge as a function of wavelength. Figure 4.13 shows the SRAM spectra for a line scan across the edge of the ellipse. As expected — as both scattering depolarization and ε discontinuity

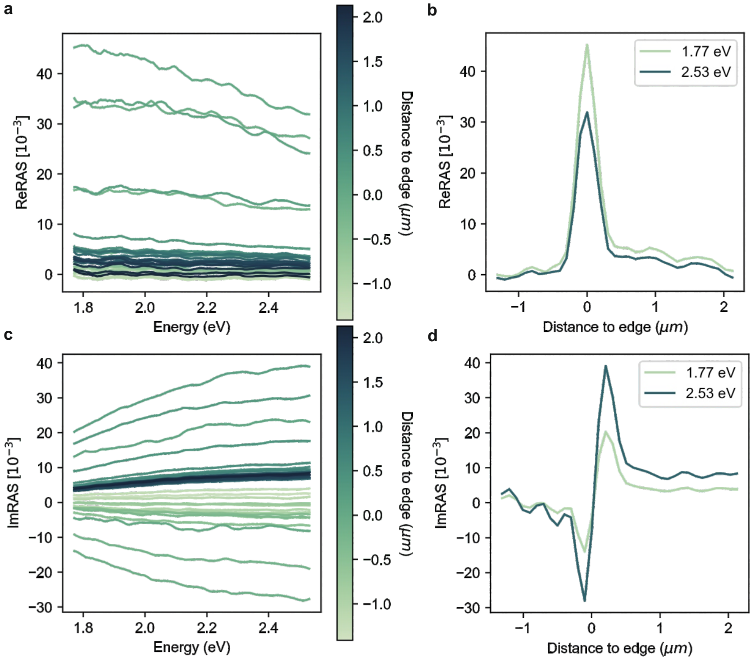

Figure 4.13: Spectral line scan over an edge of an ellipse FIBed on a 50 nm gold film on Si with a 50x objective. **a** Real part of the spectra and the corresponding edge profile for two different wavelengths **b**. **c** Imaginary part of the spectra and the corresponding edge profile for two different wavelengths **d**.

are dependent on wavelength — the edge induced signal presents a slight dependence on wavelength, with increasing signal for decreasing energy for the real part and the opposite for the imaginary part. As such, one could chose a scanning wavelength to minimize the edge effect depending on whether the real or the imaginary part is of interest.

Finally, to confirm the dependence on NA described in reference [26], the same measurement show in Figure 4.13 is repeated with the 50x objective lens. As expected, Figure 4.14 shows a stronger edge signal for the higher NA. Given the NA of the objectives, 0.5 for the 50x and 0.8 for the 100x, a quadratic dependence of C on NA would imply a signal ratio of $0.8^2/0.5^2 = 2.56$. According to Figure 4.9, the dependence on NA is only quadratic until NA$\simeq$0.5 and afterwards deviates to weaker NA influence, while the ratio shown in Figure 4.14 is 4.79 and would imply a stronger NA dependence. This measurement again hints at the presence of depolarization effects to explain the higher edge influence.

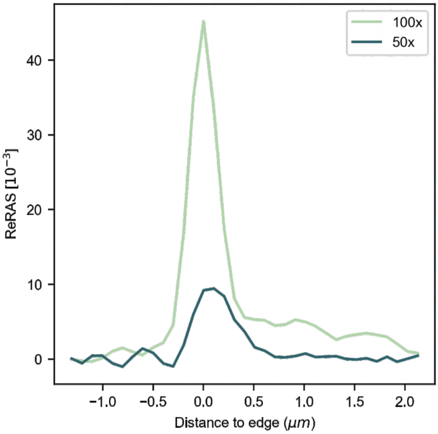

Figure 4.14: Edge profile of a FIBed ellipse on a 50 nm Au film on Si at 1.77 eV for two different objectives with numerical apertures 0.5 (50x) and 0.8 (100x).

4.3.2 Roughness

It has been shown that roughness can have a significant impact on classical RAS spectra, from sputtered surfaces [64] to roughened surfaces by polishing or ion bombardment [88–91]. Roughness can offset the RAS spectra as well as introduce modulations at low energies, unfortunately within the range of the SRAM setup.

Given the artefacts introduced by edges in the SRAM signal, it naturally follows that roughness artefacts are also heightened in RAS microscopy, especially considering the much larger coherence length of the light source when compared to classical RAS. In contrast, the wider collection angle of objective lenses allows to gather light from rougher surfaces compared to classical RAS, where the long distance between sample and detector severely limits the light collected from diffusive scattering.

Therefore, it is important to characterize the effect of roughness on the SRAM signal. Since the probing area is small, on the order of the wavelength, the correlation length τ in comparison to the wavelength has to be taken into account when analyzing roughness measurements. This section explores the influence of surface roughness with $\tau \gtrsim \lambda$ and presents noise measurements for varying roughness with $\tau \ll \lambda$.

Table 4.2: Standard deviation values obtained from a 100 spectra scan of a sputtered 50 nm gold film on silicon taken with a 50x objective (Figure 4.15).

	Real	Imag
Max	$3.2{\cdot}10^{-4}$	$5.0{\cdot}10^{-4}$
Min	$2.3{\cdot}10^{-4}$	$2.1{\cdot}10^{-4}$

Roughness with $\tau \ll \lambda$

A 50 nm gold film sputtered on Si is used as a test for surfaces with roughness smaller than the wavelength. Figure 4.15 a,b show the AFM scan of the film surface and the calculated height-height correlation function. The gaussian fit results in a roughness σ = 0.514 nm ±0.4 pm and correlation length τ = 11.9 ± 0.2 nm. For more details on the correlation function see Chapter 3.

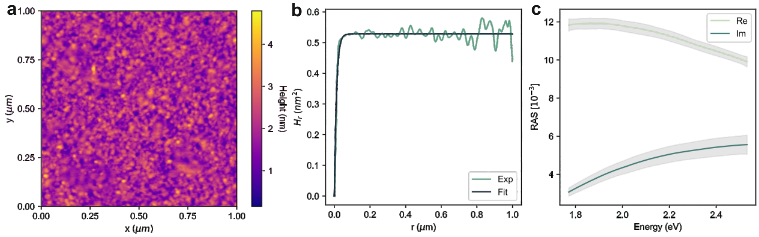

Figure 4.15: Influence of roughness on the SRAM signal for a 50 nm gold film sputtered on silicon. **a** AFM scan of the film and its calculated height-height correlation function **b** resulting in a roughness of 0.514 nm and correlation length of 11.9 nm. **c** Average of the SRAM signal recorded on the film showing the noise induced by the roughness.

Figure 4.15c shows the averaged spectrum of the gold film taken with the 50x objective. While the standard deviation of the real part (Table 4.2) stays at a similar level when compared to a silicon wafer (Table 4.1), the standard deviation of the imaginary part does increase, up to 3 times depending on wavelength. As expected, the increased roughness is translated into an increased noise level but the sensitivity is still within the 10^{-4}. Since the correlation length is much smaller than the wavelength, the increased noise is wavelength independent.

Roughness with $\tau \gtrsim \lambda$

Figure 4.16a shows the AFM scan at a grain junction in a copper plate. The plate has been annealed in vacuum at 700°C for 40 hours to grow the grains and later polished both mechanically and with broad ion beam. This results in a selective roughness depending on grain orientation. The grain at the top left corner of the AFM scan shows a structure that is anisotropic with a roughness much smaller than the wavelength but a correlation length on the order of the wavelength. Figure 4.16 c,d show the calculated height-height correlation function in for vertical and horizontal preferential directions yielding $\sigma_y = 27.4 \pm 0.1$ nm and $\tau_y = 476 \pm 15$ nm vertically and $\sigma_x = 29.3 \pm 0.9$ nm and $\tau_x = 2.21$ μm ± 30 nm horizontally. As can be seen, τ_y is slightly smaller than the resolution limit while τ_y is about four times larger.

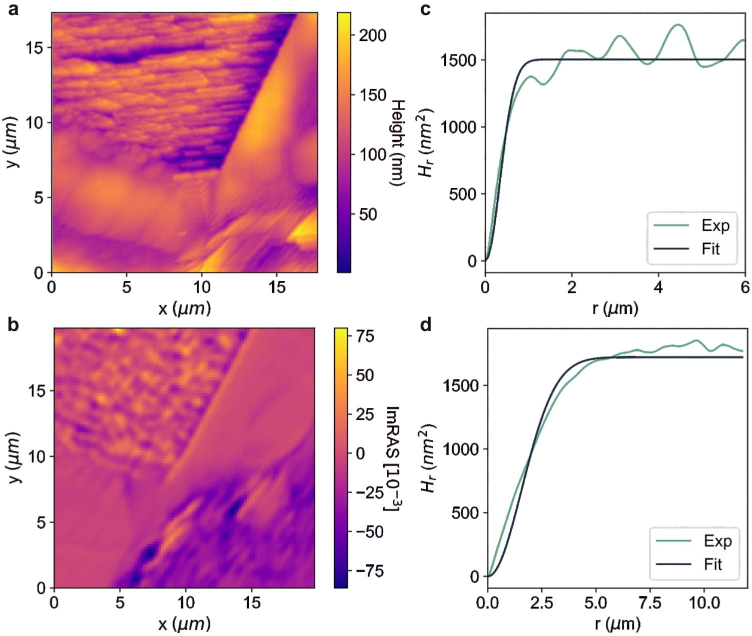

Figure 4.16: Influence of roughness on the SRAM signal for polished copper plate. **a** AFM scan of the plate at a grain junction and its calculated height-height correlation function in two preferential directions; vertical **c** and horizontal **d**. The fitted roughness and correlation lengths are $\sigma = 27.4$ nm and $\tau = 476$ nm in the vertical direction and $\sigma = 29.3$ nm and $\tau = 2.21$ μm in the horizontal direction. **b** SRAM map of the grain junction.

Figure 4.16b shows the imaginary part SRAM map of the grain junction. The roughness induced signal on the top left grain goes up to $7.5 \cdot 10^{-2}$, as expected because of the increased roughness. However, the anisotropic roughness structure cannot be resolved, even on the longitudinal direction where the correlation length is larger than the resolution of the setup. This is due to the inherent randomness of roughness, which makes it not possible to decouple the two directions with different correlation length.

Since $\tau \gtrsim \lambda$ the influence of roughness on the beam profile is not isotropic. This translates to a dependence of the induced signal on wavelength, unlike the edge case studied in section 4.3.1 or when $\tau \ll \lambda$. As can be seen in Figure 4.17b, the spectra's linehsape varies significantly in the space of 2 μm. Since this is a single grain, the signal difference cannot stem from crystallographic anisotropy and must be roughness induced.

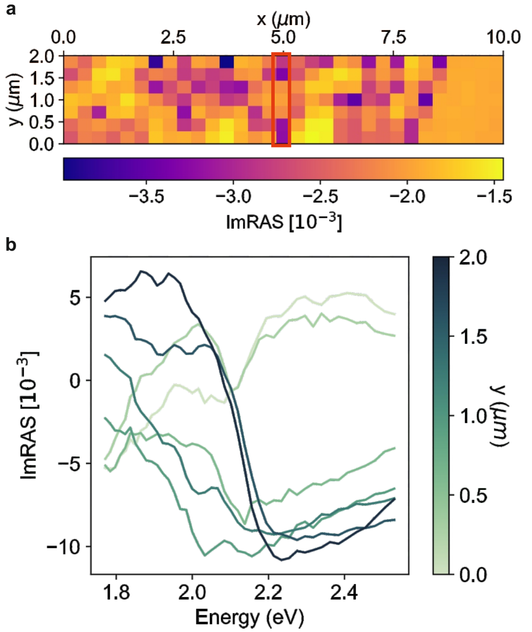

Figure 4.17: Hyperspectral scan of the rough copper surface at the grain boundary. **a** SRAM map at 2.1 eV showcasing the change in signal due to roughness. **b** Spectra at $x = 5$ μm, as indicated in red in **a**, showcasing the dependence on wavelength of the roughness induced signal.

Overall, there needs to be more experiments in surfaces with controlled roughness, *e.g.* through lithography, to accurately describe the effect on the SRAM signal. Nonetheless, one can conclude that roughness with $\tau \ll \lambda$ reduces sensitivity but its isotropic character and wavelength independence still allows for measurements to be carried out as long as the expected signal is above the new reduced sensitivity. Roughness with $\tau \gtrsim \lambda$ greatly distorts the signal and its impact on signal to noise ratio severely reduces the capabilities of the setup.

Strain sensing | 5

This chapter focuses on the use of the SRAM setup for multi-material strain sensing and mapping, including crystalline and amorphous semiconductors and metals. The sensitivity of SRAM to strain is discussed for each material and demonstrated with mapping of complex strain distributions. Raman spectroscopy is used as a comparison to a traditional strain mapping technique in highly strained suspended germanium micro bridges and the advantages and disadvantages of the SRAM setup are discussed.

5.1 Strain sensing with RAS 41
5.2 Crystalline semiconductors 44
5.2.1 Strain Sensitivity 44
5.2.2 Strain Mapping . 46
5.3 Metals 48
5.3.1 Strain Sensitivity 48
5.3.2 Strain mapping . 50
5.4 Amorphous semiconductors 52
5.4.1 Strain Sensitivity 52
5.4.2 Strain Mapping . 54

5.1 Strain sensing with RAS

As elaborated in Chapter 2, the elasto-optic effect makes RAS especially suited to detect breaking of the lattice symmetry due to strain. Much of the earlier work done on strained samples with RAS was focused on semiconductors to gain insight into the electronic band structure. The components of the piezo-optic and elasto-optic tensors above the fundamental bandgap were initially measured using piezo-reflectance measurements [92–94], a technique that makes use of the piezo-electric effect to induce birefringence via an applied electric potential and subsequently measures the changes in reflectance.

Parts of this chapter are based on the article titled *"Scanning Reflectance Anisotropy Microscopy for Multi-Material Strain Mapping"* by J. Sendra, F. Haake, M. Calvo, H. Galinski and R. Spolenak [33] currently under review in *Advanced Functional Materials*. Individual author contributions can be found in the declaration chapter.

However, II-VI semiconductors are too brittle to withstand the stresses needed for a significant reflectance change in piezo-reflectance measurements, making the more sensitive RAS technique an excellent candidate to characterize the piezo-optic properties of semiconductors [95]. RAS has been used to characterize the piezo-optic tensors of ZnSe and InP [95], Si [96] and ZnTe [97]. RAS has also been employed to characterize strain in semiconducting materials like Si [22, 70, 98], SiGe [99], GaAs [23, 70, 100, 101], ZnTe [102–104], CdTe [70, 103–105], ZnSe [104], GaP, InP and GaSb [70] among others. It is even possible to characterize strain induced in layered heterostructures like InGaAs/InP and InAlAs/InP [106] and GaAs/AlGaAs [107].

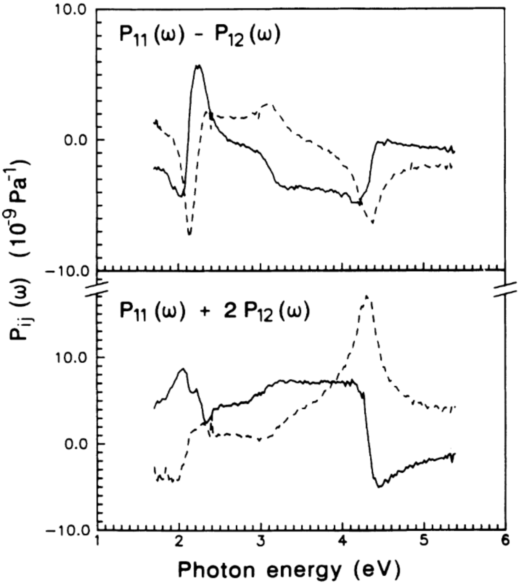

Figure 5.1: Real (solid line) and imaginary (dashed line) part of the piezo-optic tensor of germanium measured with rotating-analyzer ellipsometry. Reprinted from [108] with permission from the American Physical Society.

To the author's best knowledge strained germanium has not been measured with RAS yet but its piezo-optic tensor components have been measured using rotating-analyzer ellipsometry [108], a technique close to RAS. Figure 5.1 shows two irreducible components of the piezo-optic tensor of germanium in the visible and UV range. Germanium presents a feature around 2.2 eV, in the range of its E_1 and $E_1 + \Delta$ bandgap. Since this feature is within the range of the SRAM setup, germanium is used in this chapter to showcase strain mapping in semiconductors.

Cole *et al.* [21] were the first to employ RAS for strain sensing in metals. They strained a dog bone shaped copper foil while simultaneously acquiring RAS spectra and observed the rise of two distinct RAS features. The first one is a peak at 4.0 eV that shows a linear dependency on strain up until the yield point of copper where the signal saturates. On the other hand the signal at lower energies does not saturate and keeps increasing beyond the yield point, indicating that its not caused by the increase in inter-atomic distance.

While the exact origin of the feature is not yet clear, it has been demonstrated to be correlated to the onset of plastic deformation [64].

As in semiconductors, the strain sensitive feature in metals has its origin in dipolar interband transitions, as was demonstrated with *ab initio* calculations on copper (111) by Volpi *et al.*. This feature has been used for the mechanical characterization of thin films [20], where RAS was proved to be advantageous over x-ray diffraction due to its smaller probing volume and faster acquisition times [25]. RAS has also been employed for strain sensing in silver and gold [64], although the non-strain sensitive feature at low energies and the appearance of a global offset make full mechanical characterization difficult. However, decreasing surface roughness and introducing an offset correcting term allows to mitigate these effects [64].

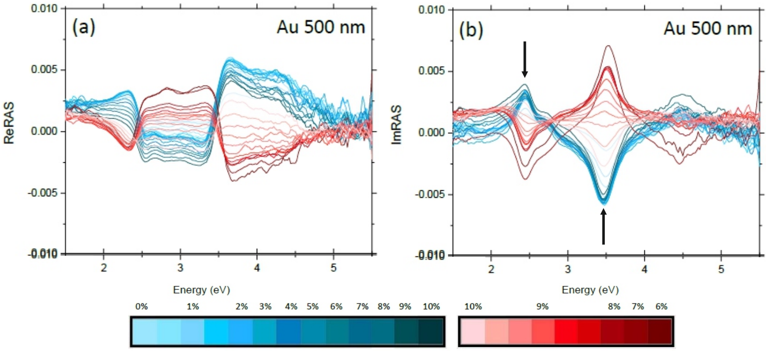

Figure 5.2: Real (**a**) and imaginary (**b**) part of the RAS signal acquired on a 500 nm gold thin film on polyimide for different uniaxial tensile loads. The loading steps are coded in blue while the unloading is coded in red and the two elastic features of gold at 2.4 eV and 3.5 eV are pointed with arrows. Adapted from [64], open access.

Figure 5.2 shows the RAS spectra of a gold thin film on polyimide for different steps of externally applied tensile load. As strain is increased, so does the amplitude of both the real and imaginary parts, as expected from equation 2.10. Since the polyimide film has a much higher yield point than gold, upon unloading the metallic thin film is driven into compression, as can be seen in the sign reversal of the spectra. Two strain sensitive features arise, one around 2.4 eV and the other one around 3.5 eV (signaled with arrows in Figure 5.2b), and the spectra also present a global offset (the imaginary part of the spectra should coincide far from resonance and the real part should coincide at the resonance frequency). While the elastic feature in copper and silver is found well into the UV, the gold peak at 2.4 eV falls inside the range of the SRAM setup, making it an ideal candidate to test the strain mapping

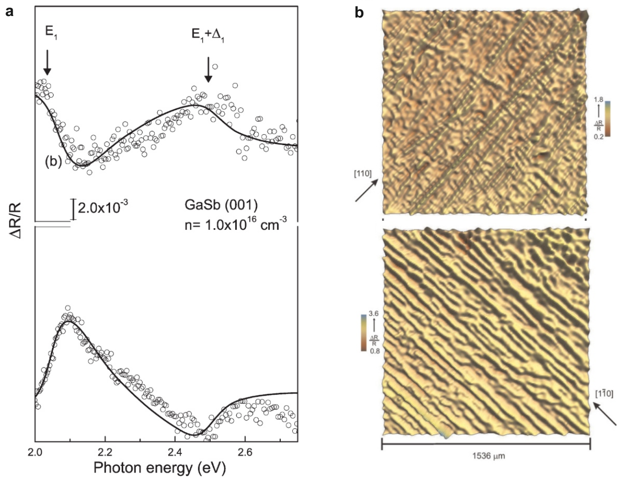

Figure 5.3: RAS spectra **a** taken of a GaSb surface rubbed with 1 μm diamond particles (top along [110] and bottom along [1$\bar{1}$0]) and the corresponding μRAS map showing the strain distribution with 24 μm resolution. Reprinted from [32], open access.

capabilities of the SRAM on metals.

Strain mapping with RAS microscopy has been largely unexplored, with the GaAs (100) and GaSb (100) surfaces being the only probed materials [31, 32]. Figure **??** shows the RAS distribution acquired with a CCD based microscope of a GaSb (100) surface that has been directionally rubbed with 1 μm diamond particles, anisotropically inducing dislocations. The spectra taken of the sample (averaged over the mapped area) shows the expected differential strain feature, indicating that the signal is strain induced. However, the authors don't comment on the effect of the diamond particles on roughness, which could also induce a RAS signal.

5.2 Crystalline semiconductors

5.2.1 Strain Sensitivity

When a semiconductor is mechanically deformed, the associated strain induces a change in the electronic band structure, which is most pronounced at critical points associated with interband transitions. This translates to a change in the dielectric permittivity and gives rise to a materials dependent optical signal. Especially epitaxial systems, due to their low roughness, defect density and large grain size, are well suited to study the deformation of the electronic band structure by optical means.

However, the low fracture strains sustained by brittle materials and the influence of random defects on their mechanical properties make tensile testing of semiconductor materials significantly more complicated than testing of metallic or polymeric materials [109]. Instead, compressive uniaxial or hydrostatic stresses have been used to measure the irreducible components of the piezo-optic and photoelastic tensors [108, 110]. In order to introduce tensile strains, three-point and four-point bending schemes are used, but they introduce complex strain states and can only apply limited elastic strain.

Here, we make use of suspended germanium micro bridges that achieve high uniaxial tensile loads (Figure Figure 5.4) to measure the resonance frequency of the irreducible component of the elasto-optic tensor ($p_{11} - p_{12}$). Uniaxial tension is achieved by depositing a thermally biaxially strained germanium layer on a silicon wafer and then using reactive ion etching to partially release the strain, resulting in highly strained microbridges. A detailed explanation of the fabrication method and a thorough characterization of the structure is available elsewhere [5].

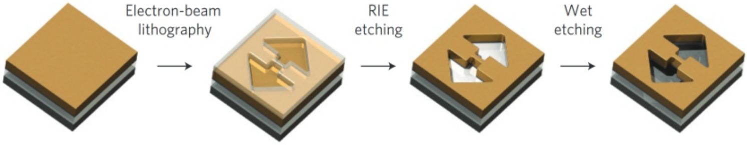

Figure 5.4: Schematic of the germanium suspended bridges lithographic fabrication. After etching of the biaxially strain germanium layer the resulting structures are under high uniaxial tension. Reprinted from [5] with permission from Springer.

Figure 5.5b shows the SRAM spectra taken at different spots of the bridge structure (the measured spots are indicated in Figure 5.5a)*. The signal is highest at the center of the bridge and completely disappears on the unreleased wafer, as expected for the equibiaxially strained layer. Fitting a Lorentzian lineshape to the peak at the center of the bridge yields a resonance frequency of 2.21 eV, which is in the range of the E_1 and $E_1 + \Delta$ bandgap and in good agreement with previous measurements of the piezo-optic tensor components of germanium [108] (see Figure 5.1).

---

* As explained in Chapter 2, $\Delta \simeq \Im\{\Delta r/r\}$.

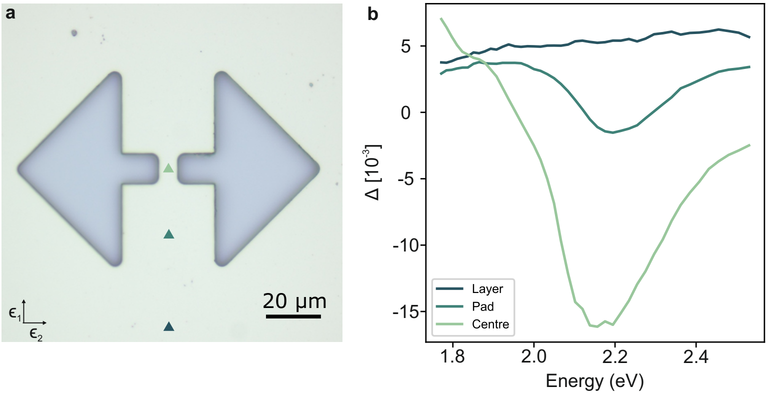

Figure 5.5: a Optical microscope top view of suspended and highly uniaxially strained germanium microbridges. The colored triangles indicate the position where the SRAM spectra in **b** were taken. **b** Measured spectra for different points of the structure. The highly uniaxial strain of the bridge yields a SRAM resonance while the equibiaxial strain of the unreleased germanium layer yields no signal.

5.2.2 Strain Mapping

Scanning the entire bridge at the resonance energy enables the determination of the local differential strain $\epsilon_{xx} - \epsilon_{yy}$. In excellent agreement with experiments and FEM simulations described in earlier works [5], the differential strain concentrates at the center of the bridge and falls off further away into the pad (Figure 5.6a).

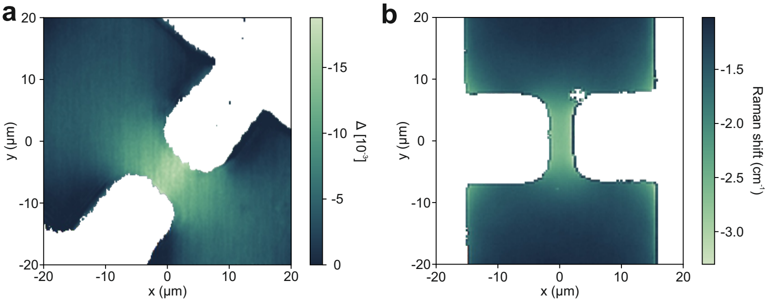

Figure 5.6: a μRAS map at 2.21 eV (resonance frequency of the spectra in Figure 5.5**b**) of the micro-bridges showing the $\epsilon_{xx} - \epsilon_{yy}$ strain distribution. The bridges are oriented at 45° to align with the polarisation axis of the PEM and polarizer/analyzer. **b** Raman shift map of the micro-bridges, proportional to $p\epsilon_{zz} + q(\epsilon_{xx} + \epsilon_{yy})$.

To further assess the strain mapping capabilities of our microscope, we

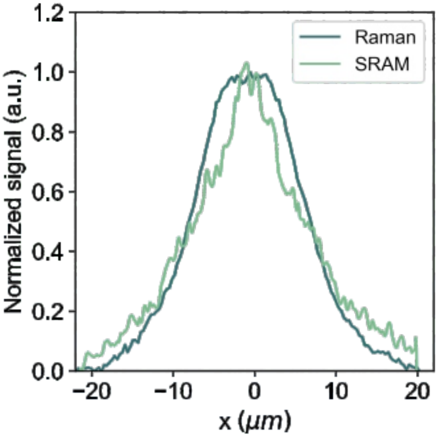

Figure 5.7: Signal profile across the bridge scanned in Figure 5.6 for both Raman and SRAM setups.

compare with an established optical technique for strain mapping: Raman spectroscopy. Figure 5.6b shows a map of the Raman shift for the same microbridge as in Figure 5.6a and Figure 5.7 plots the SRAM signal and Raman shift across the bridge. Details of the experimental procedure for Raman spectroscopy can be found in Chapter 3. As can be observed, the Raman shift follows a slightly different distribution than the one measured with SRAM. This discrepancy is due to the different strain linear combinations that these two techniques probe. While SRAM is proportional to $\epsilon_{xx} - \epsilon_{yy}$, the Raman shift is proportional to $p\epsilon_{zz} + q(\epsilon_{xx} + \epsilon_{yy})$ [53], where p and q are the Raman tensor coefficients.

Analyzing complex strain states using Raman spectroscopy generally requires the usage of FEM simulations to decouple the different strain components. However, for plane stress, the combined use of SRAM ($\propto \epsilon_{xx} - \epsilon_{yy}$) and Raman ($\propto \epsilon_{xx} + \epsilon_{yy}$) would allow to decouple ϵ_{xx} and ϵ_{yy} without the assistance of FEM simulations.

While both SRAM and Raman microscopy provide a way to infer the mechanical state of the sample, the underlying mechanisms are intrinsically different. SRAM directly probes the anisotropy in the dielectric permittivity tensor while Raman spectroscopy probes the vibrational levels of the crystal lattice that present a change in polarizability. As such, SRAM offers direct insight into the optical properties of the sample and has access to a broader range of materials, e.g. metals, for which a case study is presented in the next section.

5.3 Metals

5.3.1 Strain Sensitivity

Similar to $m3m$ semiconductors, density functional theory calculations have shown that the strain sensitivity arises from polarization dependent interband transitions [17]. However, unlike Germanium or Silicon, it is often the case that metals exhibit a polycrystalline microstructure, which can be either textured or random, with average grain size significantly smaller than the focal spot of the light beam. In such a scenario, the measured optical signal is an average over all the grain orientations such that the photo-elastic tensor becomes a scalar and equation 2.6 becomes a scalar relation.

To this extend, we apply SRAM to strained gold films. Due to their excellent optical, electrical and mechanical properties, gold films are readily used in flexible electronics. To produce films that better simulate conditions typically found in these flexible devices, we refrained from template-stripping in the fabrication of the films.

Figure 5.8a shows a set of SRAM spectra as a function of strain of a 500 nm thick gold film sputtered on polyimide (Kapton E), which presents a Poisson's ratio similar to that of gold. The characteristic peak at 2.44 eV in all spectra (Figure 5.8a) corresponds to the interband transition near the high symmetry point L between states in the 5d and 6sp bands of gold [111, 112]. Similar to the case of semiconductors, the amplitude of the resonance peak (Figure Figure 5.8b) scales linearly with strain in the elastic regime. However, in the case of metals for strains higher than the yield point one has to take into account plastic deformation and its effect on the strain sensitive signal.

In the plastic regime, the reflectance anisotropy signal should eventually saturate as further strain generates dislocations but does not increase the lattice spacing, which is the origin of the photoelastic effect. Instead, further increases in signal after the film yields are due to the creation of anisotropic defects that introduce a global offset to the spectra in the bandwidth of the SRAM [64, 113]. These contributions are low in the elastic regime but are significant in the plastic regime, specially for sputtered thin films that have increased roughness compared to template stripped films or epitaxial semiconductors.

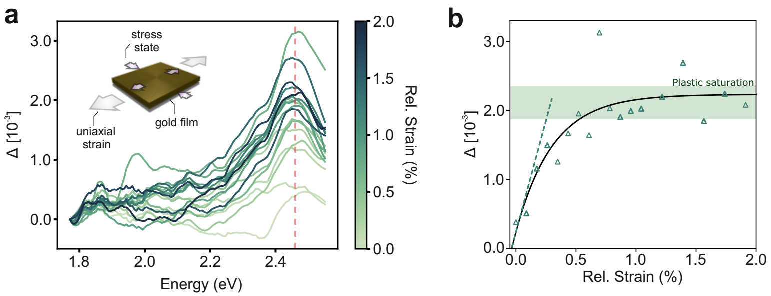

Figure 5.8: a SRAM spectra of an externally strained gold film deposited on a polyimide substrate (Kapton E) as a function of strain showing a resonance at 2.44 eV. **b** SRAM signal at 2.44 eV as a function of strain. An exponential function derived from the constitutive law of Voce (equation 5.1) provides the best fit for both the linear elastic regime and the plastic saturation regime (indicated in light green).

To uncover the signal stemming from strain in the plastic regime, we introduce a correction term at 1.77 eV, far from resonance where the spectra should coincide. Figure 5.9 plots the offset term as a function of strain, showcasing the elastic and plastic regime and how the correction increase with plastic deformation.

The constitutive law of Voce describes the stress-strain relation in the presence of strain hardening. We use an analogue to this equation, already introduced in reference [114, 115], to fit the SRAM-strain relation (Figure 5.8b):

$$\Delta r/r(\varepsilon) = \Delta r_\infty - (\Delta r_\infty - \Delta r_0)e^{-\frac{\kappa}{\Delta r_\infty - \Delta r_0}\varepsilon}, \tag{5.1}$$

where Δr_0, Δr_∞ and κ work as a reflectance anisotropy analogues to the stress parameters in the Voce equation. Δr_0 is the anisotropy signal at the initial strain state of the film, Δr_∞ is the signal at the plastic saturation plateau and κ is the initial slope. κ represents the constant of proportionality between the reflectance anisotropy signal and elastic strain and, therefore, can be related to the photoelastic tensor of gold. Since at the resonance frequency $\Im\{\Delta r/r\}$ is maximum while $\Im\{\Delta r/r\} \simeq 0$, we can approximate the average photoelastic constant of gold as

$$\overline{P} = W\frac{(1-\varepsilon)}{\varepsilon^{3/2}} = 0.18 - 0.30i. \tag{5.2}$$

$\overline{P} = 0.18 - 0.30i$ corresponds to $\overline{W} = -6.35 - 3.42i$, which is in the same order of magnitude as the only other values for gold reported in literature

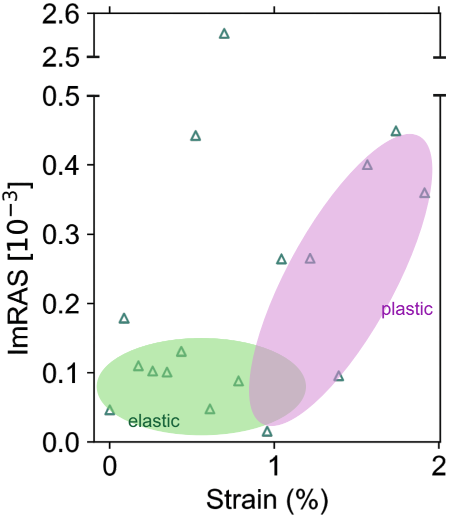

Figure 5.9: Offset correction term as a function of strain showing the increase in noise correlated to the onset of plastic deformation.

using surface Brillouin scattering [116]; $W_{11} = 42 - 4i$, $W_{12} = 53 - 15i$ and $W_{44} = -5.5 + 5.5i$ at $\omega = 2.41eV$ with $W_{11} - W_{12} \sim 10^1$. Here, a different definition of the elasto-optic tensor with direct proportionality, $\Delta\varepsilon = W\epsilon$, is used. The differences between $\overline{W}$ and $W_{11} - W_{12}$ could stem from sample microstructure (as $\overline{W}$ is an averaged value) to the sensitivity of the measurement techniques.The measured value of $\overline{P}$ is also within the same order of magnitude for values of $p_{11} - p_{12}$ for other materials reported in reference [47]. Nonetheless, given the noise of the measurement and its dependence on the film and substrate properties, further experiments are needed to determine the elasto-optic properties of gold.

5.3.2 Strain mapping

In order to showcase the capabilities of SRAM to map strain in metals, we test more complex metallic structures with a spatially anisotropic strain distribution. We fabricate a double wedge microstructure using FIB milling that introduces a strain distribution when externally applying uniaxial tension (Figure 5.10c). Such a structure should generate a strain concentration at the wedge gaps and strain relaxation close to the edges perpendicular to the strain direction (see Figure 5.10c). Applying a strain lower than the elastic limit (strain direction indicated with a double arrow in Figure 5.10c) ensures that plastic saturation is not reached so that the SRAM map is proportional to the strain distribution. Figure 5.10d shows the SRAM map at 2.44 eV, where the optical response has been suppressed at the FIBed structure. This is done to filter artefacts generated by the metal edges, which break the symmetry of the focal spot. An in depth review of the artefacts introduced by edges when using the SRAM setup can be found in Chapter 4. As can be seen, the SRAM map shows the expected concentration and relaxation of strain around the double wedge structure.

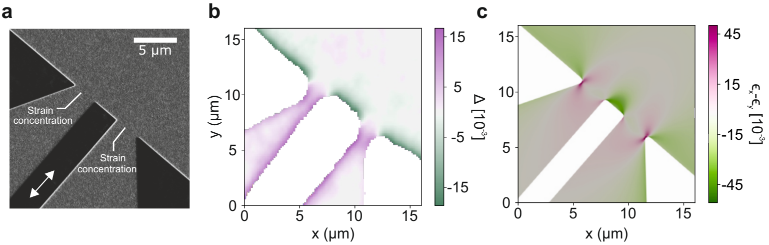

Figure 5.10: FIBed double wedge structure **a** and the resulting strain distribution, obtained with both the SRAM setup (**d**) and FEM simulations (**e**). The strain direction is indicated with an arrow in **c** together with the expected zones of strain concentration and relaxation.

To further validate our experimental results, we carried out FEM simulations of the strain distribution generated by the FIBed structure (Figure 5.10e) and find good agreement with the measured SRAM map. The regions with strain concentration/relaxation are reproduced by the measured SRAM strain distribution. The SRAM data does, however, show that the strain concentration/relaxation induced by the double wedge structure decays faster compared to FEM simulations. This is explained by the polyimide film being two orders of magnitude thicker than the metal film, thus dominating the mechanics of the system.

In a system comprised by a metallic thin film and a substantially thicker substrate (in this case 100 times greater), the substrate dominates the mechanical response of the system. As such, the stress experienced by the metallic thin film is transferred from the substrate. The transfer rate depends on the ratio of mechanical properties between the film and the substrate. This is effect is easier seen in regions near film edges where the free surface is relaxed and presents no stress (normal to the free surface) while at a sufficient distance away from the edge the film reaches the stress level transferred by the substrate. The stress curve as a function of distance from the free surface is exponential and is characterized by a length parameter dependent on the thin film's thickness and the elastic mechanical properties of the film and substrate. We employ the following linear shear lag model to calculate the characteristic length of our gold-polyimide system [117]

$$l = \frac{\pi}{2} g\left(\alpha, \beta\right) h, \tag{5.3}$$

where l is the reference length, h the film thickness and $g\left(\alpha, \beta\right)$ is a function of the Dundurs parameters α and β representing the mismatch in elastic mechanical properties between substrate and film [118]. Using the values $h = 500$ nm and $g = 5.17$ (for $\alpha = 0.878$ and $\beta = 0.250$) we obtain the reference length $l \simeq 4\ \mu$m, which is in very good agreement with the strain decay observed in the SRAM map.

The higher roughness (sub-wavelength) and polycrystallinity of sputtered metals in comparison to typical semiconductor surfaces translates to an increased noise level in the SRAM signal and slightly reduces the high strain sensitivity of the technique. However, the noise is not structured and is, therefore, mitigated by the spatial mapping of the setup. As seen by the good match between the SRAM maps and FEM simulations the noise does not impede an accurate characterization of the strain distribution.

5.4 Amorphous semiconductors

5.4.1 Strain Sensitivity

While amorphous materials don't exhibit long range order, uniaxial strain still influences the inter-atomic distance and, therefore, should also introduce a change in reflectivity. We evaporate a 300 nm germanium film on polyimide (Kapton E) to show the sensitivity of SRAM to amorphous semiconductors. Figure 5.11 shows the X-ray diffractogram and Raman spectrum of the films, which present characteristic broad peaks of amorphous germanium [119].

Figure 5.12 shows the RAS spectra of the a-ge film as a function of strain. Uniaxial tension is externally applied to the a-ge film, loading and unloading, and the RAS spectra at different strain stages are recorded, see Chapter 3 for more information on the experimental procedure. As can be seen, the RAS spectra don't exhibit any resonance and instead present a very broad response with the spectra offsetting as a function of strain.

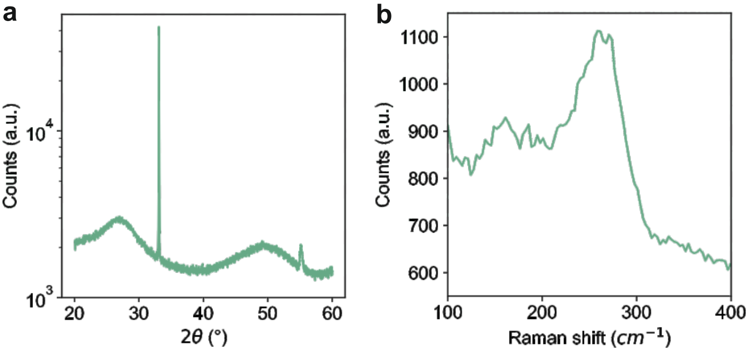

Figure 5.11: X-ray diffractogram (**a**) and Raman spectrum (**b**) of a 300 nm germanium film on polyimide showcasing the amorphous nature of the film.

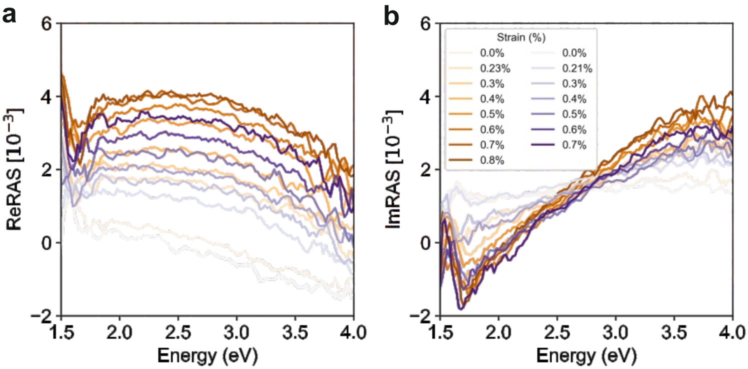

Figure 5.12: Real (**a**) and imaginary (**b**) part of RAS spectra taken at sequential tensile loads on a 300 nm amorphous germanium thin film on polyimide. Loading is color coded in brown while unloading is coded in blue.

While global offsets have been observed in the plastic regime for metals [64], the offset of the a-ge film is recovered upon unloading. Given the brittle nature of germanium, it could also be the case that the film cracks orthogonally to the strain direction and these give rise to a RAS signal. However, cracks have also been shown to be wavelength dependent [64, 114] (due to the geometric nature of the cracking) while the response presented here is broader and wavelength independent (for the real part). Instead, it is assumed that a-ge has its ε critical points shifted outside the wavelength range of the setup compared to c-ge (see Figure 5.13) and this causes a strain sensitive global offset in the RAS spectra.

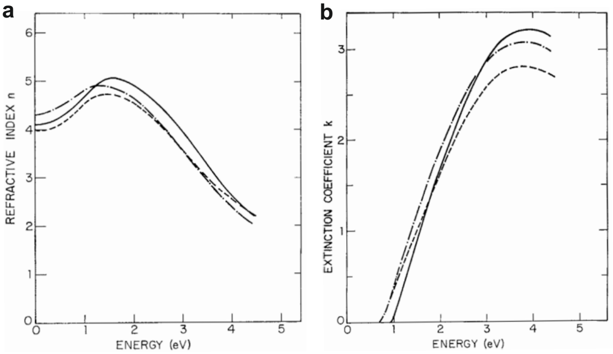

Figure 5.13: Real (**a**) and imaginary (**b**) part of the refractive index of 30 μm amorphous germanium sputtered at different substrate temperatures. Continuous line corresponds to 350°C, pointed and dashed line to 25°C and dashed line to reference [120]. Reprinted from [121] with permission from Taylor & Francis.

5.4.2 Strain Mapping

A photonic crystal inspired structure is milled onto the a-ge film with FIB in order to create an anisotropic strain distribution that can be characterized with the SRAM setup. We then externally apply uniaxial tension with a manual stage (see Chapter 3 for more information) and record the SRAM map. Figure 5.14 shows the recorded SRAM map (**a**) and the FEM simulations of the structure. As can be observed, the SRAM signal distribution is in very good agreement with the strain distribution calculated with FEM simulations, confirming the strain sensitivity of the setup to amorphous germanium.

It can be noted that if the RAS signal shown in Figure 5.12 is due to cracking of the film then the SRAM signal in Figure 5.14 would show more localization. This fact supports the hypothesis that the broader dielectric response of a-ge is responsible for the non-resonance nature of the strain induced RAS signal. Nonetheless, further experiments are needed to confirm such hypothesis.

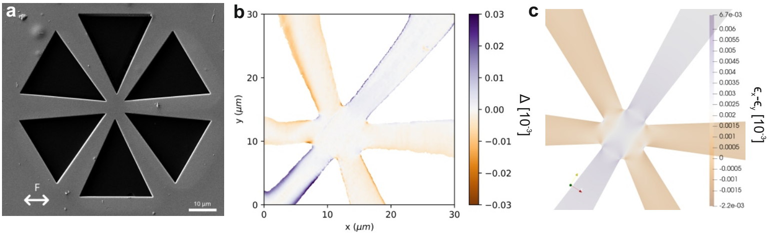

Figure 5.14: FIBed structure **a** and the resulting strain distribution, obtained with both the SRAM setup (**b**) and FEM simulations (**c**). The strain direction is indicated with an arrow in **a**.

Characterization of Nanoantennas | 6

In this chapter the SRAM signal of plasmonic nanoresonators is discussed. As explained in Chapter 2, the polarization selectivity of plasmonic nanoantennas gives rise to a dipolar resonance, which is dependent on the geometrical parameters of the antennas. As such, the strain-induced geometrical change of the antennas can be considered a model system that mimics the strain-induced symmetry breaking in conventional materials. Specifically, the observed shift in the dipolar resonance of the antennas can be seen as an analogue to the energy shift of the dipolar transitions at the high symmetry points of the band structure of conventional materials [17], typically described within the framework of deformation potential theory. Therefore, the nanoantennas presented in this chapter provide both the means to expand the range of materials by using strain markers and an excellent case study to showcase the phase sensitivity of the setup. This chapter includes an analysis of the SRAM properties of the nanoantennas, their strain sensitivity and the potential of the microscope to aid in the design of phase sensitive metamaterials.

6.1 RAS on nanoresonators 57
6.2 Design 60
6.3 Nanoantenna characterization with SRAM 61
6.3.1 Array size sensitivity 63
6.4 Strain markers . . 66
6.5 SRAM as a phase characterization technique 68

Parts of this chapter are based on the article titled *"Scanning Reflectance Anisotropy Microscopy for Multi-Material Strain Mapping"* by J. Sendra, F. Haake, M. Calvo, H. Galinski and R. Spolenak [33] currently under review in *Advanced Functional Materials*. Individual author contributions can be found in the declaration chapter.

6.1 RAS on nanoresonators

While there has not been a specific interest to study nanoantennas in the RAS community, the encounter of plasmonic interactions in nanoresonators is not uncommon in the community. RAS has been extensively used to study the properties of surfaces during growth [35, 38, 41, 122] while the emergence of islands during the initial stages of thin film growth introduces resonances to the RAS signal. Such resonances have been studied for a variety of materials, *e.g.* In [123], InAs [124] or Ag [125–127].

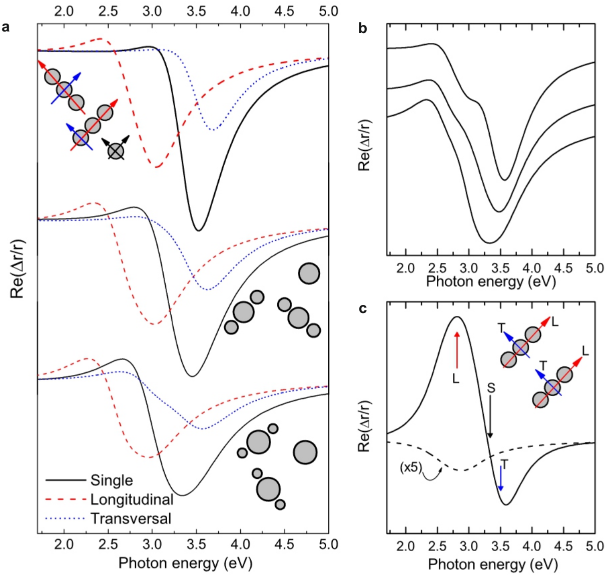

Figure 6.1: Calculations of the RAS lineshape for different truncated aggregates of silver nanoparticles (**b**) and the different contributions for each mode and single particle mode (**a**). **c** Calculated spectra for a chain of particles. Reprinted from [125], open access.

While the formation of silver clusters during thin film growth should be of particular interest — since it should provide an excellent case study for plasmonic resonances as the conductive properties of silver make it one of the most used plasmonic materials [128, 129] — analyzing the RAS signal arising from the island formation is often a complex issue. This is due to the presence of more anisotropy inducing phenomena, *e.g.* surface reconstruction and surface electronic states, which can change for each growth stage, even from adding a single monolayer [130].

Nonetheless, it can be seen that geometrical factors are driving the lineshape of the resulting signal, indicating the strong influence of the plasmon resonances. Figure 6.1 shows the calculated spectra for three different aggregates of silver nanoparticles [125], in which the shape and gap between particles determine the overall lineshape. Interestingly, the authors calculated the signal resulting from the two main plasmonic modes (longitudinal and transversal) so one can see that the aspect ratio of the resonators seems to have a strong influence on the broadening and position of the resonance (Figure 6.1b).

All the aforementioned studies are done on small particles with at least one of their dimensions ~ 0.5 – 5 nm, where the electronic structure could be distinct from that of bulk and affect the RAS signal, for example as is the case in quantum dots [131], nanoribbons [132] or silver nanodots [133]. Instead, Calvo grew silver islands by de-wetting of an epitaxially grown film on MgO single crystals [64] and transferring the film to polyimide, resulting in oriented anisotropic islands with dimensions in the tens of nanometers on a flexible substrate. The islands present a plasmonic resonance that shifts linearly with film thickness and that increases amplitude and presents a very slight shift upon straining. While the origin of the strain signal is not yet clear, simulations seem to indicate that the change in gap between islands is the main driving factor.

Furthermore, RAS has also been used to monitor the growth of self-assembling silver nanoparticle arrays by glancing angle deposition [134–137]. In this case the anisotropic signals stems both from the slight ellipticity of the particles as well as their distribution in the sample. While by changing the deposition temperature it is possible to control the ellipticity of the particles, with an observed blue shift for more spherical particles (or smaller aspect ratio), the size of the particles is also changing and the blue shift cannot be attributed only to the aspect ratio change.

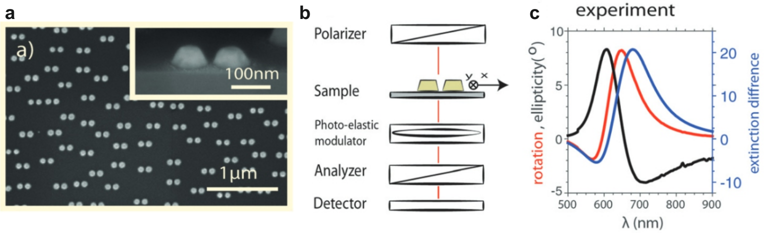

Figure 6.2: Transmittance anisotropy spectroscopy of dimer antennas. **a** SEM micrograph of the gold dimer antennas fabricated with lithography. **b** Schematic of the TAS setup. **c** Rotation and ellipticity (analogue to Ψ and Δ) measurements of the dimers seen in **a**. Adapted from [138] with permission from the Royal Society of Chemistry.

Lastly, a similar technique to RAS but in transmission (transmittance anisotropy spectroscopy) has been used to characterize lithographically fabricated gold dimer antennas [138]. Figure 6.2 shows the fabricated antennas (**a**) and the measured rotation and ellipticity of the sample (analogous to Ψ and Δ, **c**). The authors use the sensitivity of the antennas to a change in refractive index of their surroundings, especially in the antenna gap, to sense concentration of neutravidin. These experiments indicate there is high potential for RAS as a polarization sensitive technique.

6.2 Design

The antennas' dimensions are chosen such that the resonance falls within the measurement range of the microscope (1.77 eV - 2.55 eV), which corresponds to a length of 100 nm, width of 50 nm and a pitch of 150 nm. However, unlike the antennas and islands presented in section 6.1, the antennas presented in this chapter are milled into the film instead of being built up on the substrate. This allows easier fabrication (use of the FIB instead of a complex lithography process) and also ensures the antennas are strained as homogeneously as possible so that strain is not concentrated at the gaps between antennas, as was the case in reference [64].

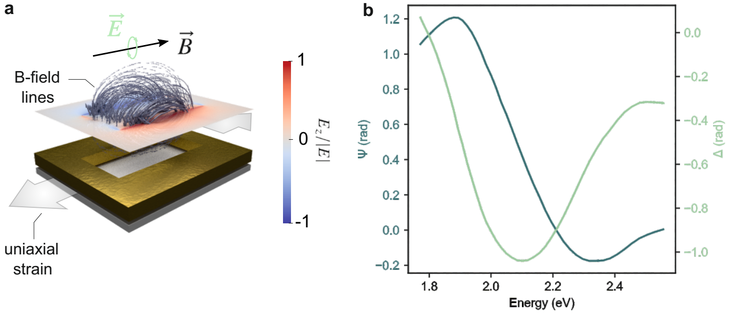

Figure 6.3: FEM simulations of a babinet nanoslot antenna. **a** Electric and magnetic field distributions around the antenna showcasing the magnetic dipolar nature of the antenna. **b** Simulated RAS signal presenting a resonance peak at 2.1 eV.

As the antennas are milled into the film, they exhibit a magnetic dipole moment instead of the electric dipole moment observed in typical nanorod antennas [139, 140]. This is due to Babinet's principle of complementary, in which diffraction from a solid body presents the same characteristics as its hollow counterpart but with the roles of the electric and magnetic field exchanged in the case of localized surface plasmon resonances, even presenting a higher magnetic field enhancement [141]. Figure 6.3a shows the normalized electric field intensity and magnetic field lines calculated with FEM simulations of the slot antennas, confirming their magnetic dipolar nature. It is also seen how the charge density is concentrated at the edges of the antenna and then decays further into the film. Since the simulation was performed with periodic boundary conditions, simulating an infinite array of antennas, this means that the gap between antennas is big enough to avoid inter-antenna coupling. As such, when the antennas are strained in section 6.4, strain direction indicated with arrows in Figure 6.3a, the influence of the gap widening can be neglected.

As seen in Figure 6.3b for Δ, which indicates the position of the resonance, the FEM simulations show a resonance at 2.1 eV while Ψ presents a differential shape also centered at 2.1 eV with influence points around 2.35 eV and 1.9 eV. Surprisingly, the simulated RAS signal has a magnitude in the order of $\sim 10^{-1} - 10^{0}$, far higher than anticipated and that is typically measured in RAS experiments (a signal of $\Psi = 1.2$ would imply $r_x \simeq 2.6 r_y$). It is assumed that the higher collection angle of the simulation (due to the boundary conditions) and ideal shape of the antennas increase the coupling efficiency of the localized surface plasmons. It is also important to note that the simulations are performed with the input light (and output) being linearly polarized instead of being in the complex time modulated polarization state after passage through the photoelastic modulator. This significantly eases the computational costs of the simulation while still providing a good qualitative approximation of the results.

6.3 Nanoantenna characterization with SRAM

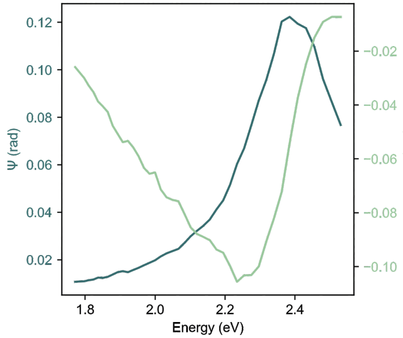

Figure 6.4: SRAM spectrum of a babinet nanoslot antenna fabricated on a 100 nm gold template stripped film.

Figure 6.4 shows the SRAM spectrum of a nanoslot antenna measured on a 10x10 array of antennas. As can be seen, the resonance is slightly blue shifted when compared to the simulations (Figure 6.3). It is also noticeable that Ψ seems to be flipped with respect to the simulations, with the highest influence point around 2.4 eV. A broadening of the resonance is also noticeable, presumably due to the imperfections in the antennas due to the fabrication process. Nonetheless, the measurements have good qualitative agreement with the simulations, confirming the measured resonance has a magnetic dipolar origin.

The antennas measured in Figure 6.4 are fabricated on a 100 nm templated stripped film on polyimide. This is done to increase the quality factor as using a template-stripped film results in ultrasmooth surfaces with increased optical quality and plasmon propagation length [142], see Chapter 3 for more details on the fabrication. This can be clearly observed in Figure 6.5, where two spectra taken on template stripped film (**a**, top) and as deposited film (**a**, bottom) are compared. The spectra are normalized and shifted for an easier comparison.

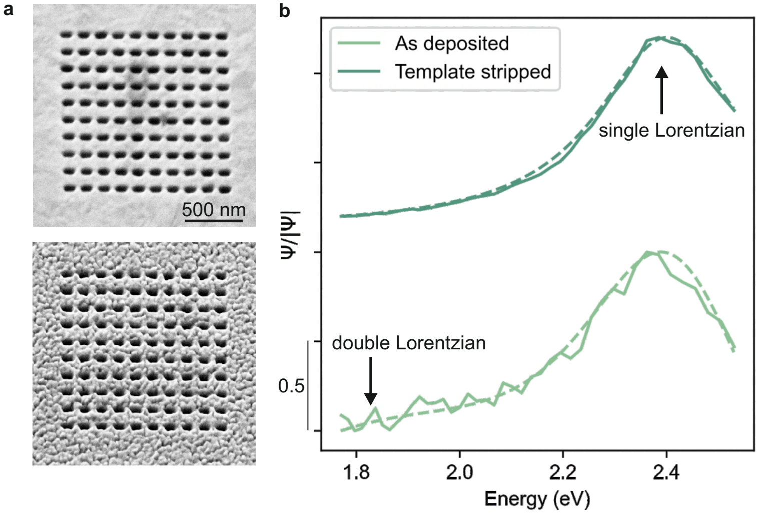

Figure 6.5: Comparison of the SRAM spectra taken on a template stripped film and an as deposited film, showcasing the increase in optical quality and reduced broadening. **a** SEM images of the two arrays, template stripped (top) and as deposited (bottom). **b** SRAM spectra taken of each array, template stripped (dark green, top) and as deposited (light green, bottom).

It is trivial to see in the SEM micrographs (Figure 6.5a) that the template stripped film is far smoother, resulting in the antennas presenting a much more uniform shape compared to the as deposited film. The increased roughness is translated into a noisier and broader resonance when measuring with the SRAM setup. While it is difficult to appreciate that in Figure 6.5b, the calculated linewidth from the fitting shows a broadening for the as deposited film. The following Lorentzian lineshape, typical for dipolar resonances, is fitted to the measured spectra (dashed lines in Figure 6.5b)

$$\Psi(\omega) = \frac{A_1}{\pi}\frac{\gamma_1}{(\omega-\Omega_1)^2+\gamma_1^2} + \frac{A_2}{\pi}\frac{\gamma_2}{(\omega-\Omega_2)^2+\gamma_2^2}, \tag{6.1}$$

where the set of parameters (A,γ,Ω) — amplitude, linewidth, and resonance frequency, all expressed in units of energy — describes each resonance. Interestingly, one single Lorentzian oscillator fits the template stripped resonance while it is not possible to fit the as deposited resonance with just one oscillator. Instead, a second extra oscillator close to 1.8 eV is needed in order to find a fit, indicating there could be a feature at low energies stemming from antenna imperfections. The fitted linewidths are $\gamma_{ts} = 0.16$ eV and $\gamma_{ad} = 0.24$ eV for the template stripped film and the as deposited film respectively, showing that the as deposited resonance is significantly broader with $\gamma_{ad}/\gamma_{ts} = 1.5$.

Figure 6.6a plots the SRAM spectra for an array of antennas as a function of angle (with respect to the lab frame). While this experiment is done on the as deposited antennas, increasing the overall noise, it is still possible to see the angular dependence of the antennas. As expected, the antennas present the same symmetry as the system and, interestingly, a slightly modified Malus law (Equation 6.2), such that $|\Psi| = 0$ at both 0°and 90°, provides the best fit to $|\Psi|$, indicating the sensitivity of the antennas to linearly polarized light.

$$|\Psi|(\theta) = \cos^2(2\theta - \theta_0) \tag{6.2}$$

6.3.1 Array size sensitivity

So far the measured SRAM spectra have been taken on 10x10 antenna arrays, which assures the beam spot is smaller than the array and completely covered with antennas, effectively simulating an infinite array. However, such arrays are large and would introduce a significant resolution loss if used as a strain marker, so it is of interest to investigate the SRAM signal for smaller arrays. To this extent, we engineer a set of antenna arrays with varying antenna numbers, from a 7x7 array down to a single nanoantenna. Figure 6.7a shows the scan of the entire region of the unstrained nanoantennas with the microscope at a single frequency, mapping the optical anisotropy. The frequency has been matched with the resonance frequency of a single antenna (ω = 2.39 eV). Remarkably, the microscope resolves the optical anisotropy down to a single nanoantenna (zoomed in region in Figure 6.7a), highlighting the excellent anisotropy sensitivity of the setup. The response of

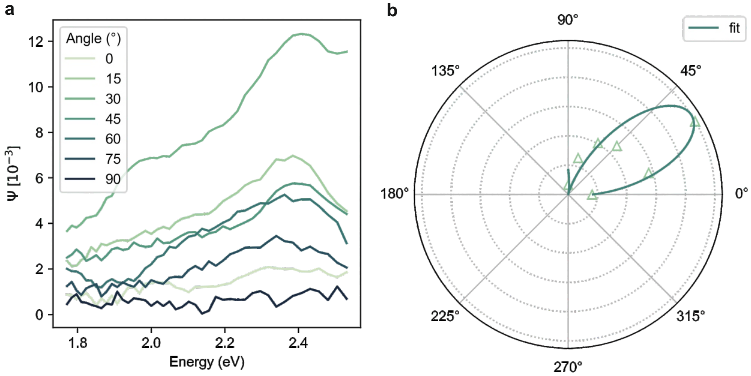

Figure 6.6: Angular dependence of the SRAM signal of an array of nanoslot antennas, showcasing the sensitivity of the setup the alignment of the antennas. **a** Spectra of the antennas at different angles and polar plot **b** of the peak intensity. The polar plot is fit with a modified malus law (Equation 6.2).

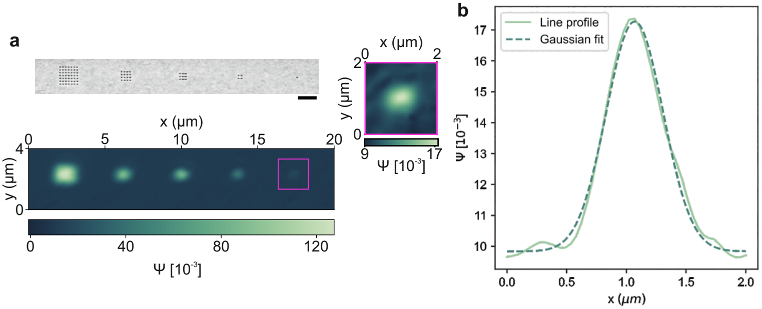

Figure 6.7: **a** Antenna arrays of varying length (scale bar is 1 μm) and the resulting SRAM map in an unstrained state showcasing the single antenna sensitivity of the setup. **b** Line profile of the scan in **a** fitted with a gaussian function. The full width half maximum of the fitted gaussian is 560 nm.

a single nanoantenna, given by the convolution of the point spread function of the antenna and the microscope, enables us to calculate the lower limit to the resolution. Figure 6.7b shows the intensity profile across the single antenna map (linearly interpolated). Fitting a Gaussian profile yields a full width half maximum of 560 nm, as is shown in Chapter 4. The measured resolution is very close to the theoretical resolution confirming that the optical setup is diffraction-limited.

As expected, the intensity of the SRAM signal decreases with decreasing array size. Figure 6.8a shows the SRAM spectra taken for the differently sized

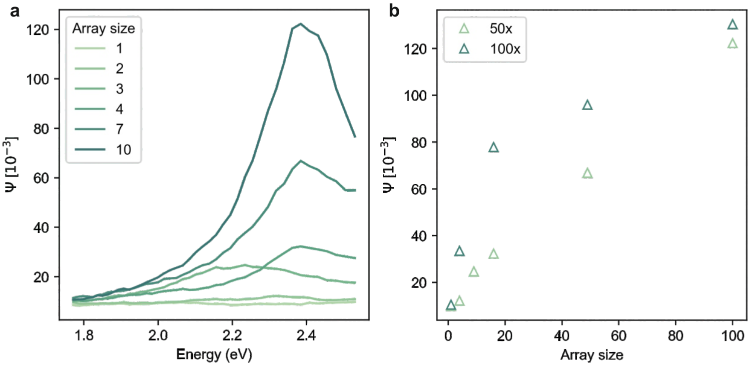

Figure 6.8: a SRAM spectra of nanoslot antennas as a function of arrays size for a 50x objective. **b** Evolution of the peak intensity as a function of array size for two different objectives, 50x (0.5 NA) and 100x (0.8 NA), showcasing the effect of antenna coverage in the beam spot.

arrays, with the spectrum of the 3x3 array being red shifted due to a defect in fabrication (see Figure 6.7a). Figure 6.8b shows a comparison of the peak intensities as a function of array size for two the two different objectives, 50x (0.5 NA) and 100x (0.8 NA). Even though they are not shown here, the spectra taken with the 100x show exactly the same lineshape, indicating that the increase in incidence angle due to the higher numerical aperture has no effect on the resonance of the antennas. While Chapter 4 covers the cancellation of artefacts due to the symmetry of the system, in this case the increased angle could have an enhanced effect due to the typical angular dependence of metasurfaces. One can also observe that the peak intensity saturates faster with the 100x objective, as is expected due to its smaller beam spot size.

Even though probing a single nanoantenna is challenging as the antenna is not visible through the imaging optics of the system (for both objectives), the scan at a single wavelength still reveals the single antenna sensitivity of the setup. While single particle or antenna measurements are not a rare occurrence in the literature [143, 144], these are usually done employing dark field microscopy, where the scattered light is analyzed. In contrast, the SRAM setup measures the anisotropy over the total reflected light, which provides alternative information that could be used in conjunction with scattered light measurements.

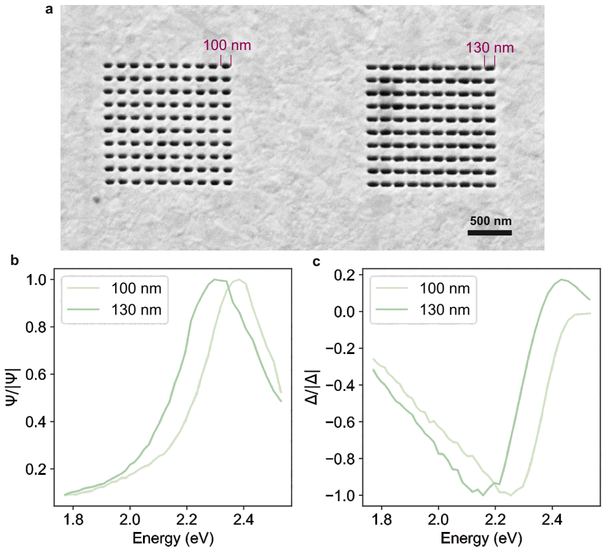

Figure 6.9: a SEM image of two antenna arrays of length 100 nm (left) and 130 nm (right). Their SRAM spectra are plotted in **b** for the real part and **c** for the imaginary part. The longer antennas showcase a significant red shift of -0.10 eV.

6.4 Strain markers

As the nanoantennas present a dipolar resonance that is dependent on their geometry, the antennas could function as strain markers, in an analogous way to the resonances used for strain sensing (see Chapter 5). Adapting the antenna's dimensions depending on the refractive index of the film would to expand the range of materials the SRAM setup is sensitive to. Figure 6.9 shows the SEM image of two arrays with different antenna length, 100 nm and 130 nm, and their corresponding SRAM spectra. As can be seen, there is a significant red shift of the resonance (-0.10 eV) for the longer antennas. However, as the longer antennas have an 30% increased length and assuming a linear shift, this would imply a shift of ~ -3 meV for a 1% strain, which could limit the functionality of the antennas as strain markers. It is also noticeable that there is no broadening of the spectra due to the change in aspect ratio.

The antennas have been template stripped onto a polycarbonate film such that strain can be externally applied as polycarbonate is a flexible substrate that allows for a controlled deformation of the metallic thin film and the

FIBed antennas. Similarly to fabricating the antennas with increased length, uniaxial deformation of the antenna also changes the ratio between the longitudinal and transversal axial lengths. However, in this case the aspect ratio is influenced by both the elongation along the strain axis and the resulting shortening along the orthogonal axis due to Poisson's effect.

To mechanically deform the nanoantennas, the flexible substrate is clamped in a tensile stage and strained until a flat profile is obtained so that the light beam illuminates at normal incidence on the film. The film has an undetermined initial strain state and all subsequent strain measurements are given relative to the initial strain state. Figure 6.10a shows the SRAM spectra of an antenna array taken for 5 incremental strain states. Since the antennas are magnetic dipoles, their line shapes can be represented by a Lorentzian (equation 6.1). The fitted Lorentzian line shapes shown in Figure 6.10a are in excellent agreement with the experimental spectra. Despite the small deformation, the resonance frequency at 2.39 eV shifts to longer wavelengths with increasing strain up to a shift of $\Delta\Omega_1 = -37.7 \pm 3.52$ meV, corresponding to a strain sensitivity of $\kappa = -20.9 \pm 1.53$ meV/%.

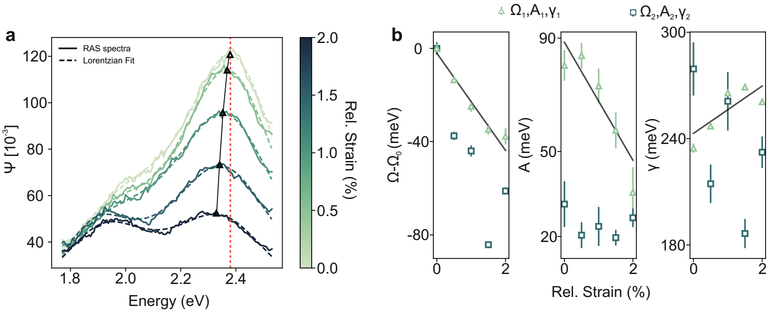

Figure 6.10: **a** SRAM spectra of a strained antenna array of 7x7 (shown in Figure 6.7a). Increasing strain states are indicated with different colours (green to black). The resulting spectra are fitted with a double Lorentzian function (equation 6.1). **b** Strain dependence of the fitted parameters (resonance shift $\Omega_{1,2} - \Omega_0$, amplitude $A_{1,2}$ and line width $\gamma_{1,2}$) of the double Lorentzian function, showcasing the strain sensitivity of the primary eV resonance.

The strain induced shift is higher than is expected from the length variation measurements. This could be due to two factors. The first one is that the aspect ratio change due to straining is more pronounced due to Poisson's effect. The second one is that strain also enlarges the gap between antennas, although simulations have shown that the gap does not have a strong influence. The decreased gap of the 130 nm long antennas (Figure 6.9) is probably a major factor influencing the observed increased red shift. Nonetheless, the spectra shown in Figure 6.10 clearly demonstrate that the antennas provide enough sensitivity for strain sensing. Moreover, the shift is also observed to be linear with strain (Figure 6.10b), which fits expectations of plasmonic nanorod antennas [61].

A closer look on the amplitude and line width of the central peak reveals that, while the amplitude is decreasing, the line width is increasing resulting in an overall broadening of the resonance with increasing strain. This is due to the mechanical deformation of the nanoresonators. While elongation of the longitudinal axis of the antennas leads to the reported red-shift of the resonance, the small mismatch in Poisson's ratio between the polycarbonate substrate and the gold film and the induced deformation on the film lead to a non-homogeneous shape change of the resonators. Cracks and considerable surface deformation are observed for strains higher than 2%, when the resonance is not observable anymore. A second resonance at 1.98 eV is also observed. This resonance does not show a conclusive strain dependence in any of the fitted parameters and is presumably related to the onset of plastic deformation. This hypothesis is also supported by the measurements on an as deposited film in Figure 6.5 that show a small contribution at lower energies due to defects. Nonetheless, more experiments are necessary to determine with certitude the origin of the low energy feature.

6.5 SRAM as a phase characterization technique

Flat optics [145, 146] have become a hot-topic for their ability to control the wavefront using plasmonic antenna arrays. However, the visualization of the phase field is usually performed with simulations. Instead, SRAM could provide local probing of the phase rotation, hence becoming an excellent technique for metasurface characterization.

To illustrate the phase sensitivity of the microscope, we designed an optically anisotropic metasurface based on the nanoslot antennas discussed in previous sections that exhibit a dipolar resonance in the spectral range of the setup. Figure Figure 6.11a depicts the metasurface containing an arrangement of antennas with an outer-ring made of horizontally oriented antennas and an array of vertically oriented antennas of the same size. Altering the nanoslot antennas' dimensions, pitch, and orientation not only places the resonance inside the spectral range of the setup but would also allow to engineer the ellipsometric parameters of the sample (Ψ,Δ), in a similar way to v-shape antennas [147].

Figure 6.11b-c shows the SRAM (Ψ, Δ) map of the nanoslot antenna arrangement at the resonance frequency of 2.39 eV, displaying the symmetry

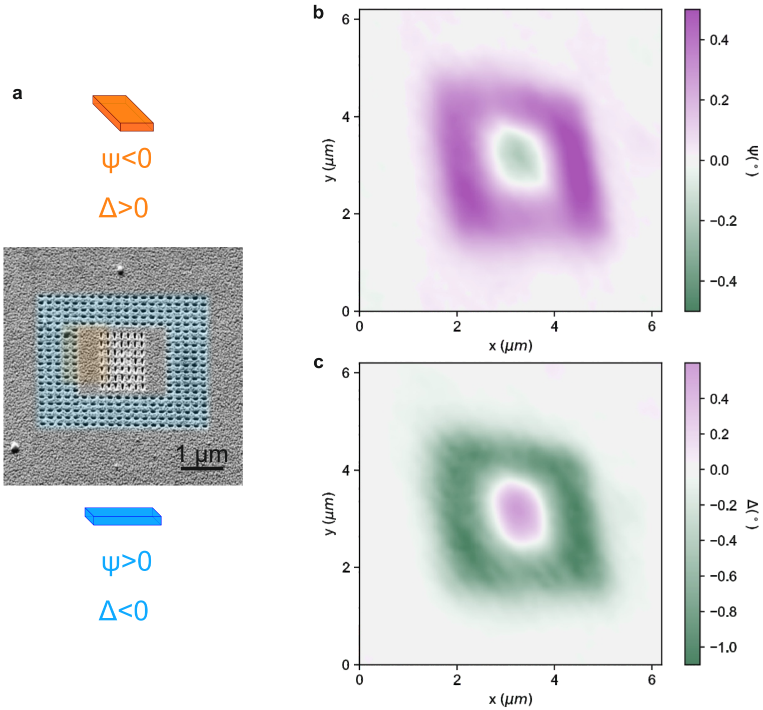

Figure 6.11: SEM image **a** and SRAM measurements of a metasurface composed of dipolar slot antennas showcasing the sensitivity of the setup to the ellipsometric properties (phase Δ **c** and amplitude Ψ **b**) of the sample. Phase sensitivity lower than 1° is achieved.

breaking of the metasurface. As can be seen, SRAM allows access to local phase information by measuring the ellipsometric parameters of the sample. These measurements showcase the high phase sensitivity of the technique, able to distinguish phase differences smaller than 1° at diffraction-limited resolution. Given the noise measurements in Chapter 4, the microscope could have a sensitivity of up to $4.7 \cdot 10^{-3}$ degrees.

7 Crystal orientation

The following chapter explores preliminary data on the impact of crystal orientation on the RAS signal. The chapter begins with a review on the measurement of single crystals surfaces, with a particular focus on Cu (110) and the various factors that can affect the signal, including surface roughness and surface reconstruction. Experimental data obtained from re-solidified single crystals of copper on ambient air measured with standard RAS is presented, as well as spatially resolved data obtained from large grains measured with the SRAM setup. Additionally, a copper thin film with micron sized grains is deposited on a flexible substrate so that the influence of strain in breaking the crystal symmetry can be investigated.

7.1 RAS on Copper . 71
7.2 Influence of crystal orientation on RAS 76
7.2.1 Single crystal measurements . . 76
7.2.2 Out of plane rotation 78
7.2.3 In-plane rotation 81
7.3 Grain mapping with SRAM . . . 84
7.3.1 Unstrained copper plate 84
7.3.2 Strained thin films 86

7.1 RAS on Copper

The RAS signal generated by anisotropic crystal structures arises from transitions with energies close to the high symmetry points of the electronic band structure, and is dependent on the material and crystal orientation. This property makes RAS a valuable tool for studying the optoelectronic properties of such materials. Research studies have employed RAS to investigate magnetite (110) [148], silicon (100) [149], germanium (113) [150], and gallium arsenide (100) [151], among others. In the case of metals, RAS has been primarily used to study (110) surfaces, as the (100) and (111) surfaces are isotropic for fcc crystal structures, *e.g.* copper [152], gold [153], aluminum [154], silver [155, 156], and nickel [157] among others.

However, the RAS signal is significantly affected by the surface, either because the bulk crystal is isotropic and the anisotropy originates only from surface reconstruction, or because the penetration depth of the probing light is shallow, and the surface layers contribute significantly to the signal. This surface sensitivity of RAS has made it an excellent tool for monitoring thin film growth. Therefore, RAS research is often focused on the study of specific surface reconstructions in different environments and/or temperatures. Figure 7.1 illustrates the RAS signal for the clean Cu (110) surface and for different oxygen adsorption-induced reconstructions, with relevant features marked with lines. The clean surface presents features at 2.1 eV, 4.1 eV, 4.3 eV, and 5.0 eV (signal with green arrows in Figure 7.1a). The 4.3 eV and 5.0 eV features are associated with surface-modified bulk transitions close to the L symmetry point, while the 4.1 eV feature originates from surface states transitions close to the $\overline{X}$ symmetry point [152, 158, 159].

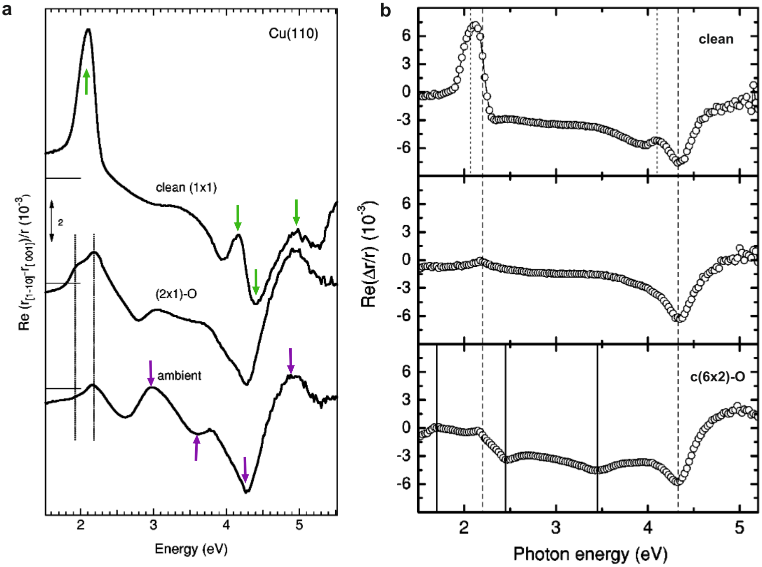

Figure 7.1: Influence of oxide reconstruction on the RAS signal of Cu (110) surfaces. **a** Recorded signal of a Cu(110) crystal in ultra high vacuum for a clean surface and a (2x1)O reconstruction (top and middle), and for the same surface but exposed to ambient air (bottom). Features commented in the text are signaled with green and pruple arrows. **b** Recorded signal of a Cu(110) crystal in ultra high vacuum for a clean surface (top) and a c(6x2)O surface reconstruction. The acquired spectrum in the middle is an in-between state where the oxygen has reacted with the surface but no reconstruction has been formed yet. An annealing step allows for the surface to reconstruct into the c(6x2)O surface. **a** Reprinted from the [160] and **b** reprinted from [158] with permission from the American Physical Society.

The resonance at 2.1 eV is of particular interest because it falls within the spectral range of the SRAM setup. This feature results from multiple contributions, including a transition between surface states at the high symmetry point $\overline{Y}$ and a surface-modified bulk interband transition close to the $\overline{X}$ symmetry point [152, 158, 161]. Drude-like intraband transitions also add a small contribution to the signal around 2.1 eV [162] and anisotropic field effects could also contribute to the surface feature [163, 164], although these calculations appear to be a better fit for oxidized surfaces.

Surface reconstruction due to oxygen adsorption quenches the signal around 2.1 eV, even changing its lineshape and blue shifting the resonance peak. This is evident from the spectra recorded of the (2x1)O (Figure 7.1a middle) and c(6x2)O (Figure 7.1b bottom) surface reconstructions. The transition associated with surface states (2.1 eV) is quenched, as the surface has been modified, while the transition at 2.2 eV still gives rise to an RAS signal as its origin is a bulk interband transition [158]. Additionally, the new surface induces new low energy resonances at 1.7 eV and 2.5 eV for the c(6x2)O reconstruction and at 1.9 eV for the (2x1)O reconstruction.

The oxygen surface coverage of the c(6x2)O and (2x1)O reconstructions is still 1/3 and 1/2 respectively and cannot be considered a fully oxidized surface. As expected, exposing the crystal to ambient air induces further changes in the RAS spectrum. The bulk feature remains (2.2 eV) but the 1.7 eV, 1.9 eV and 2.1 eV resonances of the reconstructed and clean surfaces are fully quenched. At higher energies the lineshape changes compared to the different reconstruction and clean surfaces but the resonances are not quenched (signaled with purple arrows in Figure 7.1a). The valley at 3.5 eV is close to the valley of the c(6x2)O reconstruction and the features at 4.3 eV and 5 eV are found in all surfaces, most probably due to their association with the bulk transitions close to the $\overline{X}$ high symmetry point. A new peak appears around 3 eV but its origin is not yet clear.

As the surface states play a large role in the resulting RAS signal, it is natural to assume that surface roughness/topography also greatly influences the acquired signal. This can be observed in Figure 7.2 showing the RAS signal for different treatments of the copper (110) surface [88, 165]. The spectra in **a** and **b** (corresponding STM images in **c** and **d**) are taken in UHV on a non-oxidized surface prepared with sequential steps of ion bombardment and annealing and a final step of ion bombardment at different temperatures (300 K and 45 K). As can be seen, at 45 K the surface is isotropically full of defects and atom mobility is not high enough for the surface to restructure, resulting in a quenching of the surface states induced signal. At higher temperatures mobility is high enough for surface restructuring and the signal is no quenched and signal can be recovered with further annealing steps. The feature at 4.3 eV is strain sensitive [166] and as a result it is not quenched as the ion bombardment results in an anisotropic strain field.

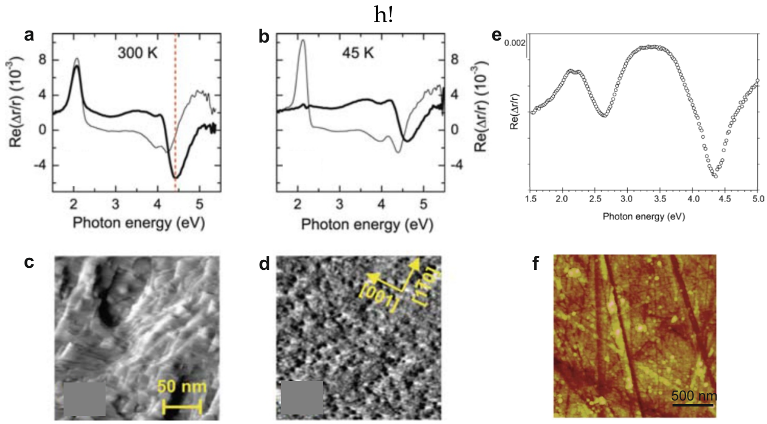

Figure 7.2: Influence of roughness on the RAS signal of Cu (110) surfaces.**a-d** RAS spectra and STM maps taken of a clean Cu (110) surface in UHV after ion bombardment at 300 K (**a,c**) and at 45 K (**b,d**) displaying the effect of surface defects on quenching the RAS signal at 2.1 eV. **e** RAS spectrum of a Cu (110) surface mechanically polished and exposed in ambient air (AFM scan in **f**) showing how surface modified bulk transitions can still show even when significant roughness and an oxide layer is present. **a-d** Reprinted from [165], open access. **e-f** Reprinted from [88] with permission from Elsevier.

Figure 7.2e instead shows the signal acquired from a copper (110) crystal that has been mechanically polished (AFM scan shown in **f**), resulting in a considerably rougher surface. Nonetheless, the spectra shows features at 2.2 and 4.3, the as discussed energies for the surface modified bulk interband transitions. The oxide, which is determined to be cuprous oxide (Cu_2O) by XPS, does not seem to quench the signal as one would expect. The authors do not provide further analysis on the origin of the signals in the presence of an oxide phase. The signal could stem from either the copper - copper oxide interface, as long as the thickness of the oxide layer is not significantly larger than the penetration depth, or from the oxide itself as the bandgap of Cu_2O is in the energy range 1.8-2.5 eV [167]. Given that the peaks are found at 2.2 eV and 4.3 eV, the most likely case is that the origin is still the surface modified bulk transitions. This is possibly supported by the spectrum recorded in Figure 7.1b (middle) of an oxygenated surface that has not yet induced an ordered reconstructed surface yet still shows the features at 2.2 eV and 4.3 eV. Furthermore, there is a broad feature around 3.2-3.5 eV (and valley at 2.6 eV) that has yet an unclear origin.

However, when considering roughened surfaces one also has to take into account the induced facets that might be exposed to the optical probe. For example, Figure 7.3 shows the RAS spectra taken of a copper (111)

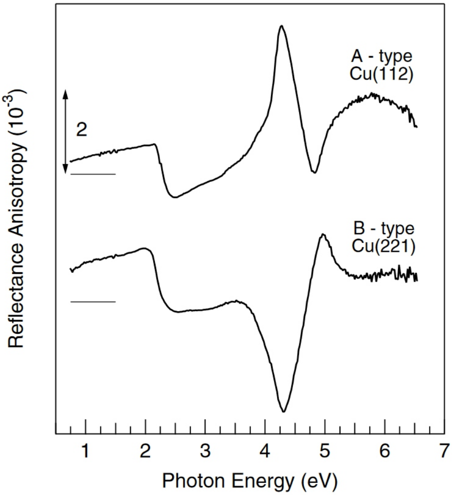

Figure 7.3: RAS spectra of a Cu (111) surface in UHV presenting a stepped surface resulting in (112) and (221) facets. Reprinted from [168] with permission from the American Physical Society.

surface (which is isotropic) that has been prepared to present steps with facets oriented in the (112) or (221) directions. In this case, the 4.3 eV and 5 eV features are still present, with a change in sign depending on the facet, but the feature at 2.2 eV is not present anymore. Instead, a feature around 2 eV appears, which is confirmed to be of a different origin than the surface modified bulk transitions at 2.2 eV [168]. Further measurements also revealed the presence of the 4.3 eV feature in the (443) and (332) directions. Nonetheless, these step facets are all oriented in the same direction, due to sample preparation, while mechanical polishing should induce isotropic roughness, so it is not clear if such facets have an influence in the recorded signal in Figure 7.2.

Due to the high surface sensitivity, RAS has been employed to study the adsorption of various elements/molecules on copper (110), *e.g.* water [169], CO [170, 171] or methanol [172] among others, even with a precoverage of oxygen. Therefore, the environment or contaminants could also influence the RAS signal, although that might be less likely with a full oxide layer on the surface.

In summary, the RAS signal of Cu (110), and presumably as well for other non-isotropic surfaces, is heavily influenced by the surface. This is more pronounced for transitions between surface states that can be completely quenched, *e.g.* the 2.1 eV transition close to the $\overline{Y}$ high symmetry point, than for surface modified bulk transitions, *e.g.* the transitions at 2.2 ev and 4.3 eV. The presence of oxygen, other molecules and/or roughness also influences the signal and tends to quench the features.

7.2 Influence of crystal orientation on RAS

In order to determine if RAS would be a suitable technique for crystal orientation mapping it is necessary to first investigate the influence of non (110) surfaces to the RAS signal. While the (100) and (111) surfaces are isotropic and should yield no signal, it is possible that in-between orientations do give rise to a signal and, if the lineshape is distinct, then crystal orientation indexing should be possible. This section provides an initial exploration into the influence of crystal orientation on the reflectance anisotropy.

7.2.1 Single crystal measurements

Figure 7.4 shows the acquired RAS signal of a single crystal copper sample in ambient air that has been mechanically polished. For more information on the sample preparation procedure the reader is referred to Chapter 3. The crystal exhibits an out of plane orientation that is slightly rotated from the (111) plane (see the EBSD map in Figure 7.4a) with a root mean square roughness of 1.98 nm, although significant anisotropic defects are present due to the last polishing step with 20 nm silica particles (Figure 7.4b).

As the crystal is larger than the probing spot of the RAS setup (~ 2 mm) several spectra at different points of the crystal are recorded an plotted in Figure 7.4c. Features around 2.1 eV, 2.2 eV, 3.5 eV and 4.3 eV are found depending on the considered spectrum (purple arrows). It is possible to argue that a peak exists at 5 eV, however, due to the high level of noise in the deep UV region, it is not possible to draw a definitive conclusion. The peak at 2.2 eV and valley at 4.3 eV coincide with the surface modified bulk transitions discussed in section 7.1, found in both ambient air and for clean surfaces. However, these transitions were discussed for the (110) orientation and, as such, are not necessarily the origin of the features in Figure 7.4c.

Nonetheless, the appearance of these features on a differently prepared surface with a different out of plane orientation is interesting. As is mentioned in reference [166] and in section 7.1, the surface modified bulk transition at 4.3 eV ($E_F \rightarrow L_1^u$) is particularly sensitive to strain. The residual stresses produced

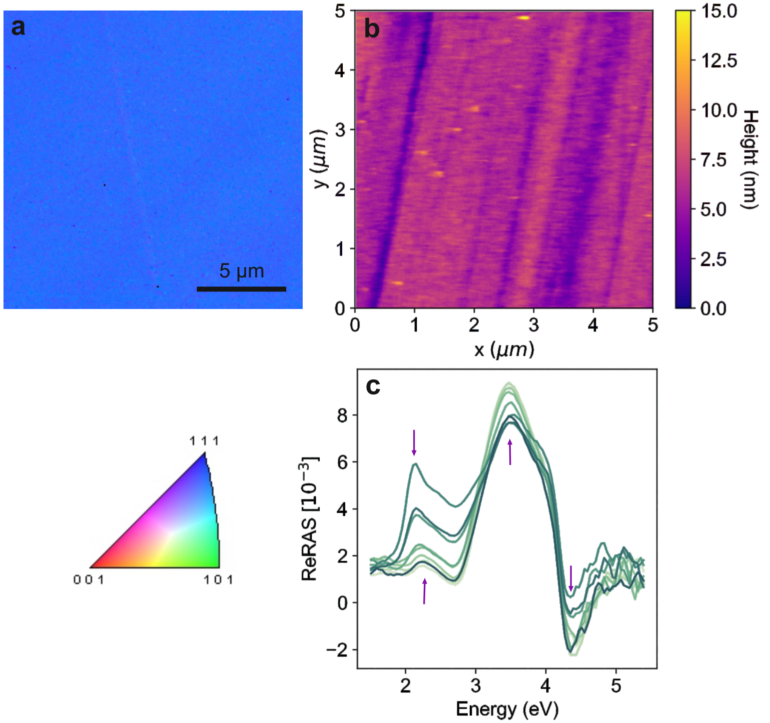

Figure 7.4: RAS signal of a mechanically polished copper single crystal close to the (111) crystal orientation in ambient air. **a** EBSD map of a section of the crystal (color legend at the bottom). **b** AFM scan of a section of the crystal surface with a 1.98 nm RMS roughness. The vertical scratches are attributed to the polishing with silica and diamond particles. **c** RAS spectra of different spots on the crystal surface. Relevant features are signaled with purple arrows.

by the polishing procedure, even if they are minimized by introducing an etching step, should follow the scratches left by the silica particles and should be anisotropic. Therefore, the polishing induced stress field could be the origin of the feature at 4.3 eV.

The feature at 2.2 eV shifts to 2.1 eV for three of the spectra, which is surprising as the feature at 2.1 eV was established to have a pure surface origin. It is hypothesized that the shift could be due to misorientation in the sample as it was directionally crystallized. This hypothesis could explain the slight differences between spectra. Looking at Figure 7.2e, the feature at 2.2 eV is double peaked. If the hypothesis about the misorientation is correct, it could be that the two peaks at 2.1 and 2.2 have a similar origin to the peak in Figure

7.2e, and the change in orientation changes the amplitude ratio between both peaks.

Finally, there is a broad feature centered at 3.5 eV that resembles the same feature found in Figure 7.2e but with an extra shoulder close to 4 eV. This shoulder could have a strain origin, similar to the valley at 4.3 eV, as it coincides with the second strain peak in reference [17]. In reference [17] the authors use *ab initio* calculations of a copper (111) crystal without a surface contribution and, as such, could explain why the strain features are not quenched in the presence of an oxide. The broad peak at 3.5 has only been observed in mechanically polished surfaces (although the c(6x2)O surface reconstruction does show a peak close to 3.5 eV), so it is possible that it could be attributed to anisotropic polishing induced defects.

7.2.2 Out of plane rotation

In order to test the influence of a small change in the out of plane crystal orientation, *i.e.* a rotation around an axis perpendicular to the surface normal vector, a mechanically polished single crystal (same procedure as the sample measured in Figure 7.4) is cut at sequentially increasing angles and the RAS signal of the resulting surface is measured.

Figure 7.5 shows the acquired RAS signal of the single crystal sample at different cutting angles. **a,b** show the EBSD pole and inverse pole figures of the sample cut at 0 degrees (**c**). As one can see, the crystal presents a small in-grain misorientation as the crystal orientation slightly rotates along the sample, probably due to the crystallization direction during sample preparation. This goes along the hypothesis formulated in the previous subsection stating that the small variations in RAS spectra taken of the same surface are due to the in-grain rotation. As seen in the plots in Figure 7.5c-e, this sample also shows small variations between spectra.

The crystal exhibits an out of plane orientation that is close to the (110) orientation. The RAS spectra display peaks at 2.4 eV, 3.2 eV and 4.2 eV and valleys at 2.1 eV, 2.9 eV and 3.6 eV (see arrows in Figure 7.5d). The features at 2.1 eV and 4.2 eV resemble the previously found (110) features at 2.2 eV and 4.3 eV but with an opposite sign, which would just be an indication of the orientation of the crystallographic axis with respect to the measurement axis, and a slight red shift in energy. The feature at 2.1 eV could have several origins, including:

- A surface state transition at the vicinity of the $\overline{Y}$ symmetry point, as the orientation is close to (110). However, this transition has been

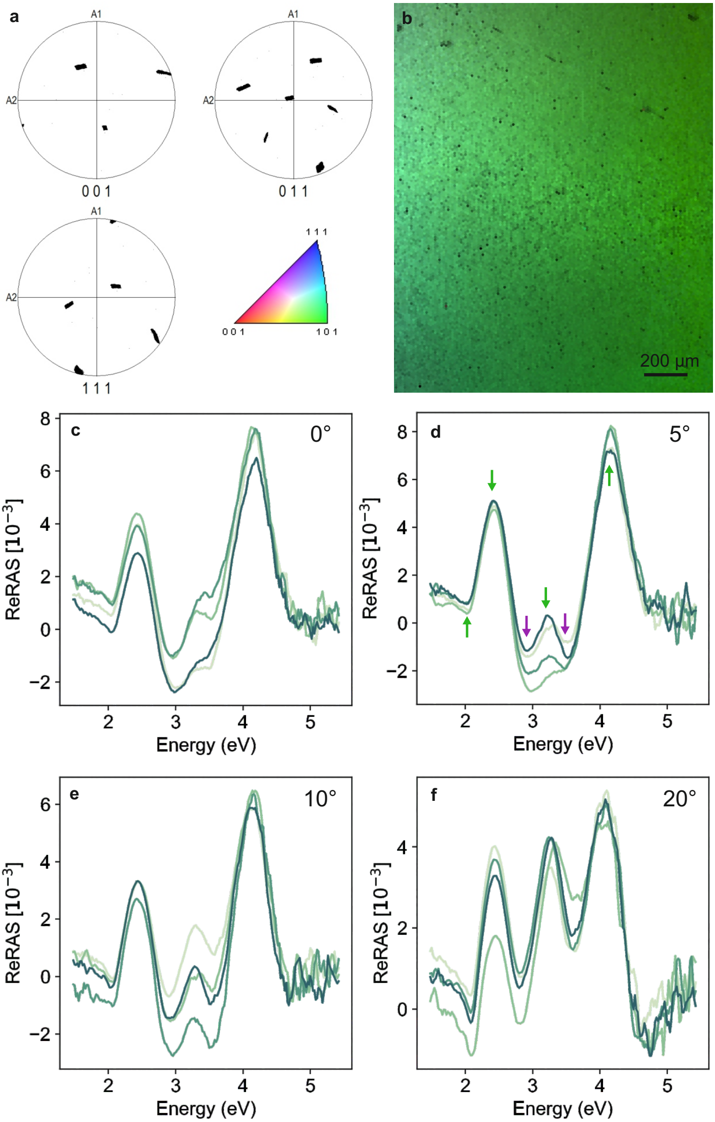

Figure 7.5: EBSD and RAS data of a copper crystal close to (110) orientation. **a-b** Pole and inverse pole figures of the sample's surface. **c-f** RAS spectra of the sample as a function of cutting angle, resulting in surfaces rotated 5°, 10° and 20° degrees.

demonstrated to be quenched in presence of an oxide reconstruction [158].

- Drude intraband transitions of the (110) surface [162], although these should yield a signal shifted towards 2.2 eV.
- Anisotropic local field effects [163, 164]. These match the resonance energy and also resemble the shape, similar to the exposed surface in Figure 7.1a.
- Aligned terraces or steps that expose different facets to the probing light, similar to Figure 7.3, which shows a similar lineshape [168]. However, as there was no annealing step after cutting and polishing, these would have to have formed during polishing before the surface could be oxidized, which seems highly improbable.
- Mechanical polishing induced defects. These would have to be related to the underlying crystal orientation (instead of having a plasmonic origin) in order to explain a resonance coincidentally located at 2.1 eV.
- Surface modified bulk transitions particular to the sample's crystal orientation or the transition close to the $\overline{X}$ symmetry point of the (110) surface that is slightly red shifted due to the small rotation of the crystal.

Based on the measured spectra, it is difficult to establish a clear origin of the 2.1 eV feature (or even 2.2 eV feature for other orientations). It is possible that the absorption edge of copper at 2.1 eV [173] has a high density of states, which can give rise to this feature, and as such, it may be a common feature in all anisotropic orientations. Furthermore, the feature at 4.2 eV is also very close in energy to previously found features at 4.1 eV (although of opposite sign when compared to the 2.1 eV feature) and 4.3 eV, coinciding with another influence point in the absorption of copper. Due to the concentration of transitions/effects at these energies further experiments and calculations would be necessary to identify the origin of these features for each particular orientation.

The peak (or valley with an orthogonal axis alignment) at 2.4 eV is not close to any peak in the clean (110) copper. It coincides with a small feature in the Cu(110)-c(6x2)O surface reconstruction but this feature is not found in the (2x1)O reconstruction and, nonetheless, should be expected to change when the surface is has full oxide cover. The 3.2 eV peak has not been previously recorded for other orientations.

Overall, even if the crystal orientation is relatively close to (110), the measured features in the spectra of Figure 7.5 cannot be assigned an origin as there are too many variables influencing the surface signal that change with each out of plane orientation. Nonetheless, one could look at it phenomenologically to try to extract information from the spectra. For example, the valleys at 2.9 eV and 3.6 eV, marked with purple arrows in Figure 7.5d, shift in energy depending on the cutting angle. However, the energy shift changes in both direction and magnitude depending on the cutting angle as well as between spectra taken at the same cutting angle. This would suggest that the valleys are just formed because of the energy fixed adjacent peaks, hence totally dependent on the amplitude and positions of these peaks, and don't have their origin in an electronic band transition.

Furthermore, while the peaks at 2.4 eV and 4.2 eV have a more or less constant ratio, the peak at 3.2 eV changes amplitude as a function of cutting angle. The amplitude increases for increasing rotation of the crystal, even though it does so non-linearly with a sharp increase at 20 degrees. The feature at 2.1 eV also has a narrower bandwidth at 20 degrees. The 3.2 eV feature is so far unique and seems to be highly dependent on the out of plane rotation and, as such, could potentially be employed to index crystal orientation. This is further supported by all the different surfaces measured in Figure 7.4 and Figure 7.5 being distinct. Nonetheless, more orientations would need to be measured to conclude that crystal orientation indexing is possible with RAS.

7.2.3 In-plane rotation

To index crystal orientation it is also necessary to measure the in-plane rotation of a grain. This can be achieved by employing azimuth dependent reflectance anisotropy spectroscopy (ADRAS), which acquires RAS measurements as a function of the azimuth angle (introduced in section 6.3), and has been demonstrated as a tool to determine the crystallographic axis of the sample, *e.g.* of molecularly oriented PET films [24] or even 2D materials using a microscopy setup [77].

Figure 7.6a-b show the EBSD data of a grain in a polycrystalline copper sample. Unlike the samples discussed in previous sections, this sample was deformed by cold rolling to induce defects and then annealed to achieve recrystallization, resulting in a polycrystalline sample with grain size in the order of millimetres. As one can see, the EBSD pole and inverse pole figure for the sample indicate significant in-grain misorientation, with an average orientation between 110 and 111.

Figure 7.6c shows the ADRAS of the sample, obtained by rotating the sample from 0° to 90°. The RAS spectra show very broad features with a peak between 2.1 eV and 2.2 eV (depending on angle, 2.15 eV at 0°), another peak at 4.3 eV, and shoulders at 2.7 eV and 3.6 eV. However, due to the broad nature

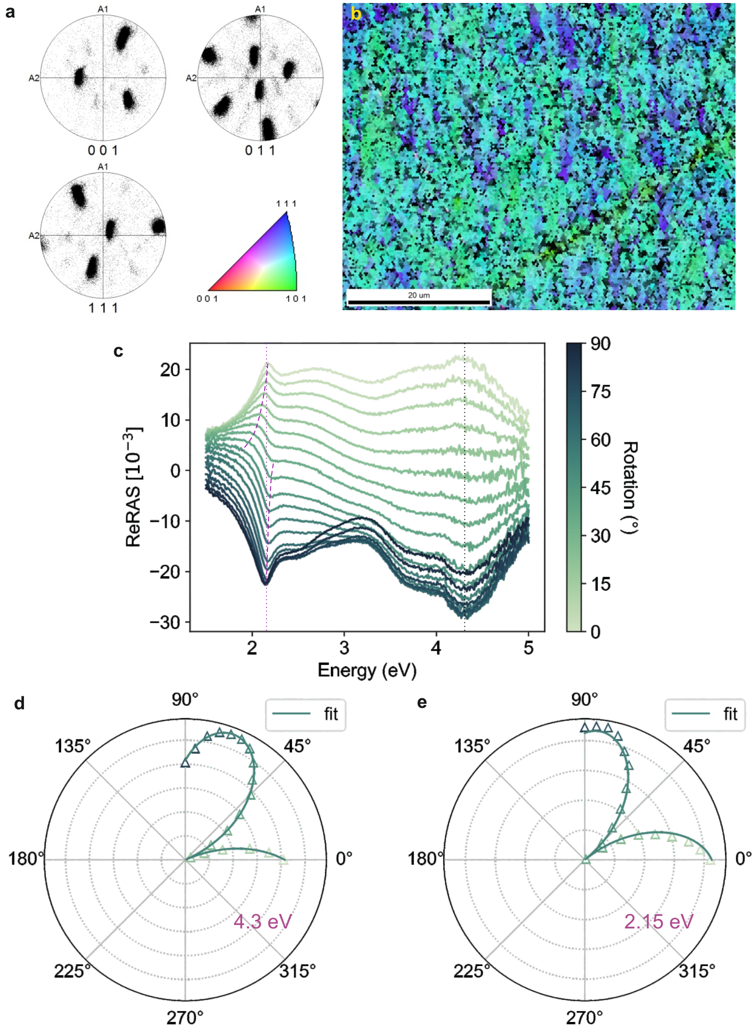

Figure 7.6: EBSD and RAS data of a copper grain in-between (110) and (111) out of plane orientation. **a-b** Pole and inverse pole figures of the sample's surface showcasing significant in-grain misorientation. **c** azimuth dependent RAS spectra of the sample as a function of in-plane rotating angle. **d-e** Angular dependence of $|\Re\Delta r/r|$ of the features located at 4.3 eV and 2.15 eV and their fit of equation 7.1.

of the spectra, it is difficult to distinguish features in the range between the 2.15 eV and 4.3 eV peaks.

Upon in-plane rotation of the sample, the peak at 2.15 eV shifts energy while the peak at 4.3 eV stays constant in energy. This could be attributed to the misorientation in the grain, as different orientations in the grain may present a slightly shifted 2.15 eV peak. An in-plane rotation could change the selectivity between the different orientations, resulting in an overall shift of the peak. It has been shown that the spectra of differently oriented films/surfaces in ADRAS changes shape as a function of rotation angle [174].

Figure 7.6d shows the azimuth angular dependence of the 4.3 eV feature's absolute value fitted with equation 7.1. Unlike the antenna case in section 6.3, the resonance follows the expected $\cos(2\phi)$ trend typical for $2mm$ systems [19]. The fit for the angular dependence of the 2.15 eV feature, while not perfect, is relatively good. The small discrepancy can be attributed to the in-grain misorientation as the resulting signal is a grain average. However, the optical eigenaxes for each feature do not coincide with $\theta_0^{2.15} - \theta_0^{4.3} \simeq 15.4°$. This could be because of two different reasons, either the misorientation in the grain that shifts the axes or the dependence on wavelength of θ_0. As the transitions that give rise to an RAS signal depend on the polarization of the exciting light, each transition would yield different eigenaxes resulting in a wavelength dependence of θ_0 [19]. Given the ~15° different between each feature's axis, it is more probable that the shift originates because of the wavelength dependence, as such a big misorientation would result in significant stresses.

$$\Re\left\{\frac{\Delta r}{r}\right\} \sim \cos\left[2\left(\phi - \theta_0\right)\right] \tag{7.1}$$

In summary, the observed RAS spectra for the samples discussed in section 7.2 show several features that could be attributed to surface states, surface modified bulk states, surface reconstruction or roughness. However, due to the samples presenting crystal orientations that have not been previously studied and the surface/interface resulting from the sample preparation procedure it is difficult to assign any particular feature to a specific electronic transition or structural property. Nonetheless, given the dependence of the features with both in-plane and out of plane rotations, the possibility of crystal orientation indexing cannot be ruled out. More orientations need to be measured in order to properly determine the extent to which RAS can be used for crystal orientation determination.

7.3 Grain mapping with SRAM

7.3.1 Unstrained copper plate

The most efficient way of measuring a wide variety of orientations is to employ an RAS microscope with polycrystalline samples. Unfortunately, currently the SRAM setup spectral range is limited in the 1.77 eV to 2.55 eV range, severely limiting the selection of features the setup is sensitive to. Nonetheless, and one of the main reason why copper is employed for this study, the surface features around 2.1 eV fall perfectly with the range of the setup.

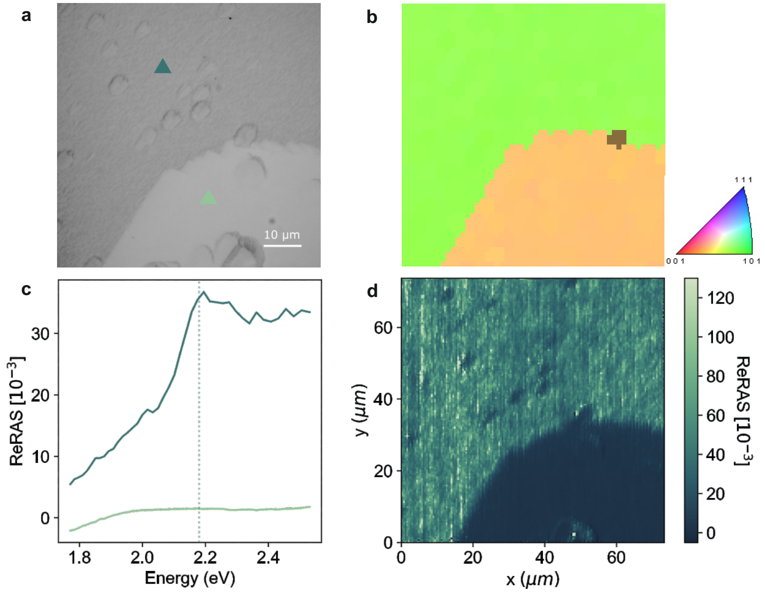

Figure 7.7: EBSD map and SRAM signal and map at a grain boundary of a copper plate polished both mechanically and by board ion beam. **a** Optical microscopy picture of the grain boundary taken with a 100x objective. **b,d** EBSD map and SRAM map at the location pictured in **a**. **c** SRAM signal taken at the spots indicated with coloured triangles in **a**

In order to obtain polycrystalline samples, copper plates are annealed to induce grain growth, mechanically polished and subsequently polished with board ion beam, see Chapter 3 for more details on sample preparation. The plates present a polycrystalline texture without a preferential orientation with grain sizes ranging from tens of micrometres to millimetres. Figure 7.7

displays the SRAM signal taken at a boundary in a copper plate sample. The EBSD map (Figure 7.7b) shows that the grains have orientations in the vicinity of the (110) and (100) orientations (green and orange respectively). Figure 7.7c plots the SRAM spectra taken at a sample spot on each grain, as indicated with the coloured triangles in Figure 7.7a). As one can observe, the (110) grain exhibits a feature close to 2.2 eV, in line with the spectra presented in the previous sections, usually attributed to surface modified bulk transitions. In contrast, the (100) grain shows a flat spectrum, indicating an isotropic surface as expected from such an orientation.

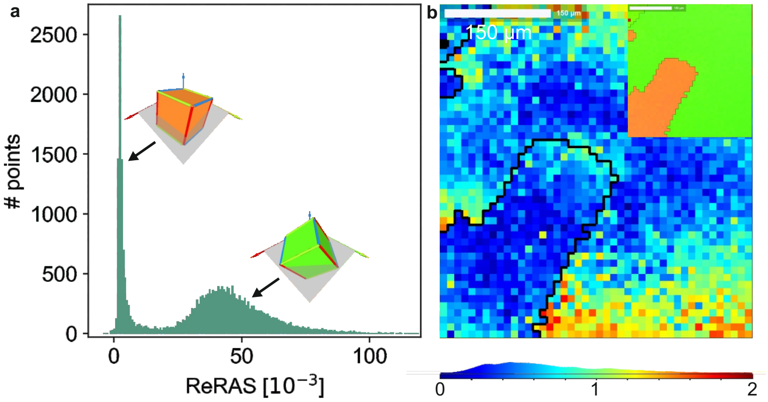

Figure 7.8: **a** Histogram of the SRAM map taken in Figure 7.7d with a unit cell indicating the crystal orientation of each grain. **b** Grain distortion of the two grains forming the grain boundary mapped in Figure 7.7.

Acquiring a map at the resonance peak (2.2 eV) clearly differentiates between the two grains (Figure 7.7d), also seen in the histogram plot of all the SRAM points in the map (Figure 7.8a), which exhibits a clear bi-modal distribution. However, the signal broadening of the (110) grain is significantly larger than that of the (100) grain. There are two factors that can contribute to the broadening; roughness and in-grain distortion. From inspection of the surface with SEM the roughness should yield the same broadening for both grains. The distortion map (Figure 7.8b) also reveals a similar distortion for both grains, with a distortion distribution of up to 1° for both grains at the mapping spot. This means that the sensitivity to a crystal rotation for the (100) orientation is low compared to the (110) rotation, which would indicate a nonlinear relation between SRAM signal and crystal orientation, at least when rotating between (100) and (110). Taking the SRAM spectra of grains that are not in the vicinity of the (110) crystal orientation yielded no significant resonance, which limits the current capabilities of the setup for grain mapping.

7.3.2 Strained thin films

One approach to address the issue of isotropic surfaces failing to generate a SRAM signal is to break the underlying symmetry by externally applying strain. To this purpose, copper is electrodeposited on a polyimide film (with an interlayer of 500 nm sputtered silver to act as the cathode), with a targeted thickness of 20 μm. Annealing at 300 °C induces grain growth, achieving a grain size in the 1 μm to 10 μm range. After annealing the film also exhibits an anisotropic strain distribution due to the mismatch in thermal expansion coefficients between substrate and film.

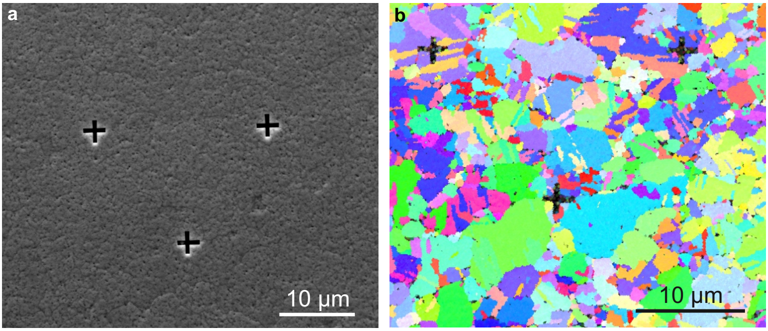

Figure 7.9: SEM (**a**) and EBSD (**b**) scans of an electroplated copper film on a flexible substrate. Crosses have been milled with FIB on the film to act as markers for correlating the EBSD and SRAM maps.

Figure 7.9 shows the SEM micrograph and an EBSD map of the surface of an electroplated film, where three markers are milled with FIB. The film exhibits a textured and rough surface that is characterized by a concentration of pits and grooves, which are presumably cause by grooving at the grain boundaries. The EBSD map shows a texture with an heterogeneous grain orientation distribution across the measured area, allowing to test the selectivity of the SRAM setup to varying grain orientations.

Figure 7.10 displays the SRAM maps of the region imaged in Figure 7.9 for the sample in a prestrained state (mounted on the mechanical stage, **a,c,e**) and a strained state (**b,d,f**). While the acquired SRAM map shows a non random distribution, as can be seen by the features from the prestrained map being reproduced by the strained map, it is difficult to assign any particular origin to the spatial features. Overlapping the grain boundary map (obtained from the EBSD measurement) with the SRAM maps seems to indicate that most of the SRAM signal peaks are distributed along grain boundaries or small grains. This would suggest that either the grooving or the symmetry breaking at the grain boundary are the origin of the SRAM signal.

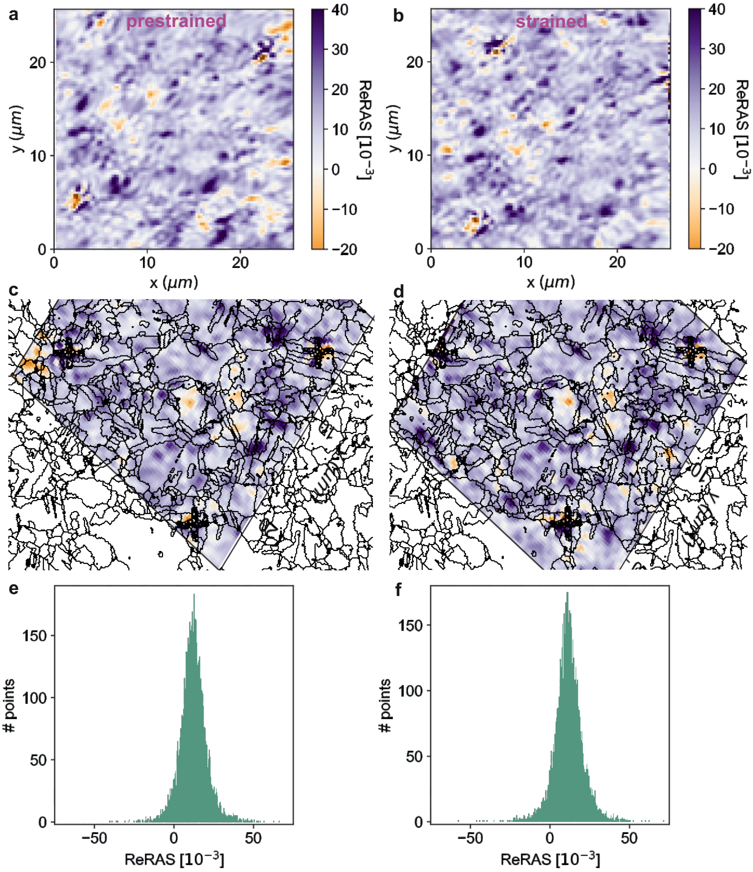

Figure 7.10: SRAM signal of the region imaged in Figure 7.9 taken at 2.1 eV. Left column shows the prestrained results and right column shows the strain results. **a,b** as measured SRAM maps, **c,d** SRAM maps overlaped with the grain boundary structure, **e-f** histograms of the signal in **a,b**.

However, due to mechanical artefacts during scanning, which result in a distorted map, and the large amount of grains in the sample, a conclusion cannot be reached on the exact origin of each SRAM map feature. On the one hand, the signal shows single mode distribution (as seen in Figure

7.10e-f) without any shift due to strain, most probably due to the strain sensitive feature being located at higher energies, presumably indicating that surface roughness is the main cause of local anisotropy. On the other hand, localization of features in the SRAM map, which does not exhibit a spatially uniform distribution, would indicate that anisotropy is texture originated. Therefore, while the SRAM setup shows promise for grain mapping, further experiments are needed to establish its suitability.

General discussion

8

8.1 Main findings . . . 89
8.2 On-going issues . . 94
8.3 Outlook 96
8.4 Conclusions 98

This chapter discusses the main findings and contributions of the thesis, as well as unresolved issues and potential directions for future research. First, the major findings are summarized and their implications discussed. Next, the limitations and unresolved issues are highlighted and possible ways to address them are suggested. Finally, potential applications or studies where the SRAM setup could contribute to further advances in the field are discussed.

8.1 Main findings

A diffraction limited RAS microscopy setup with a broad spectral range (compared to current laser-based setups) has been implemented. While the sensitivity of the setup decreases with increasing numerical aperture, it is not found that the numerical aperture limits the capabilities of the setup, indicating that even higher numerical apertures are possible (see Figure 8.1 for the relationship between sensitivity and NA). The setup presents a noise floor in the order of 10^{-4} rad in average, depending on wavelength and numerical aperture, and, in ideal conditions, the phase sensitivity of the setup could reach $4.7 \cdot 10^{-3}$ degrees.

The broad spectral range of the setup allows for tuning of the scanning energy, adapting the setup for multiple materials or applications. Sensitivity to features in gold, crystalline and amorphous germanium, and copper are demonstrated. Moreover work on alpha-brass has also shown a feature in the spectral range of the setup (as long as zinc content is high enough to red-shift the resonance) [20]. This includes both metals and semiconductors as well as crystalline and non-crystalline materials.

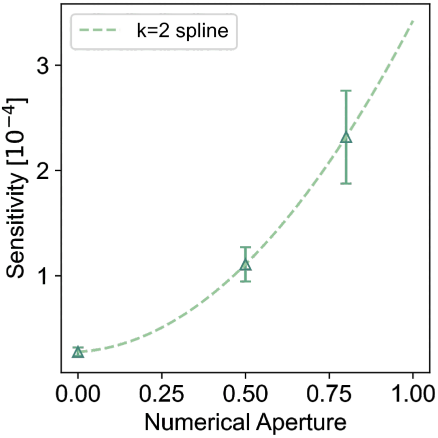

Figure 8.1: Strain sensitivity as a function of numerical aperture. Mean and standard deviation values are taken by averaging over wavelength from the data in Figure 4.6. Assuming $\Im\{\delta r/r\} = 0.01$ for 1% strain, then the sensitivity of the technique is equal to the strain sensitivity. A quadratic spline interpolation shows the non-linearity relationship between sensitivity and numerical aperture.

Strain sensitivity is demonstrated in gold and germanium, with a measured average elasto-optic constant of gold $\overline{P} = 0.18 - 0.30i$. High strain sensitivity is also demonstrated for slot nanoantennas with a measured sensitivity of $\kappa = -20.9 \pm 1.53$ meV/%, which implies that the setup is sensitive to shifts of less than 1 nm in a 100 nm antenna. The measured nanoresonators can be a model of dipolar transitions in materials and, as such, open the way to study materials resonances via mimicking the symmetry breaking with carefully designed antennas, *e.g.* using chiral antennas to simulate chiral materials resonances. Furthermore, mapping of complex strain distributions is achieved in good agreement with FEM simulations and/or a standard strain mapping technique in Raman spectroscopy. To the best of the author's knowledge, SRAM is currently the only optical technique able to map strain in metals without strain markers.

It is also found, as expected, that texture has an influence on the RAS signal, even for mechanically polished surfaces in ambient air. While results in measuring the influence of crystal orientation on copper are preliminary, the measurements indicate the possibility of indexing grains in future works. Grain mapping is achieved for polished samples and close to (110) crystal orientation. Mapping on rougher samples indicated a signal concentration presumably induced at the grain boundaries.

Comparison with other non-destructive techniques

In the opinion of the author, this thesis has resulted in an advancement in the field of RAS microscopy and non-destructive strain sensing with RAS. It is, however, important to place the capabilities of the SRAM setup in context to the more general field of non-destructive strain sensing. In particular, the techniques considered are Raman spectroscopy, X-ray diffraction (XRD) and electron microscopy (TEM/SEM). As strain sensitivity usually depends on material and experimental conditions, the numbers given in the following list are meant as a general range estimation to contextualize SRAM and, therefore, can deviate depending on the situation. The reader is encouraged to do a more in depth review if a more specific scenario is of interest.

- *Raman Spectroscopy*: Both Raman spectroscopy and SRAM are optical techniques and, as such, share the same limitation for spatial resolution, which is usually in the hundreds of manometers range. In terms of strain sensitivity, Raman usually (for single monochromator setups) has a similar sensitivity to electron back-scattered diffraction (EBSD), in the order of 10^{-3} to 10^{-4} [175], which is lower than the achievable 10^{-5} sensitivity for RAS. According to the data presented in Chapter 4, the sensitivity for SRAM is, in average, an order of magnitude lower in the order of 10^{-4} and would therefore be similar to that of Raman. However, roughness does have a higher impact for SRAM than it has for Raman, so SRAM could perform worse for rougher samples. In general though, SRAM and Raman present comparable resolution and sensitivity.
  As mentioned in Chapter 5, the main difference between the two techniques lies in the materials range and measured strain state. Raman spectroscopy measures a convolution of the different strain components and, thus, analysis can be challenging without assistance of FEM simulations. To that end, it is believed that both techniques are not in competition and instead the combined use of SRAM ($\propto \epsilon_{xx} - \epsilon_{yy}$) and Raman ($\propto \epsilon_{xx} + \epsilon_{yy}$) would allow to decouple ϵ_{xx} and ϵ_{yy} without the assistance of FEM simulations (for plane stress). Lastly, Raman spectroscopy is, in general, not sensitive to metals, due to their lack of change in polarizability, so SRAM could provide an avenue to measure more material classes.
- *X-ray diffraction*: XRD provides information about the crystal lattice of the sample through the Laue/Bragg diffraction of x-rays, including strain and crystal orientation [176]. When comparing SRAM to XRD one has to differentiate between synchrotron XRD (sXRD) and lab-scale XRD. sXRD offers spatial resolution in the order of 100 nm [176, 177],

and even down to 10 nm when employing coherent imaging [178], with a 10^{-4} to 10^{-5} strain sensitivity [179]. In contrast, lab-scale XRD is generally limited by the brightness and extension of the source and cannot achieve the resolution of sXRD, with conventional setups offering a probing spot in the order of hundreds of micrometers or millimiters without mapping capabilities, and also lower sensitivity. However, the use of coherent bragg imaging [180] with soft x-rays has allowed for sub-100 nm resolution [181] and recent advances in hard x-ray sources are bringing down the resolution in conventional setups to the micrometer regime [182]. These techniques require complex and extensive algorithms (for coherent imaging) and/or sources not yet conventionally available in standard XRD setups but the trend is certainly for lab-scale setups to increase their spatial resolution.
In general, SRAM cannot compete with XRD, as both sXRD and advanced lab-scale setups (when considering cutting edge technology) offer far superior resolution with a similar sensitivity to SRAM and are not limited by materials class, as long as the sample is crystalline. However, SRAM does offer a few advantages over XRD that could make it an attractive technique for mechanical characterization. The main advantage of SRAM is its simplicity and cheaper components, while sXRD and non-conventional XRD setups require extensive time and/or economic investment. On the technical side, even though there are studies on XRD of amorphous materials [183], the results in this thesis indicate that SRAM could become an alternative technique to XRD for amorphous materials. Furthermore, when measuring the yield strength of ultra-thin films, RAS has proved itself to complement XRD due to its smaller probing volume, offering higher signal to noise ratio for a 50 nm thick film [25]. While SRAM is noisier than standard RAS setups, it could become an alternative as well when studying ultra-thin films with thicknesses below 50 nm. This has been the object of further studies in the dissertation of Calvo [64].

- *Scanning electron microscopy*: SEM offers the capability to map crystal orientation, defect density and strain via EBSD. Even though the probing spot of an SEM can achieve a spatial resolution below 10 nm, the needed interaction volume to form Kikuchi patterns limits the spatial resolution to tens of nanometers [184] (this limit can be circumvented with transmission EBSD [185]). The strain resolution of EBSD can reach 10^{-4} for cutting edge setups [186, 187]. Due to induced in-grain misorientation, plasticity can severely hinder sensitivity with 10^{-3} uncertainties [188], needing digital image correlations techniques, often termed high resolution EBSD, to achieve 10^{-4} in plastically

deformed metals [189]. Most commercial SEMs with EBSD capabilities currently available in laboratories offer strain sensitivities limited to 10^{-3} or even 10^{-2}. Moreover, strain measurements in EBSD are most often relative to a calibration pattern in the sample, as simulation based patterns often introduce phantom stresses [190].
EBSD does once again offer superior spatial resolution to SRAM with similar sensitivity for setups at the frontier of research. In the case of metals, SRAM does provide higher sensitivity than conventional EBSD setups, with recent advances in high resolution EBSD necessary to match its strain sensitivity. SRAM might provide an advantage for polycrystalline samples with a grain size in the low tens of nanometers, where the sampling spot of the electron beam might overlap multiple Kikuchi patterns. In terms of sample preparation, both EBSD and SRAM require flat surfaces, as the sensitivity in SRAM is severely limited by roughness. Nonetheless, the probing volume of the electron beam makes measuring ultra-thin films challenging once again, further encouraging SRAM/RAS as a technique for mechanical characterization of ultra-thin films. Last but not least, EBSD requires conductive samples and high vacuum to not hinder sensitivity. So far the materials studied with SRAM have been semiconductors or metals but the technique is not limited in material classes and future works could be center on polymeric/non-conductive samples or *in situ* environmental studies.

- *Transmission electron microscopy*: TEM is, perhaps, a bit out of place in this comparison and it is included for completion. TEM can achieve extremely high resolutions, even lower than 1 nm, can image dislocations and, depending on the measurement mode, presents strain sensitivity in the order of 10^{-3} to 10^{-4} for the most advanced instruments [191, 192]. It is, therefore, clearly very far superior to SRAM in terms of resolution with a similar strain sensitivity. Nonetheless, TEM requires challenging sample preparation, which can influence the strain distribution, thicknesses equal or lower than 100 nm and *in situ* experiments also present further complications. Furthermore, the field of view can be a limiting factor, which can be challenging for micromechanics studies. Therefore, as the measurement conditions are so different, SRAM and TEM are not in competition and instead could be used complementarily, *e.g.* employing TEM to study the texture of a polycrystalline ultra-thin film [64].

8.2 On-going issues

Roughness

Roughness induced noise is arguably the biggest limitation of the SRAM setup (and RAS microscopy in general). It is found that it limits both strain sensitivity and crystal orientation indexing. Roughness has been shown to introduce artefacts, due to focusing, as well as modifying the electronic structure at the surface, which mainly determines the SRAM signal. Going forward, two different ways to minimize the impact of roughness are proposed:

- *Reducing roughness:* This work, as well as previous studies [64, 142], has shown that template stripping is effective in reducing surface roughness. This has been shown with the low measurement noise in the SRAM spectra acquired of the template stripped gold films with milled nanoantennas. For example, template stripping could be used to reduce the roughness in the electrodeposited copper thin films measured in Chapter 7, although the high addition of copper to silicon or silicon nitride wafers has proven a challenge when attempting to template strip copper onto flexible substrates [64]. Gold is also a fcc metal and could be a candidate substitute material for the study as it is significantly easier to strip and, moreover, presents a strain sensitive feature in the spectral range of the microscope. Alternatively, focusing on systems with minimum surface roughness, *e.g.* epitaxially grown semiconductors (as the bridges measured in Chapter 5) or sputtered materials on silicon/silicon nitride wafers, can be a straightforward way to fully show the capabilities of the SRAM setup.
- *Data treatment algorithms:* The Interpretation of RAS spectra can be a challenging task, even more so with the now added capability for spectral maps and the resulting data size increase. However, the data presented in this thesis are predominantly untreated. Some spectra are smoothed with a small window moving average and maps are interpolated to a square matrix for plotting reasons, but no significant algorithm is applied to the data. Instead, learning algorithms [193, 194] or even simpler noise reducing filters, *e.g.* Gaussian or median filters [195], can be a powerful tool for noise reduction and identification of roughness patterns. To that end, there are already efforts to apply learning algorithms to the interpretation of RAS data [196] and, for applications that do not require a fundamental understanding of the RAS signal's origin, these algorithms should be further explored.

Spectral range

While SRAM is a very versatile technique that is not in principle limited by materials class or environment, in practice the spectral range of the setup determines the range of materials the technique is sensitive to. Figure 8.2 shows the spectral range of the supercontinuum laser source with the current range of the setup highlighted in green. As one can see, there is potential to expand the wavelength range towards the near-infrared without modifying the source but expansion into the UV range would require a new source. An acousto-optic modulator spanning the range 650 nm to 1100 nm has actually already been acquired an in the process of implementation (see Figure 4.5b) and the new extended range (shown in purple) will allow to expand the range of materials to, for example, Al [197], GaAs [23], or potentially Si, as its bandgap is exactly 1100 nm.

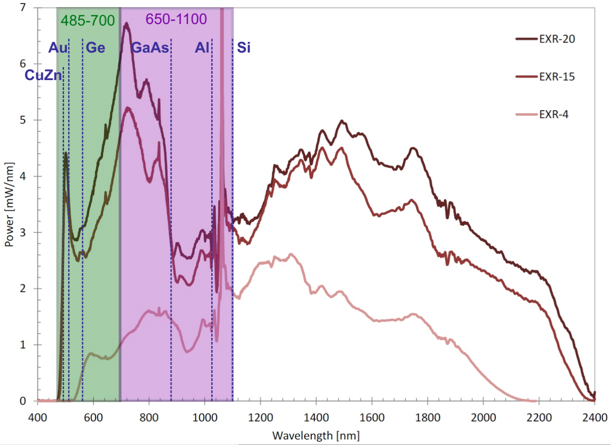

Figure 8.2: Spectral range of the supercontinuum source used in the SRAM setup (EXR-20). Highlighted in green is the current range of the setup limited by the acousto-optic modulator and highlighted in purple is the range of an extended acousto-optic modulator in the infrared range. For reference, strain sensitive resonances of selected materials are signal with discontinued lines. Spectral graph adapted from [198]

Unfortunately, expansion into the UV range has been so far unsuccessful. Two approaches have been explored; use of a crystal to convert the pump supercontinuum light to UV through second harmonic generation (offered commercially) and monochromating and filtering of a mercury lamp for specific wavelengths in the UV range. In both cases the the resulting beam intensity is too low to acquire RAS spectra. However, the low beam intensity of the mercury lamp is caused by the spatial filtering needed to focus with sub-micron resolution (as the lamp is an extended source and is, therefore, limited by Liouville's theorem). There exists a trade-off between intensity and resolution and, as such, for applications with a lax requirement for resolution, it is possible to acquire RAS signals at approximately 20 μm resolution (at the emission lines of the mercury lamp). Lastly, another option would be to change the laser source to newer models, *e.g.* the FIU-6 system (NKT Photonics, Denmark), that offer an extended range (up to 380 nm) at the cost of a reduced intensity.

Acquisition speed

In order for SRAM to become an attractive technique for *in situ* studies it would be enticing to improve the acquisition speed of the setup. Currently, the single point acquisition time, including stage movement and wavelength change, is approximately 3.5 s for maps and 2.6 s for spectra. Considering an integration time of 1 s and a time constant $\tau_c = 0.05$ s with a stabilisation time of $5\tau_c$, the theoretical limit would be 1.25 s per point, meaning the speed can be improved, at maximum, by a 2.1 to 2.8 factor without reducing signal to noise ratio. Further increases in speed would require a reduction in either τ_c or integration time, resulting in an increased signal to noise ratio. Instead, a multi-channel setup could be implemented utilizing multiple PMTs, inspired by reference [199]. As the acousto-optic modulator allows for up to 8 simultaneous wavelengths, this could improve the spectral acquisition speed by up to 8 times, allowing spectral maps to be taken *in situ*. However, realistically, as dichroic mirrors and bandpass filters would be needed for the new setup, most probably only a double channel or triple channel could be implemented. Otherwise, a monochromator-PMT scheme, similar to reference [199], would allow for the 8 channels to be implemented. While the use of a monochromator a priori makes the acousto-optic modulator redundant, illuminating with the non-monochromated beam would increase the power density to levels that could damage the sample, such that use of the acousto-optic modulator would be recommended.

8.3 Outlook

The previous sections in this chapter have discussed possible avenues for improvement of the setup and data analysis. This section instead aims to provide a quick suggestion on possible research directions given the capabilities of the SRAM setup discussed in previous chapters.

Micro electronic mechanical systems

Micro electro-mechanical systems (MEMS) refer to a class of miniaturized devices that integrate electrical and mechanical components on a single chip. MEMS devices typically have critical dimensions in the micrometer range and can be tailored to a wide range of functions, including but not limited to sensing and actuation. MEMS technology has emerged as a key enabler for a variety of applications, *e.g.* biomedical sensors [200], optical switches [201] or accelerometers [202]. The characteristics of MEMS devices, such as low power consumption, high sensitivity, and fast response time, make them attractive for a wide range of scientific and industrial applications.

MEMS devices are typically fabricated using semiconductor processing techniques, such as lithography, and, therefore, usually exhibit smooth surfaces with minimal roughness. Furthermore, MEMS devices can comprise multiple materials, including polymers, metals and semiconductors, which, coupled to their smooth surfaces, make them ideal candidates for characterization with the SRAM setup. While there a multitude of mechanisms that induce failure in MEMS, mechanical failure is very predominant in MEMS systems due to their interaction with the environment and often times movables parts [203, 204], see Figure 8.3 for some examples of failure in MEMS. This makes understanding the mechanical properties and performance of the devices, as well as the underlying materials, of the utmost importance. Characterization of stress distributions is often difficult, as has been discussed in length during this thesis, thus FEM simulations are often used to analyze the mechanical performance of MEMS and aid in their design. Therefore, SRAM could provide invaluable input in the failure analysis and design optimization of MEMS.

Plastic deformation

As seen in Chapter 5, plasticity has an influence on the SRAM/RAS signal of strained metals. While mapping distributions of elastic strain is important, specially for brittle materials, in ductile materials failure most often happens at heavily deformed areas. Therefore, understanding the influence of plastic deformation on the RAS signal is a challenge that needs to be tackled in order to realise full mechanical characterization in future applications.

While there have been some efforts into understanding the correlation between RAS and plastic deformation [113], this is an area of research that has been mostly unexplored. In Figure 5.9 one can see how, even if the overall ratio between SRAM signal and strain is linear, elastic and plastic

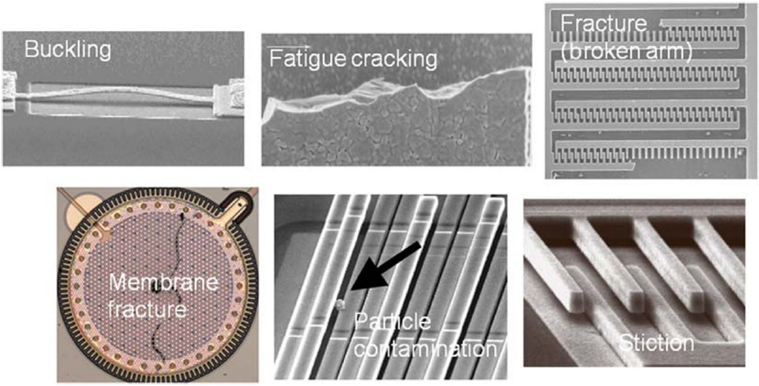

Figure 8.3: Examples of failure in micro electro-mechanical system devices, most prominently mechanical failure. Reprinted from [204] with permission from Elsevier.

deformation have a separate influence on the RAS signal, as expected from the distinct physical nature of each phenomena. As such, this implies that the elasto-optic tensor has a dependency on strain. Expanding equation 2.4 into higher orders yields

$$D = d\sigma + \varepsilon E + c\sigma E + f\sigma^2 E + \dots \quad , \tag{8.1}$$

where second and higher order terms not linear with E have been ignored. f determines the third order effect that describes the influence of strain on the photoelastic effect as $(\partial D/\partial E)_\sigma = \varepsilon + c\sigma + f\sigma^2$. Since in the elastic regime the photoelastic effect is linear, this means that f is mostly influenced by plastic deformation and determining f could potentially help in the understanding of the relationship between RAS and plastic deformation. Moreover, as the coefficients a, b, c, d etc. are influenced by the crystal structure of the material, gaining insight into f could translate to other fields like piezoelectricity (d) or the electro-optic effect (a), although piezoelectric materials are most often brittle. Therefore, going forward it is suggested that the plastic regime is further explored in order to fully understand the elasto-optic effect.

8.4 Conclusions

In conclusion, non-destructive mechanical characterization has become essential for an improved understanding and design of complex multi-material devices, such as flexible electronics that comprise demanding mechanical deformation conditions. The scanning reflectance anisotropy microscope (SRAM) presented in this thesis provides a versatile stand-alone platform for high-resolution strain mapping and strain imaging of semiconductors, metasurfaces and metals. Figure 8.4 is, perhaps, the most important figure in this thesis as it places SRAM in the field of non-destructive strain mapping. While there are certainly issues that need to be addressed, this thesis has proved SRAM to be an alternative to traditional strain mapping techniques that offers its own advantages in the right conditions with still plenty room for development and improvement of its capabilities.

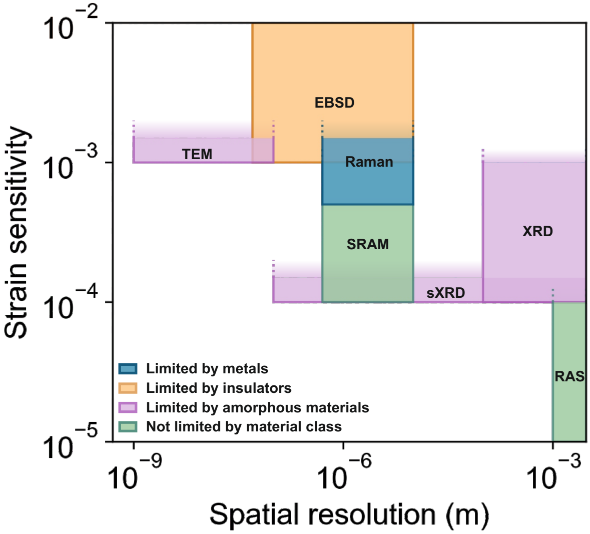

Figure 8.4: Relationship between spatial resolution and strain sensitivity for the most important non-destructive strain mapping techniques in the field with the addition of SRAM described by the results in this thesis. The edges of all boxes are open ended in their low sensitivity limit as all techniques are sensitive to strains larger than 10^{-2}. The limits for each technique are estimated values for conventional setups. See section 8.1 for more information on the cutting edge technologies for each technique not represented in this chart.

APPENDIX

A

RAS signal derivation

In this Appendix the mathematical derivation of the RAS signal recorded by the detector is presented. The derivation follows Weightman's formulation [19, 36] using Jone's formalism for polarization dependent optical elements. The instrument is assumed to be in the configuration showed in Figure 2.1a.

Considering the $\hat{\boldsymbol{x}}$ and $\hat{\boldsymbol{y}}$ axes oriented along the axes of the sample, the electric field amplitude at the detector plane is

$$\boldsymbol{E} \propto \begin{pmatrix} 1 & 0 \\ 0 & 0 \end{pmatrix} \begin{pmatrix} \cos(\Gamma/2) & i\sin(\Gamma/2) \\ i\sin(\Gamma/2) & \cos(\Gamma/2) \end{pmatrix} \begin{pmatrix} r_x & 0 \\ 0 & r_y \end{pmatrix} \begin{pmatrix} 1 \\ 1 \end{pmatrix}, \tag{A.1}$$

where each matrix represents - from left to right - the analyzer, PEM, sample and incoming polarized light after going through the polarizer. Γ is the modulation of the PEM of the form $\Gamma = \Gamma_0 \sin(\omega t)$, with Γ_0 being the modulation amplitude, and r_x and r_y are the complex Fresnel reflection coefficients of the sample along the $\hat{\boldsymbol{x}}$ and $\hat{\boldsymbol{y}}$ axes. Performing the matrices multiplication yields an electric field of the form

$$\boldsymbol{E} \propto \begin{pmatrix} \cos(\Gamma/2) r_x + i\sin(\Gamma/2) r_y \\ 0 \end{pmatrix}. \tag{A.2}$$

By using Euler's formula the expression can be written as

$$\boldsymbol{E} \propto \frac{1}{2}\left[e^{i\Gamma/2}\left(r_x + r_y\right) + e^{-i\Gamma/2}\left(r_x - r_y\right)\right]\hat{\boldsymbol{x}}. \tag{A.3}$$

Calculating the intensity ($I \propto \|\boldsymbol{E}\|^2 = \boldsymbol{E}\cdot\boldsymbol{E}^*$) detected by the PMT yields the following four terms

$$\frac{1}{4}\left[r'_x + r'_y + i(r''_x + r''_y)\right]\left[r'_x + r'_y - i(r''_x + r''_y)\right] \tag{A.4}$$

$$\frac{1}{4}e^{i\Gamma}\left[r'_x + r'_y + i(r''_x + r''_y)\right]\left[[r'_x - r'_y - i(r''_x - r''_y)\right] \tag{A.5}$$

$$\frac{1}{4}e^{-i\Gamma}\left[r'_x - r'_y + i(r''_x - r''_y)\right]\left[[r'_x + r'_y - i(r''_x + r''_y)\right] \tag{A.6}$$

$$\frac{1}{4}\left[r'_x - r'_y + i(r''_x - r''_y)\right]\left[[r'_x - r'_y - i(r''_x - r''_y)\right] \tag{A.7}$$

where r'_i and r''_i denote the real and imaginary parts of the Fresnel coefficients. Adding A.4 and A.7 results in the total reflectance

$$R = \frac{1}{2}\left(\|r_x\|^2 + \|r_y\|^2\right), \tag{A.8}$$

while adding A.5 and A.6 results in two additional terms such that

$$I \propto R + \frac{1}{2}\cos(\Gamma)\left(\|r_x\|^2 - \|r_y\|^2\right) + \sin(\Gamma)\left(r'_x r''_y - r'_y r''_x\right). \tag{A.9}$$

It is now clear that the intensity has a dc component ($I_{dc} \propto R$) and two ac components oscillating at a frequency multiple of the PEM modulation frequency ω. These oscillating terms can be related to the RAS signal $\Delta r/r$

$$\frac{\Delta r}{r} = \frac{r'_x - r'_y + i(r''_x - r''_y)}{r_x + r_y + i(r''_x + r''_y)} = \frac{\|r_x\|^2 - \|r_y\|^2}{\|r_x\|^2 + \|r_y\|^2} + i\frac{2(r'_y r''_x - r'_x r''_y)}{\|r_x\|^2 + \|r_y\|^2} \tag{A.10}$$

by comparing equation A.10 to A.9. It's trivial to see that I/I_{dc} yields

$$\frac{I}{I_{dc}} = 1 + \cos(\Gamma)\mathrm{Re}\left[\frac{\Delta r}{r}\right] + \sin(\Gamma)\mathrm{Im}\left[\frac{\Delta r}{r}\right]. \tag{A.11}$$

The term $\cos(\Gamma) = \cos\left(\Gamma_0 \sin\left(\omega t\right)\right)$ can be simplified using the following expansion in Bessel functions

$$\cos\left[\Gamma_0 \sin(\omega t)\right] = J_0(\Gamma_0) + 2\sum_{m=1}^{\infty} J_{2m}(\Gamma_0)\cos(2m\omega t) \tag{A.12}$$

$$\sin\left[\Gamma_0 \sin(\omega t)\right] = 2\sum_{m=0}^{\infty} J_{2m+1}(\Gamma_0)\sin\left[(2m+1)\omega t\right], \tag{A.13}$$

where J_n is the nth-order Bessel function. Adjusting the PEM retardation to 2.405 radians such that $J_0(\Gamma_0) = 0$ and taking up to the first non-zero order in the Bessel expansions yields the final expression

$$\frac{I}{I_{dc}} = 1 + 2J_1(\Gamma_0)\mathrm{Im}\left[\frac{\Delta r}{r}\right]\sin(\omega t) + 2J_2(\Gamma_0)\mathrm{Re}\left[\frac{\Delta r}{r}\right]\cos(2\omega t). \tag{A.14}$$

Hence

$$\Re\{\Delta r/r\} = \frac{I_{2\omega}}{2J_2 I_{dc}} \tag{A.15}$$

$$\Im\{\Delta r/r\} = \frac{I_{\omega}}{2J_1 I_{dc}} \tag{A.16}$$

References

1. Bardeen, J. & Shockley, W. Deformation Potentials and Mobilities in Non-Polar Crystals. *Physical Review* **80,** 72–80. (2023) (Oct. 1, 1950).
2. Hensel, J. C. & Feher, G. Cyclotron Resonance Experiments in Uniaxially Stressed Silicon: Valence Band Inverse Mass Parameters and Deformation Potentials. *Physical Review* **129,** 1041–1062. (2023) (Feb. 1, 1963).
3. Maiti, C. K. *Stress and Strain Engineering at Nanoscale in Semiconductor Devices* 275 pp. ISBN: 978-1-00-040493-7. Google Books: `jpktEAAAQBAJ` (CRC Press, June 29, 2021).
4. Tyurnina, A. V. *et al.* Strained Bubbles in van Der Waals Heterostructures as Local Emitters of Photoluminescence with Adjustable Wavelength. *ACS Photonics* **6,** 516–524. ISSN: 2330-4022, 2330-4022. (2023) (Feb. 20, 2019).
5. Süess, M. J. *et al.* Analysis of Enhanced Light Emission from Highly Strained Germanium Microbridges. *Nature Photonics* **7,** 466–472. ISSN: 1749-4893. (2023) (6 June 2013).
6. Katiyar, A. K., Thai, K. Y., Yun, W. S., Lee, J. & Ahn, J.-H. Breaking the Absorption Limit of Si toward SWIR Wavelength Range via Strain Engineering. *Science Advances* **6,** eabb0576. (2023) (July 29, 2020).
7. Miao, Y., Zhao, Y., Zhang, S., Shi, R. & Zhang, T. Strain Engineering: A Boosting Strategy for Photocatalysis. *Advanced Materials* **34,** 2200868. ISSN: 1521-4095. (2023) (2022).
8. Xia, Z. & Guo, S. Strain Engineering of Metal-Based Nanomaterials for Energy Electrocatalysis. *Chemical Society Reviews* **48,** 3265–3278. (2023) (2019).
9. Chu, M., Sun, Y., Aghoram, U. & Thompson, S. E. Strain: A Solution for Higher Carrier Mobility in Nanoscale MOSFETs. *Annual Review of Materials Research* **39,** 203–229. (2023) (2009).
10. Hu, X. *et al.* Enhanced Ferromagnetism and Tunable Magnetism in Fe3GeTe2 Monolayer by Strain Engineering. *ACS Applied Materials & Interfaces* **12,** 26367–26373. ISSN: 1944-8244. (2023) (June 10, 2020).
11. Schlom, D. G. *et al.* Elastic Strain Engineering of Ferroic Oxides. *MRS Bulletin* **39,** 118–130. ISSN: 0883-7694, 1938-1425. (2023) (Feb. 2014).

12. Xu, L., Shyu, T. C. & Kotov, N. A. Origami and Kirigami Nanocomposites. *ACS Nano* **11,** 7587–7599. ISSN: 1936-0851, 1936-086X. (2023) (Aug. 22, 2017).

13. Kim, D.-H. *et al.* Epidermal Electronics. *Science* **333,** 838–843. (2023) (Aug. 12, 2011).

14. Ho, C.-M. & Tai, Y.-C. Micro-Electro-Mechanical-Systems (Mems) and Fluid Flows. *Annual Review of Fluid Mechanics* **30,** 579–612. (2023) (1998).

15. Wang, S., Oh, J. Y., Xu, J., Tran, H. & Bao, Z. Skin-Inspired Electronics: An Emerging Paradigm. *Accounts of Chemical Research* **51,** 1033–1045. ISSN: 0001-4842. (2023) (May 15, 2018).

16. GRAYSON, A. *et al.* A BioMEMS Review: MEMS Technology for Physiologically Integrated Devices. *Proceedings of the IEEE* **92,** 6–21. ISSN: 1558-2256 (Jan. 2004).

17. Volpi, M. *et al.* Sensing Strain-Induced Symmetry Breaking by Reflectance Anisotropy Spectroscopy. *Applied Physics Letters* **119,** 151602. ISSN: 0003-6951. (2023) (Oct. 11, 2021).

18. Aspnes, D. E. Above-Bandgap Optical Anisotropies in Cubic Semiconductors: A Visible–near Ultraviolet Probe of Surfaces. *Journal of Vacuum Science & Technology B: Microelectronics and Nanometer Structures* **3,** 1498. ISSN: 0734211X. (2023) (Sept. 1985).

19. Weightman, P., Martin, D. S., Cole, R. J. & Farrell, T. Reflection Anisotropy Spectroscopy. *Reports on Progress in Physics* **68,** 1251–1341. ISSN: 0034-4885, 1361-6633. (2023) (June 1, 2005).

20. Wyss, A. *et al.* Reflectance Anisotropy Spectroscopy as a Tool for Mechanical Characterization of Metallic Thin Films. *Journal of Physics D: Applied Physics* **48,** 415303. ISSN: 0022-3727. (2023) (Sept. 2015).

21. Cole, R. J. *et al.* Stress-Induced Optical Anisotropy in Polycrystalline Copper Studied by Reflection Anisotropy Spectroscopy. *Journal of Physics D: Applied Physics* **36,** L115. ISSN: 0022-3727. (2023) (Oct. 2003).

22. Papadimitriou, D. & Richter, W. Highly Sensitive Strain Detection in Silicon by Reflectance Anisotropy Spectroscopy. *Physical Review B* **72,** 075212. ISSN: 1098-0121, 1550-235X. (2023) (Aug. 29, 2005).

23. Ortega-Gallegos, J., Lastras-Martínez, A., Lastras-Martínez, L. F. & Balderas-Navarro, R. E. Optical Anisotropy Induced by Mechanical Strain around the Fundamental Gap of GaAs. *physica status solidi c* **5,** 2561–2564. ISSN: 1610-1642. (2023) (2008).

24. Schmidegg, K., Sun, L. D. & Zeppenfeld, P. Optical and Mechanical Anisotropies of Oriented Poly(Ethylene Terephthalate) Films. *Applied Physics Letters* **89,** 051906. ISSN: 0003-6951. (2023) (July 31, 2006).
25. Wyss, A., Sologubenko, A. S., Mishra, N., Gruber, P. A. & Spolenak, R. Monitoring of Stress–Strain Evolution in Thin Films by Reflection Anisotropy Spectroscopy and Synchrotron X-ray Diffraction. *Journal of Materials Science* **52,** 6741–6753. ISSN: 1573-4803. (2023) (June 1, 2017).
26. Koopmans, B., Santos, P. & Cardona, M. Microscopic Reflection Difference Spectroscopy on Semiconductor Nanostructures. *physica status solidi (a)* **170,** 307–315. ISSN: 1521-396X. (2023) (1998).
27. Shen, W., Hu, C., Li, S. & Hu, X. Using High Numerical Aperture Objective Lens in Micro-Reflectance Difference Spectrometer. *Applied Surface Science. 7th_International Conference on Spectroscopic Ellipsometry* **421,** 535–541. ISSN: 0169-4332. (2023) (Nov. 1, 2017).
28. Yang, S. *et al.* Highly In-Plane Optical and Electrical Anisotropy of 2D Germanium Arsenide. *Advanced Functional Materials* **28,** 1707379. ISSN: 1616-3028. (2023) (2018).
29. Huang, W. *et al.* Reflectance Difference Spectroscopy Microscope for Circular Defects on InN Films. *Optics Express* **24,** 15059. ISSN: 1094-4087. (2023) (June 27, 2016).
30. Zhang, W., Qin, Z. & Yang, Z. Reflectance Difference Spectroscopy Microscope for Nanometer Step Height Detection. *Journal of Applied Physics* **97,** 074314. ISSN: 0021-8979, 1089-7550. (2023) (Apr. 2005).
31. Lastras-Martínez, L. F., Castro-García, R., Balderas-Navarro, R. E. & Lastras-Martínez, A. Microreflectance Difference Spectrometer Based on a Charge Coupled Device Camera: Surface Distribution of Polishing-Related Linear Defect Density in GaAs (001). *Applied Optics* **48,** 5713. ISSN: 0003-6935, 1539-4522. (2023) (Oct. 20, 2009).
32. Lastras-Martínez, L. F. *et al.* Micro Reflectance Difference Techniques: Optical Probes for Surface Exploration. *physica status solidi (b)* **249,** 1119–1123. ISSN: 1521-3951. (2023) (2012).
33. Sendra, J., Haake, F., Calvo, M., Galinski, H. & Spolenak, R. *Scanning Reflectance Anisotropy Microscopy for Multi-Material Strain Mapping* arXiv: `2302.04095 [cond-mat, physics:physics]`. `http://arxiv.org/abs/2302.04095` (2023). preprint.
34. Aspnes, D. E. & Studna, A. A. Anisotropies in the Above—Band-Gap Optical Spectra of Cubic Semiconductors. *Physical Review Letters* **54,** 1956–1959. (2023) (Apr. 29, 1985).

35. Aspnes, D. E., Harbison, J. P., Studna, A. A. & Florez, L. T. Application of Reflectance Difference Spectroscopy to Molecular-beam Epitaxy Growth of GaAs and AlAs. *Journal of Vacuum Science & Technology A* **6,** 1327–1332. ISSN: 0734-2101. (2023) (May 1, 1988).

36. Martin, D. S. & Weightman, P. Reflection Anisotropy Spectroscopy: A New Probe of Metal Surfaces. *Surface and Interface Analysis* **31,** 915–926. ISSN: 1096-9918. (2023) (2001).

37. Acher, O. & Drévillon, B. A Reflectance Anisotropy Spectrometer for Real-time Measurements. *Review of Scientific Instruments* **63,** 5332–5339. ISSN: 0034-6748, 1089-7623. (2023) (Nov. 1992).

38. Aspnes, D. E. Observation and Analysis of Epitaxial Growth with Reflectance-Difference Spectroscopy. *Materials Science and Engineering: B* **30,** 109–119. ISSN: 0921-5107. (2023) (Mar. 1, 1995).

39. Aspnes, D. E., Harbison, J. P., Studna, A. A. & Florez, L. T. Reflectance-difference Spectroscopy System for Real-time Measurements of Crystal Growth. *Applied Physics Letters* **52,** 957–959. ISSN: 0003-6951. (2023) (Mar. 21, 1988).

40. Briones, F. & Horikoshi, Y. Application of Reflectance Difference Spectroscopy (RDS) to Migration-Enhanced Epitaxy (MEE) Growth of GaAs. *Japanese Journal of Applied Physics* **29,** 1014. ISSN: 1347-4065. (2023) (6R June 1, 1990).

41. Hohage, M., Sun, L. & Zeppenfeld, P. Reflectance Difference Spectroscopy – a Powerful Tool to Study Adsorption and Growth. *Applied Physics A* **80,** 1005–1010. ISSN: 1432-0630. (2023) (Feb. 1, 2005).

42. Cole, R. J., Frederick, B. G. & Weightman, P. Substrate Dependence of Adlayer Optical Response in Reflectance Anisotropy Spectroscopy. *Journal of Vacuum Science & Technology A: Vacuum, Surfaces, and Films* **16,** 3088–3095. ISSN: 0734-2101, 1520-8559. (2023) (Sept. 1998).

43. Macdonald, B. F., Law, J. S. & Cole, R. J. Azimuth-Dependent Reflection Anisotropy Spectroscopy. *Journal of Applied Physics* **93,** 3320–3327. ISSN: 0021-8979, 1089-7550. (2023) (Mar. 15, 2003).

44. Bonanni, A. *et al.* Reflectance Difference Spectroscopy and Magneto-Optical Analysis of Digital Magnetic Heterostructures. *Journal of Vacuum Science & Technology B: Microelectronics and Nanometer Structures Processing, Measurement, and Phenomena* **17,** 1722–1727. ISSN: 1071-1023. (2023) (July 1, 1999).

45. Denk, R., Hohage, M. & Zeppenfeld, P. Extremely Sharp Spin Reorientation Transition in Ultrathin Ni Films Grown on Cu(110)-(2x1)O. *Physical Review B* **79,** 073407. (2023) (Feb. 17, 2009).

46. Denk, R., Hohage, M., Sun, L. & Zeppenfeld, P. Optical and Magnetic Properties of Ni Films Grown on Cu(110)-(2 x 1)O and Cu(110)-(2 x 3)N. *Verhandlungen der Deutschen Physikalischen Gesellschaft* **43.** `https://www.osti.gov/etdeweb/biblio/21197157` (2023) (July 1, 2008).

47. Nye, J. F. *Physical Properties of Crystals: Their Representation by Tensors and Matrices* 356 pp. ISBN: 978-0-19-851165-6 (Clarendon Press, 1985).

48. Smith, E. & Dent, G. *Modern Raman Spectroscopy: A Practical Approach* 253 pp. ISBN: 978-1-119-44055-0. Google Books: `WsqFDwAAQBAJ` (John Wiley & Sons, Apr. 29, 2019).

49. Kudelski, A. Analytical Applications of Raman Spectroscopy. *Talanta* **76,** 1–8. ISSN: 0039-9140. (2023) (June 30, 2008).

50. Schrader, B. *Infrared and Raman Spectroscopy: Methods and Applications* 814 pp. ISBN: 978-3-527-61542-1. Google Books: `9LOcQs2MSesC` (John Wiley & Sons, Sept. 26, 2008).

51. Ni, Z. H. *et al.* Uniaxial Strain on Graphene: Raman Spectroscopy Study and Band-Gap Opening. *ACS Nano* **2,** 2301–2305. ISSN: 1936-0851. (2023) (Nov. 25, 2008).

52. Becker, M., Scheel, H., Christiansen, S. & Strunk, H. P. Grain Orientation, Texture, and Internal Stress Optically Evaluated by Micro-Raman Spectroscopy. *Journal of Applied Physics* **101,** 063531. ISSN: 0021-8979, 1089-7550. (2023) (Mar. 15, 2007).

53. De Wolf, I. Relation between Raman Frequency and Triaxial Stress in Si for Surface and Cross-Sectional Experiments in Microelectronics Components. *Journal of Applied Physics* **118,** 053101. ISSN: 0021-8979, 1089-7550. (2023) (Aug. 7, 2015).

54. Kelly, K. L., Coronado, E., Zhao, L. L. & Schatz, G. C. The Optical Properties of Metal Nanoparticles: The Influence of Size, Shape, and Dielectric Environment. *The Journal of Physical Chemistry B* **107,** 668–677. ISSN: 1520-6106. (2023) (Jan. 1, 2003).

55. Willets, K. A. & Van Duyne, R. P. Localized Surface Plasmon Resonance Spectroscopy and Sensing. *Annual Review of Physical Chemistry* **58,** 267–297. pmid: `17067281`. (2023) (2007).

56. Fuku, K. *et al.* The Synthesis of Size- and Color-Controlled Silver Nanoparticles by Using Microwave Heating and Their Enhanced Catalytic Activity by Localized Surface Plasmon Resonance. *Angewandte Chemie International Edition* **52,** 7446–7450. ISSN: 1521-3773. (2023) (2013).

57. Hutter, E. & Fendler, J. H. Exploitation of Localized Surface Plasmon Resonance. *Advanced Materials* **16,** 1685–1706. ISSN: 1521-4095. (2023) (2004).
58. Kosako, T., Kadoya, Y. & Hofmann, H. F. Directional Control of Light by a Nano-Optical Yagi–Uda Antenna. *Nature Photonics* **4,** 312–315. ISSN: 1749-4893. (2023) (5 May 2010).
59. Novotny, L. & Hecht, B. *Principles of Nano-Optics* 583 pp. ISBN: 978-1-139-56045-0. Google Books: `RHC_AwAAQBAJ` (Cambridge University Press, Sept. 6, 2012).
60. Ghenuche, P., Cherukulappurath, S., Taminiau, T. H., Van Hulst, N. F. & Quidant, R. Spectroscopic Mode Mapping of Resonant Plasmon Nanoantennas. *Physical Review Letters* **101,** 116805. ISSN: 0031-9007, 1079-7114. (2023) (Sept. 9, 2008).
61. Knight, M. W. *et al.* Aluminum Plasmonic Nanoantennas. *Nano Letters* **12,** 6000–6004. ISSN: 1530-6984. (2023) (Nov. 14, 2012).
62. Biagioni, P., Huang, J.-S. & Hecht, B. Nanoantennas for Visible and Infrared Radiation. *Reports on Progress in Physics* **75,** 024402. ISSN: 0034-4885. (2023) (Jan. 2012).
63. Zentgraf, T. *et al.* Babinet's Principle for Optical Frequency Metamaterials and Nanoantennas. *Physical Review B* **76,** 033407. ISSN: 1098-0121, 1550-235X. (2023) (July 10, 2007).
64. Calvo, M. *Reflectance Anisotropy Spectroscopy on Ultrathin Noble Metal Films: Mechanics, Topography and Crystal Orientation* Doctoral Thesis (ETH Zurich, 2022). (2023).
65. Deshmukh, R. *et al.* Synthesis, Spray Deposition, and Hot-Press Transfer of Copper Nanowires for Flexible Transparent Electrodes. *ACS Applied Materials & Interfaces* **10,** 20748–20754. ISSN: 1944-8244, 1944-8252. (2023) (June 20, 2018).
66. Süess, M. J. *Highly Strained Si and Ge Microand Nanobridges for Micro- and Optoelectronic Applications* Doctoral Thesis (ETH Zurich, 2014). (2023).
67. Koopmans, B., Richards, B., Santos, P., Eberl, K. & Cardona, M. In-plane Optical Anisotropy of GaAs/AlAs Multiple Quantum Wells Probed by Microscopic Reflectance Difference Spectroscopy. *Applied Physics Letters* **69,** 782–784. ISSN: 0003-6951, 1077-3118. (2023) (Aug. 5, 1996).

68. Richards, B., Wolf, E. & Gabor, D. Electromagnetic Diffraction in Optical Systems, II. Structure of the Image Field in an Aplanatic System. *Proceedings of the Royal Society of London. Series A. Mathematical and Physical Sciences* **253,** 358–379. (2023) (Jan. 1997).

69. Balderas-Navarro, R. E. *et al.* Optical Anisotropies of Si Grown on Step-Graded SiGe(110) Layers. *Applied Physics Letters* **96,** 091904. ISSN: 0003-6951, 1077-3118. (2023) (Mar. 2010).

70. Lastras-Martínez, L. *et al.* Polarization Contrast Linear Spectroscopies for Cubic Semiconductors under Stress: Macro- and Micro-Reflectance Difference Spectroscopies. *Annalen der Physik* **523,** 121–128. ISSN: 1521-3889. (2023) (2011).

71. Lastras-Martínez, L. F., Castro-García, R., Balderas-Navarro, R. E. & Lastras-Martínez, A. *Reflectance Difference Spectrometer Based on the Use of a CCD Camera* in. Sixth Symposium Optics in Industry (eds Gutiérrez-Vega, J. C., Dávila-Rodríguez, J. & López-Mariscal, C.) (Monterrey, Mexico, Mar. 23, 2007), 64221C. (2023).

72. Lastras-Martínez, L. F. *et al.* Microscopic Optical Anisotropy of Exciton-Polaritons in a GaAs-based Semiconductor Microcavity. *Physical Review B* **96,** 235306. ISSN: 2469-9950, 2469-9969. (2023) (Dec. 18, 2017).

73. Lastras-Martínez, L. F. *et al.* Optical Detection of Graphene Nanoribbons Synthesized on Stepped SiC Surfaces. *Journal of Applied Physics* **122,** 035701. ISSN: 0021-8979, 1089-7550. (2023) (July 21, 2017).

74. Flores-Rangel, G. *et al.* Optical Contrast in the Near-Field Limit for Structural Characterization of Graphene Nanoribbons. *Applied Surface Science* **536,** 147710. ISSN: 01694332. (2023) (Jan. 2021).

75. Hu, C., Huo, S., Shen, W., Li, Y. & Hu, X. Reflectance Difference Microscopy for Nanometre Thickness Microstructure Measurements. *Journal of Microscopy* **270,** 318–325. ISSN: 1365-2818. (2023) (2018).

76. Hu, C., Wang, H., Huo, S., Shen, W. & Hu, X. Rapid Reflectance Difference Microscopy Based on Liquid Crystal Variable Retarder. *Journal of Vacuum Science & Technology B* **37,** 050604. ISSN: 2166-2746. (2023) (Sept. 2019).

77. Shen, W., Sun, Z., Huo, S. & Hu, C. Directly Evaluating the Optical Anisotropy of Few-Layered Black Phosphorus during Ambient Oxidization. *Advanced Optical Materials* **10,** 2102018. ISSN: 2195-1071. (2023) (2022).

78. Shen, W. *et al.* Resolving the Optical Anisotropy of Low-Symmetry 2D Materials. *Nanoscale* **10,** 8329–8337. ISSN: 2040-3364, 2040-3372. (2023) (2018).

79. Yang, S. *et al.* In-Plane Optical Anisotropy and Linear Dichroism in Low-Symmetry Layered TlSe. *ACS Nano* **12,** 8798–8807. ISSN: 1936-0851. (2023) (Aug. 28, 2018).

80. Yang, Y. *et al.* In-Plane Optical Anisotropy of Low-Symmetry 2D GeSe. *Advanced Optical Materials* **7,** 1801311. ISSN: 2195-1071. (2023) (2019).

81. Zhong, M. *et al.* In-Plane Optical and Electrical Anisotropy of 2D Black Arsenic. *ACS Nano* **15,** 1701–1709. ISSN: 1936-0851. (2023) (Jan. 26, 2021).

82. Zheng, X. *et al.* Investigation of InGaN Layer Grown Under In-Rich Condition by Reflectance Difference Spectroscopy Microscope. *Journal of Nanoscience and Nanotechnology* **18,** 7468–7472. ISSN: 1533-4880. (2023) (Nov. 1, 2018).

83. Dudley, J. M., Genty, G. & Coen, S. Supercontinuum Generation in Photonic Crystal Fiber. *Reviews of Modern Physics* **78,** 1135–1184. ISSN: 0034-6861, 1539-0756. (2023) (Oct. 4, 2006).

84. Savitzky, A. & Golay, M. J. E. Smoothing and Differentiation of Data by Simplified Least Squares Procedures. *Analytical Chemistry* **36,** 1627–1639. ISSN: 0003-2700, 1520-6882. (2023) (July 1, 1964).

85. Aspnes, D. E., Harbison, J. P. & Studna, A. A. Application of Reflectance Difference Spectroscopy to Molecular-beam Epitaxy Growth of GaAs and AlAs.

86. Abbe, E. Beiträge zur Theorie des Mikroskops und der mikroskopischen Wahrnehmung. *Archiv für Mikroskopische Anatomie* **9,** 413–468. ISSN: 0176-7364. (2023) (Dec. 1, 1873).

87. Aspnes, D. E. Optical Response of Microscopically Rough Surfaces. *Physical Review B* **41,** 10334–10343. ISSN: 0163-1829, 1095-3795. (2023) (May 15, 1990).

88. Isted, G. E. & Martin, D. S. Preparation and Characterisation of Au(11 0) and Cu(11 0) Surfaces for Applications in Ambient Environments. *Applied Surface Science* **252,** 1883–1890. ISSN: 0169-4332. (2023) (Dec. 15, 2005).

89. Martin, D. S., Cole, R. J. & Weightman, P. Effects of Ion Bombardment on the Optical and Electronic Properties of Cu(110). *Physical Review B* **72,** 035408. ISSN: 1098-0121, 1550-235X. (2023) (July 5, 2005).

90. Martin, D. S., Maunder, A. & Weightman, P. Thermal Behavior of the Cu(110) Surface Studied by Reflection Anisotropy Spectroscopy and Scanning Tunneling Microscopy. *Physical Review B* **63,** 155403. ISSN: 0163-1829, 1095-3795. (2023) (Mar. 23, 2001).

91. Volpi, M. *Reflectance Anisotropy Spectroscopy as a Tool for Characterization of Additively Manufactured Precious Alloys* PhD thesis (ETH Zurich, 2021).

92. Gobeli, G. W. & Kane, E. O. Dependence of the Optical Constants of Silicon on Uniaxial Stress. *Physical Review Letters* **15,** 142–146. ISSN: 0031-9007. (2023) (July 26, 1965).

93. Musilová, J. Piezoreflectance Study of E1 and E2 Transitions in Germanium from 107 to 326 K. *physica status solidi (b)* **101,** 85–93. ISSN: 1521-3951. (2023) (1980).

94. Sell, D. D. & Kane, E. O. Piezoreflectance of Germanium from 1.9 to 2.8 eV. *Physical Review* **185,** 1103–1114. (2023) (Sept. 15, 1969).

95. Rönnow, D., Lastras-Mart´, L. F., Cardona, M. & Santos, P. V. Determination of the Piezo-Optical Properties of Semiconductors above the Fundamental Gap by Means of Reflectance Difference Spectroscopy. *JOSA A* **16,** 568–573. ISSN: 1520-8532. (2023) (Mar. 1, 1999).

96. Mori, T., Kumagai, N., Hanada, T., Yao, T. & Yasuda, T. Measurements of a Component of the Piezo-Optic Tensor of Si by Reflectance Difference Spectroscopy. *Journal of Applied Physics* **94,** 1458–1460. ISSN: 0021-8979, 1089-7550. (2023) (Aug. 2003).

97. Rönnow, D., Cardona, M. & Lastras-Martínez, L. F. Piezo-Optical Coefficients of ZnSe and ZnTe above the Fundamental Gap. *Physical Review B* **59,** 5581–5590. ISSN: 0163-1829, 1095-3795. (2023) (Feb. 15, 1999).

98. Yang, Z. *et al.* Determination of Interface Layer Strain of Si/SiO2 Interfaces by Reflectance Difference Spectroscopy. *Applied Physics Letters* **71,** 87–89. ISSN: 0003-6951. (2023) (July 7, 1997).

99. Liarokapis, E., Papadimitriou, D., Rumberg, J. & Richter, W. Raman and RAS Measurements on Uniaxially Strained Thin Semiconductor Layers. *physica status solidi (b)* **211,** 309–316. ISSN: 1521-3951. (2023) (1999).

100. Lastras-Martínez, L. F., Chavira-Rodríguez, M., Balderas-Navarro, R. E., Flores-Camacho, J. M. & Lastras-Martínez, A. Reflectance Difference Spectroscopy of GaAs (001) under a [110] Uniaxial Stress. *Physical Review B* **70,** 035306. ISSN: 1098-0121, 1550-235X. (2023) (July 15, 2004).

101. Lastras-Martínez, L. F. *et al.* Effect of Reconstruction-Induced Strain on the Reflectance Difference Spectroscopy of GaAs (001) around E 1 and E 1 + Δ 1 Transitions. *Physical Review B* **75,** 235315. ISSN: 1098-0121, 1550-235X. (2023) (June 13, 2007).

102. Hingerl, K., Balderas-Navarro, R. E., Hilber, W., Bonanni, A. & Stifter, D. Surface-Stress-Induced Optical Bulk Anisotropy. *Physical Review B* **62,** 13048–13052. issn: 0163-1829, 1095-3795. (2023) (Nov. 15, 2000).

103. Balderas-Navarro, R. E., Hingerl, K., Bonanni, A., Sitter, H. & Stifter, D. In Situ Observation of Stress Relaxation in CdTe/ZnTe Heterostructures by Reflectance-Difference Spectroscopy. *Applied Physics Letters* **78,** 3615–3617. issn: 0003-6951. (2023) (June 4, 2001).

104. Hingerl, K., Balderas-Navarro, R. E., Bonanni, A. & Stifter, D. Influence of Anisotropic In-Plane Strain on Critical Point Resonances in Reflectance Difference Data. *Journal of Vacuum Science & Technology B: Microelectronics and Nanometer Structures* **19,** 1650. issn: 0734211X. (2023) (2001).

105. Molina_C, J. R. & Espinosa-Luna, R. Reflectance-Difference Study near the E1 and E1 + Δ1 Transition Regions of CdTe. *Journal of Physics D: Applied Physics* **38,** 12. issn: 0022-3727. (2023) (Dec. 2004).

106. Bennett, B. R. *et al.* Origin of Optical Anisotropy in Strained InxGa1-xAs/InP and InyAl1-yAs/InP Heterostructures. *Journal of Electronic Materials* **23,** 423–429. issn: 1543-186X. (2023) (Apr. 1, 1994).

107. Tang, C. G., Chen, Y. H., Ye, X. L., Wang, Z. G. & Zhang, W. F. Strain-Induced in-Plane Optical Anisotropy in (001) GaAs/AlGaAs Superlattice Studied by Reflectance Difference Spectroscopy. *Journal of Applied Physics* **100,** 113122. issn: 0021-8979. (2023) (Dec. 2006).

108. Etchegoin, P., Kircher, J., Cardona, M. & Grein, C. Piezo-Optical Response of Ge in the Visible–Uv Range. *Physical Review B* **45,** 11721–11735. (2023) (May 15, 1992).

109. Danzer, R. On the Relationship between Ceramic Strength and the Requirements for Mechanical Design. *Journal of the European Ceramic Society* **34,** 3435–3460. issn: 0955-2219. (2023) (Dec. 1, 2014).

110. Rönnow, D., Santos, P., Cardona, M., Anastassakis, E. & Kuball, M. Piezo-Optics of InP in the Visible-Ultraviolet Range. *Physical Review B* **57,** 4432–4442. issn: 0163-1829, 1095-3795. (2023) (Feb. 15, 1998).

111. Guerrisi, M., Rosei, R. & Winsemius, P. Splitting of the Interband Absorption Edge in Au. *Physical Review B* **12,** 557–563. (2023) (July 15, 1975).

112. Ngoc, L. L. T., Wiedemair, J., van den Berg, A. & Carlen, E. T. Plasmon-Modulated Photoluminescence from Gold Nanostructures and Its Dependence on Plasmon Resonance, Excitation Energy, and Band Structure. *Optics Express* **23,** 5547. issn: 1094-4087. (2023) (Mar. 9, 2015).

113. Blackford, J. R. *et al.* RAS as a Remote Sensor of Plastic Deformation in Metals. *physica status solidi (c)* **2,** 3997–4002. ISSN: 1610-1642. (2023) (2005).

114. Wyss, A. *Reflectance Anisotropy Spectroscopy as a Tool for Thin Film Characterization* Doctoral Thesis (ETH Zurich, 2017). (2023).

115. Ames, M., Markmann, J. & Birringer, R. Mechanical Testing via Dominant Shear Deformation of Small-Sized Specimen. *Materials Science and Engineering: A. Special Topic Section: Local and Near Surface Structure from Diffraction* **528,** 526–532. ISSN: 0921-5093. (2023) (Nov. 25, 2010).

116. Bassoli, L., Nizzoli, F. & Sandercock, J. R. Surface Brillouin Scattering in Polycrystalline Gold. *Physical Review B* **34,** 1296–1299. (2023) (July 15, 1986).

117. Xia, Z. C. & Hutchinson, J. W. Crack Patterns in Thin Films. *Journal of the Mechanics and Physics of Solids* **48,** 1107–1131. ISSN: 0022-5096. (2023) (June 1, 2000).

118. Beuth, J. L. Cracking of Thin Bonded Films in Residual Tension. *International Journal of Solids and Structures* **29,** 1657–1675. ISSN: 0020-7683. (2023) (Jan. 1, 1992).

119. Hao, Z., Kochubei, S. A., Popov, A. A. & Volodin, V. A. On Raman Scattering Cross Section Ratio of Amorphous to Nanocrystalline Germanium. *Solid State Communications* **313,** 113897. ISSN: 0038-1098. (2023) (June 1, 2020).

120. Donovan, T. M., Spicer, W. E., Bennett, J. M. & Ashley, E. J. Optical Properties of Amorphous Germanium Films. *Physical Review B* **2,** 397–413. ISSN: 0556-2805. (2023) (July 15, 1970).

121. Connell, G., Temkin, R. & Paul, W. Amorphous Germanium III. Optical Properties. *Advances in Physics* **22,** 643–665. ISSN: 0001-8732, 1460-6976. (2023) (Sept. 1973).

122. Kamiya, I., Aspnes, D. E., Florez, L. T. & Harbison, J. P. Reflectance-Difference Spectroscopy of (001) GaAs Surfaces in Ultrahigh Vacuum. *Physical Review B* **46,** 15894–15904. (2023) (Dec. 15, 1992).

123. Esser, N. *et al.* Optical Resonances of Indium Islands on GaAs(001) Observed by Reflectance Anisotropy Spectroscopy. *Physical Review B* **67,** 125306. ISSN: 0163-1829, 1095-3795. (2023) (Mar. 17, 2003).

124. Westwood, D. I., Sobiesierski, Z., Steimetz, E., Zettler, T. & Richter, W. On the Development of InAs on GaAs(001) as Measured by Reflectance Anisotropy Spectroscopy: Continuous and Islanded Films. *Applied Surface Science* **123–124,** 347–351. ISSN: 0169-4332. (2023) (Jan. 1, 1998).

125. Flores-Camacho, J. M. *et al.* In-Situ Characterization of Metal Clusters Supported on a Birefringent Substrate Using Reflectance Difference Spectroscopy. *Applied Physics A* **98,** 499–507. ISSN: 1432-0630. (2023) (Mar. 1, 2010).

126. Flores-Camacho, J. M. *et al.* Optical Anisotropies of Metal Clusters Supported on a Birefringent Substrate. *Physical Review B* **78,** 075416. (2023) (Aug. 13, 2008).

127. Flores-Camacho, J. M. *et al.* Growth and Optical Properties of Ag Clusters Deposited on Poly(Ethylene Terephthalate). *Nanotechnology* **22,** 275710. ISSN: 0957-4484. (2023) (May 2011).

128. Murray, W. A. & Barnes, W. L. Plasmonic Materials. *Advanced Materials* **19,** 3771–3782. ISSN: 1521-4095. (2023) (2007).

129. Naik, G. V., Shalaev, V. M. & Boltasseva, A. Alternative Plasmonic Materials: Beyond Gold and Silver. *Advanced Materials* **25,** 3264–3294. ISSN: 1521-4095. (2023) (2013).

130. Sun, L. D., Hohage, M., Zeppenfeld, P., Deisl, C. & Bertel, E. Reflectance Difference Spectroscopy Study of Ag Growth on W(110). *Surface Science* **600,** L281–L285. ISSN: 0039-6028. (2023) (Oct. 15, 2006).

131. Steimetz, E., Schienle, F., Zettler, J. .-. & Richter, W. Stranski-Krastanov Formation of InAs Quantum Dots Monitored during Growth by Reflectance Anisotropy Spectroscopy and Spectroscopic Ellipsometry. *Journal of Crystal Growth. Metalorganic Vapour Phase Epitaxy 1996* **170,** 208–214. ISSN: 0022-0248. (2023) (Jan. 1, 1997).

132. Denk, R. *et al.* Exciton-Dominated Optical Response of Ultra-Narrow Graphene Nanoribbons. *Nature Communications* **5,** 4253. ISSN: 2041-1723. (2023) (1 July 8, 2014).

133. Chandola, S. *et al.* Optical and Electronic Properties of Ag Nanodots on Si(111). *Journal of Physics: Condensed Matter* **18,** 6979. ISSN: 0953-8984. (2023) (July 2006).

134. Ualibek, O. *et al.* Manipulating and Probing the Growth of Plasmonic Nanoparticle Arrays Using Light. *Nanoscale* **5,** 4923–4930. (2023) (2013).

135. Verre, R. *et al.* Controlled in Situ Growth of Tunable Plasmonic Self-Assembled Nanoparticle Arrays. *Nanotechnology* **23,** 035606. ISSN: 0957-4484. (2023) (Dec. 2011).

136. Verre, R., Fleischer, K., Ualibek, O. & Shvets, I. V. Self-Assembled Broadband Plasmonic Nanoparticle Arrays for Sensing Applications. *Applied Physics Letters* **100,** 031102. ISSN: 0003-6951. (2023) (Jan. 16, 2012).

137. Verre, R. *et al. In Situ* Characterization of One-Dimensional Plasmonic Ag Nanocluster Arrays. *Physical Review B* **83,** 125432. ISSN: 1098-0121, 1550-235X. (2023) (Mar. 30, 2011).

138. Verre, R. *et al.* Polarization Conversion-Based Molecular Sensing Using Anisotropic Plasmonic Metasurfaces. *Nanoscale* **8,** 10576–10581. (2023) (2016).

139. Park, Y., Kim, J., Roh, Y.-G. & Park, Q.-H. Optical Slot Antennas and Their Applications to Photonic Devices. *Nanophotonics* **7,** 1617–1636. ISSN: 2192-8614. (2023) (Oct. 1, 2018).

140. Hrtoň, M., Konečná, A., Horák, M., Šikola, T. & Křápek, V. Plasmonic Antennas with Electric, Magnetic, and Electromagnetic Hot Spots Based on Babinet's Principle. *Physical Review Applied* **13,** 054045. (2023) (May 19, 2020).

141. Horák, M. *et al.* Limits of Babinet's Principle for Solid and Hollow Plasmonic Antennas. *Scientific Reports* **9,** 4004. ISSN: 2045-2322. (2023) (1 Mar. 8, 2019).

142. McPeak, K. M. *et al.* Plasmonic Films Can Easily Be Better: Rules and Recipes. *ACS Photonics* **2,** 326–333. (2023) (Mar. 18, 2015).

143. Fu, Y. H., Kuznetsov, A. I., Miroshnichenko, A. E., Yu, Y. F. & Luk'yanchuk, B. Directional Visible Light Scattering by Silicon Nanoparticles. *Nature Communications* **4,** 1527. ISSN: 2041-1723. (2023) (1 Feb. 26, 2013).

144. Timpu, F. *et al.* Lithium Niobate Nanocubes as Linear and Nonlinear Ultraviolet Mie Resonators. *ACS Photonics* **6,** 545–552. (2023) (Feb. 20, 2019).

145. Chen, W. T. *et al.* A Broadband Achromatic Metalens for Focusing and Imaging in the Visible. *Nature Nanotechnology* **13,** 220–226. ISSN: 1748-3395. (2023) (3 Mar. 2018).

146. Yu, N. & Capasso, F. Flat Optics with Designer Metasurfaces. *Nature Materials* **13,** 139–150. ISSN: 1476-4660. (2023) (2 Feb. 2014).

147. Yu, N. *et al.* Flat Optics: Controlling Wavefronts With Optical Antenna Metasurfaces. *IEEE Journal of Selected Topics in Quantum Electronics* **19,** 4700423–4700423. ISSN: 1558-4542 (May 2013).

148. Fleischer, K. *et al.* Reflectance Anisotropy Spectroscopy of Magnetite (110) Surfaces. *Physical Review B* **89,** 195118. (2023) (May 13, 2014).

149. Shioda, R. & van der Weide, J. Reflectance Difference Spectroscopy of Highly Oriented (2x1) Reconstructed Si(001) Surfaces. *Physical Review B* **57,** R6823–R6825. (2023) (Mar. 15, 1998).

150. Scholz, S. M., Jacobi, K., Zettler, J. .-. & Richter, W. Reflectance Anisotropy Spectroscopy on the Ge(113) Surface. *Surface Science* **359,** 205–212. ISSN: 0039-6028. (2023) (July 1, 1996).

151. Kamiya, I., Aspnes, D. E., Florez, L. T. & Harbison, J. P. Reflectance-Difference Spectroscopy of (001) GaAs Surfaces in Ultrahigh Vacuum. *Physical Review B* **46,** 15894–15904. (2023) (Dec. 15, 1992).

152. Hofmann, P., Rose, K. C., Fernandez, V., Bradshaw, A. M. & Richter, W. Study of Surface States on Cu(110) Using Optical Reflectance Anisotropy. *Physical Review Letters* **75,** 2039–2042. ISSN: 0031-9007, 1079-7114. (2023) (Sept. 4, 1995).

153. Martin, D. S., Blanchard, N. P. & Weightman, P. Reflection Anisotropy Spectroscopy of the Pd/Au(110)-$(1x2)$ Surface Alloy. *Physical Review B* **69,** 113409. (2023) (Mar. 24, 2004).

154. Herrmann, T. *et al.* Optical Reflectance Anisotropy of Al(110): Experiment and *Ab Initio* Calculation. *Physical Review B* **69,** 165406. ISSN: 1098-0121, 1550-235X. (2023) (Apr. 19, 2004).

155. Borensztein, Y., Mochan, W. L., Tarriba, J., Barrera, R. G. & Tadjeddine, A. Large Anisotropy in the Optical Reflectance of Ag(110) Single Crystals: Experiment and Theory. *Physical Review Letters* **71,** 2334–2337. (2023) (Oct. 4, 1993).

156. Stahrenberg, K. *et al.* Surface-State Contribution to the Optical Anisotropy of Ag(110) Surfaces: A Reflectance-Anisotropy-Spectroscopy and Photoemission Study. *Physical Review B* **58,** R10207–R10209. (2023) (Oct. 15, 1998).

157. Martin, D. S., Barrett, S. D. & Weightman, P. Reflection Anisotropy Spectroscopy of Clean and Adsorbate-Covered Ni(110) Surfaces. *Journal of Physics: Condensed Matter* **13,** 9847. ISSN: 0953-8984. (2023) (Oct. 2001).

158. Sun, L. D., Hohage, M. & Zeppenfeld, P. Oxygen-Induced Reconstructions of Cu(110) Studied by Reflectance Difference Spectroscopy. *Physical Review B* **69,** 045407. ISSN: 1098-0121, 1550-235X. (2023) (Jan. 15, 2004).

159. Sun, L. D., Hohage, M., Zeppenfeld, P., Balderas-Navarro, R. E. & Hingerl, K. Surface-Induced d-Band Anisotropy on Cu(110). *Surface Science* **527,** L184–L190. ISSN: 0039-6028. (2023) (Mar. 10, 2003).

160. Stahrenberg, K., Herrmann, T., Esser, N. & Richter, W. Surface Optical Properties of Clean Cu(110) and Cu(110)- (2×1) -O. *Physical Review B* **61,** 3043–3047. ISSN: 0163-1829, 1095-3795. (2023) (Jan. 15, 2000).

161. Monachesi, P., Palummo, M., Del Sole, R., Ahuja, R. & Eriksson, O. Reflectance Anisotropy Spectra of Cu and Ag (110) Surfaces from *Ab Initio* Theory. *Physical Review B* **64,** 115421. ISSN: 0163-1829, 1095-3795. (2023) (Aug. 30, 2001).

162. Sun, L. D., Hohage, M., Zeppenfeld, P. & Balderas-Navarro, R. E. Origin and Temperature Dependence of the Surface Optical Anisotropy on Cu(110). *Surface Science* **589,** 153–163. ISSN: 0039-6028. (2023) (Sept. 1, 2005).

163. Hansen, J. .-., Bremer, J. & Hunderi, O. The Electronic Structure of Cu(110) and Ag(110) Surfaces Studied by Reflection Anisotropy Spectroscopy. *Surface Science* **418,** L58–L61. ISSN: 0039-6028. (2023) (Dec. 5, 1998).

164. Hansen, J.-K., Bremer, J. & Hunderi, O. Local-Field Effects at the Ag(110) and Cu(110) Surfaces Studied by Reflection Anisotropy Spectroscopy. *physica status solidi (a)* **170,** 271–277. ISSN: 1521-396X. (2023) (1998).

165. Sun, L. D., Hohage, M. & Zeppenfeld, P. Optical Probe for Surface and Subsurface Defects Induced by Ion Bombardment. *physica status solidi (RRL) – Rapid Research Letters* **7,** 301–304. ISSN: 1862-6270. (2023) (2013).

166. Sun, L. D., Hohage, M., Zeppenfeld, P., Balderas-Navarro, R. E. & Hingerl, K. Strain Oscillations Probed with Light. *Physical Review Letters* **96,** 016105. ISSN: 0031-9007, 1079-7114. (2023) (Jan. 5, 2006).

167. Oudah, M. H., Hasan, M. H. & Abd, A. N. Synthesis of Copper Oxide Thin Films by Electrolysis Method Based on Porous Silicon for Solar Cell Applications. *IOP Conference Series: Materials Science and Engineering* **757,** 012051. ISSN: 1757-8981, 1757-899X. (2023) (Mar. 1, 2020).

168. Baumberger, F. *et al.* Optical Recognition of Atomic Steps on Surfaces. *Physical Review Letters* **90,** 177402. ISSN: 0031-9007, 1079-7114. (2023) (Apr. 29, 2003).

169. Denk, M. *et al.* Reflectance Difference Spectroscopy of Water on Cu(110). *Surface Science* **627,** 16–22. ISSN: 0039-6028. (2023) (Sept. 1, 2014).

170. Monachesi, P. & Chiodo, L. Optical Response of the Copper Surface to Carbon Monoxide Deposition. *Physical Review Letters* **93,** 116102. ISSN: 0031-9007, 1079-7114. (2023) (Sept. 10, 2004).

171. Sun, L. D., Hohage, M., Zeppenfeld, P., Balderas-Navarro, R. E. & Hingerl, K. Enhanced Optical Sensitivity to Adsorption Due to Depolarization of Anisotropic Surface States. *Physical Review Letters* **90,** 106104. (2023) (Mar. 13, 2003).

172. Sun, L. D. *et al.* Optical Characterization of Methanol Adsorption on the Bare and Oxygen Precovered Cu(110) Surface. *Surface Science* **604,** 824–828. ISSN: 0039-6028. (2023) (May 15, 2010).

173. Johnson, P. B. & Christy, R. W. Optical Constants of the Noble Metals. *Physical Review B* **6,** 4370–4379. (2023) (Dec. 15, 1972).

174. Macdonald, B. F., Law, J. S. & Cole, R. J. Azimuth-Dependent Reflection Anisotropy Spectroscopy. *Journal of Applied Physics* **93,** 3320–3327. ISSN: 0021-8979. (2023) (Mar. 5, 2003).

175. Vaudin, M. D., Gerbig, Y. B., Stranick, S. J. & Cook, R. F. Comparison of Nanoscale Measurements of Strain and Stress Using Electron Back Scattered Diffraction and Confocal Raman Microscopy. *Applied Physics Letters* **93,** 193116. ISSN: 0003-6951. (2023) (Nov. 13, 2008).

176. Tamura, N. *et al.* High Spatial Resolution Grain Orientation and Strain Mapping in Thin Films Using Polychromatic Submicron X-Ray Diffraction. *Applied Physics Letters* **80,** 3724–3726. ISSN: 0003-6951, 1077-3118. (2023) (May 20, 2002).

177. Tamura, N. *et al.* Submicron X-Ray Diffraction and Its Applications to Problems in Materials and Environmental Science. *Review of Scientific Instruments* **73,** 1369–1372. ISSN: 0034-6748. (2023) (Mar. 1, 2002).

178. Pfeifer, M. A., Williams, G. J., Vartanyants, I. A., Harder, R. & Robinson, I. K. Three-Dimensional Mapping of a Deformation Field inside a Nanocrystal. *Nature* **442,** 63–66. ISSN: 1476-4687. (2023) (7098 July 2006).

179. Cornelius, T. W. & Thomas, O. Progress of in Situ Synchrotron X-ray Diffraction Studies on the Mechanical Behavior of Materials at Small Scales. *Progress in Materials Science* **94,** 384–434. ISSN: 0079-6425. (2023) (May 1, 2018).

180. Miao, J., Sandberg, R. L. & Song, C. Coherent X-Ray Diffraction Imaging. *IEEE Journal of Selected Topics in Quantum Electronics* **18,** 399–410. ISSN: 1558-4542 (Jan. 2012).

181. Sandberg, R. L. *et al.* High Numerical Aperture Tabletop Soft X-Ray Diffraction Microscopy with 70-Nm Resolution. *Proceedings of the National Academy of Sciences* **105,** 24–27. (2023) (Jan. 8, 2008).

182. Silies, M. *et al.* Table-Top kHz Hard X-ray Source with Ultrashort Pulse Duration for Time-Resolved X-ray Diffraction. *Applied Physics A* **96,** 59–67. ISSN: 1432-0630. (2023) (July 1, 2009).

183. Ohnuma, M. *et al.* Structural Anisotropy of Amorphous Alloys with Creep-Induced Magnetic Anisotropy. *Acta Materialia* **60,** 1278–1286. ISSN: 1359-6454. (2023) (Feb. 1, 2012).

184. Chen, D., Kuo, J.-C. & Wu, W.-T. Effect of Microscopic Parameters on EBSD Spatial Resolution. *Ultramicroscopy* **111,** 1488–1494. ISSN: 0304-3991. (2023) (Aug. 1, 2011).

185. Keller, R. & Geiss, R. Transmission EBSD from 10 Nm Domains in a Scanning Electron Microscope. *Journal of Microscopy* **245,** 245–251. ISSN: 1365-2818. (2023) (2012).

186. Wilkinson, A. J., Britton, T. B., Jiang, J. & Karamched, P. S. A Review of Advances and Challenges in EBSD Strain Mapping. *IOP Conference Series: Materials Science and Engineering* **55,** 012020. ISSN: 1757-899X. (2023) (Mar. 2014).

187. Wilkinson, A. J. & Britton, T. B. Strains, Planes, and EBSD in Materials Science. *Materials Today* **15,** 366–376. ISSN: 1369-7021. (2023) (Sept. 1, 2012).

188. Britton, T. B. *et al.* Factors Affecting the Accuracy of High Resolution Electron Backscatter Diffraction When Using Simulated Patterns. *Ultramicroscopy* **110,** 1443–1453. ISSN: 0304-3991. (2023) (Nov. 1, 2010).

189. Zhu, C., Kaufmann, K. & Vecchio, K. S. Novel Remapping Approach for HR-EBSD Based on Demons Registration. *Ultramicroscopy* **208,** 112851. ISSN: 0304-3991. (2023) (Jan. 1, 2020).

190. Alkorta, J. Limits of Simulation Based High Resolution EBSD. *Ultramicroscopy* **131,** 33–38. ISSN: 0304-3991. (2023) (Aug. 1, 2013).

191. Darbal, A. D. *et al.* Applications of Automated High Resolution Strain Mapping in TEM on the Study of Strain Distribution in MOSFETs. *Microscopy and Microanalysis* **20,** 1066–1067. ISSN: 1431-9276, 1435-8115. (2023) (Aug. 2014).

192. Hÿtch, M. J. & Minor, A. M. Observing and Measuring Strain in Nanostructures and Devices with Transmission Electron Microscopy. *MRS Bulletin* **39,** 138–146. ISSN: 0883-7694, 1938-1425. (2023) (Feb. 2014).

193. Sarker, I. H. Machine Learning: Algorithms, Real-World Applications and Research Directions. *SN Computer Science* **2,** 160. ISSN: 2661-8907. (2023) (Mar. 22, 2021).

194. Shrestha, A. & Mahmood, A. Review of Deep Learning Algorithms and Architectures. *IEEE Access* **7,** 53040–53065. ISSN: 2169-3536 (2019).

195. Zhu, Y. & Huang, C. An Improved Median Filtering Algorithm for Image Noise Reduction. *Physics Procedia. International Conference on Solid State Devices and Materials Science, April 1-2, 2012, Macao* **25,** 609–616. ISSN: 1875-3892. (2023) (Jan. 1, 2012).

196. Oliveira, E., Strassner, J., Doering, C. & Fouckhardt, H. Reflectance Anisotropy Spectroscopy (RAS) for in-Situ Identification of Roughness Morphologies Evolving during Reactive Ion Etching (RIE). *Applied Surface Science* **611,** 155769. ISSN: 0169-4332. (2023) (Feb. 15, 2023).

197. Jiles, D. C. & Staines, M. P. Piezo Optic Properties of Aluminum. *Solid State Communications* **47,** 37–41. ISSN: 0038-1098. (2023) (July 1, 1983).

198. Photonics Optics and, F.-T. N. W. t. F. L. *SuperK EXTREME Supercontinuum Lasers - EXW-12* `https://www.findlight.net/lasers/fiber-lasers/broadband-supercontinuum-sources/superk-extreme-supercontinuum-lasers-exw-12` (2023).

199. Núñez-Olvera, O. *et al.* A Rapid Reflectance-Difference Spectrometer for Real-Time Semiconductor Growth Monitoring with Sub-Second Time Resolution. *Review of Scientific Instruments* **83,** 103109. ISSN: 0034-6748. (2023) (Oct. 25, 2012).

200. Khoshnoud, F. & de Silva, C. W. Recent Advances in MEMS Sensor Technology – Biomedical Applications. *IEEE Instrumentation & Measurement Magazine* **15,** 8–14. ISSN: 1941-0123 (Feb. 2012).

201. Yeow, T.-W., Law, K. & Goldenberg, A. MEMS Optical Switches. *IEEE Communications Magazine* **39,** 158–163. ISSN: 1558-1896 (Nov. 2001).

202. Dong, Y., Zwahlen, P., Nguyen, A. M., Frosio, R. & Rudolf, F. *Ultra-High Precision MEMS Accelerometer* in *2011 16th International Solid-State Sensors, Actuators and Microsystems Conference* 2011 16th International Solid-State Sensors, Actuators and Microsystems Conference (June 2011), 695–698.

203. Iannacci, J. Reliability of MEMS: A Perspective on Failure Mechanisms, Improvement Solutions and Best Practices at Development Level. *Displays. Advanced MEMS Technologies and Displays* **37,** 62–71. ISSN: 0141-9382. (2023) (Apr. 1, 2015).

204. Skogström, L., Li, J., Mattila, T. T. & Vuorinen, V. in *Handbook of Silicon Based MEMS Materials and Technologies* 851–876 (Elsevier, 2020). ISBN: 978-0-12-817786-0. (2023).

Declaration

This thesis has been an exciting collaborative effort and the following list gratefully acknowledges the contributions of

Prof. Ralph Spolenak is a professor at ETH Zurich and head of the Laboratory for Nanometallurgy. He supervised this thesis.

Dr. Henning Galinski milled the nanoantennas with FIB and helped in the proceeding simulations.

Dr. Micha Calvo fabricated the template stripped gold films.

Fabian Haake fabricated and measured the non-templated stripped gold films with milled structures and the amorphous germanium films.

Jose Ocaña performed XRD on the amorphous germanium films.

Fabian Bill fabricated the single crystal copper samples in Chapter 7 and subsequently performed the RAS measurements.

Nerea Abando aided in the mechanical polishing of the copper plates and performed the EBSD scans of the copper films.

Dr. Karsten Kunze performed the EBSD maps of the copper plates.

Dr. Marco Volpi performed the EBSD scans for the copper single crystals.

List of Abbreviations

ADRAS	Azimuth Dependent Reflectance Anisotropy Spectroscopy
AFM	Atomic Force Microscopy
CCD	Charged Coupled Device
EBSD	Electron Backscattered Diffraction
eV	electronvolts
FCC	Face Centered Cubic
FEM	Finite Element Modelling
FIB	Focused Ion Beam
LCVR	Liquid Crystal Variable Retarder
LSPR	Localized Surface Plasmon Resonance
MEMS	Micro electro-mechanical systems
NA	Numerical Aperture
NIR	Near Infrared
PEM	Photoelastic Modulator
PMT	Photomultiplier Tube
PSF	Point Spread Function
PVD	Physical Vapor Deposition
RAS	Reflectance Anisotropy Spectroscopy
SEM	Scanning Electron Microscopy
SRAM	Scanning Reflectance Anisotropy Microscope/-y
STM	Scanning Tunneling Microscopy

TEM	Transmission Electron microscopy
UHV	Ultra High Vacuum
UV	Ultra-Violet
XRD	X-Ray Diffraction

List of Figures

1.1 Proposed RAS microscopy setup design 3

2.1 Schematic of a typical RAS setup 6
2.2 Modes of nanorod antennas and length dependence of the resonance frequency 12
2.3 Gap influence on the resonance frequency of nanorod dimer antennas 13
2.4 Babinet's principle for optical nanoantennas 14

4.1 Modulus of the Fresnel reflectance coefficients for gold at 2.44 eV 19

4.2 Calculation of the RAS signal at the focal plane after an objective lens 20
4.3 μRAS setups overview 21
4.4 LCVR RAS as a function of NA 23
4.5 SRAM setup picture and diagram 26
4.6 Artefacts and noise characterization 28
4.7 Effect of calibration on the spectral line shape of SRAM 30
4.8 PSF of the SRAM setup measured by scanning a nanoantenna . 31
4.9 Influence of a step on a μRAS setup 32
4.10 Influence of step height on the RAS signal of a step edge 33
4.11 SRAM scan of an ellipse showing the step influence 34
4.12 Origin of the RAS signal induced by and edge and the inferred lineshape. 35
4.13 Spectral line scan over an ellipse edge on a 50 nm gold film with a 50x objective 36
4.14 Edge profile of ellipse as a function of magnification 37
4.15 Roughness influence of a 50 nm gold film sputtered on silicon. . 38
4.16 Roughness influence of a polished copper plate with $\tau \gtrsim \lambda$. . . . 39
4.17 Hyperspectral scan of a rough copper surface with $\tau \gtrsim \lambda$ 40

5.1 Piezo-optic tensor of germanium 42
5.2 RAS signal of gold as a function of strain 43
5.3 Strain mapping on polished GaSb 44
5.4 Schematic of the germanium suspended bridges lithographic fabrication 45
5.5 SRAM spectra of germanium as a function of strain 46
5.6 Strain map of germanium 46

5.7 Strain profile of a suspended germanium microbridge 47
5.8 SRAM signal of a gold film as a function of strain 49
5.9 Offset correction term as a function of strain 50
5.10 Strain mapping in gold 51
5.11 XRD and Raman measurements of an a-ge film 53
5.12 RAS signal of amorphous germanium as a function of strain . . 53
5.13 Refractive index of amorphous germanium 54
5.14 Strain mapping in amorphous germanium 55

6.1 Calculated signal for grown Ag nanoparticles 58
6.2 TAS of gold dimer antennas 59
6.3 FEM simulations of babinet nanoslot antennas 60
6.4 SRAM spectrum of Babinet nanoslot antennas 61
6.5 Comparison SRAM spectra between template stripped and as deposited 62
6.6 Angular dependence of the SRAM signal of an array of nanoslot antennas 64
6.7 Single antenna sensitivity 64
6.8 SRAM spectra as a function of array size 65
6.9 SRAM spectra for two different antenna lengths 66
6.10 SRAM spectra of strained antennas 67
6.11 SRAM map of a metasurface 69

7.1 Influence of oxide reconstruction on the RAS signal of Cu (110) surfaces 72
7.2 Influence of roughness on the RAS signal of Cu (110) surfaces . 74
7.3 RAS spectra of Cu (112) and Cu (221) facets 75
7.4 RAS signal of a single crystal in ambient air 77
7.5 EBSD and RAS data of a copper crystal close to (110) orientation 79
7.6 EBSD and RAS data of a copper grain in-between (110) and (111) out of plane orientation 82
7.7 SRAM map of a grain boundary at a copper plate 84
7.8 Histogram and grain distortion of a copper plate grain boundary 85
7.9 SEM and EBSD scans of an electroplated copper film on a flexible substrate 86
7.10 SRAM signal of an electroplated copper film on a flexible substrate 87

8.1 Strain sensitivity as a function of numerical aperture 90
8.2 Extension of the SRAM spectral range 95
8.3 Failure in MEMS 98

8.4 Strain sensitivity vs spatial resolution chart 99

Joan Sendra Garcia

Personal Data

Place and Date of Birth: Barcelona, Spain | 20 March 1993

Employment Experience

Jan 2018-Apr 2023	**Research Assistant at ETHZ, Switzerland**
May-Nov 2017	**Intership at Optotune, Switzerland**
Feb-Jul 2015	**Internship at ICFO - The Institute of Photonic Sciences, Spain**
Jul-Aug 2010	**Assistant Counsellor at YMCA Wanakita, Canada**

Education

2018-2023	*Ph.D. in Materials Science* **Eidgenössische Technische Hochschule Zürich (ETHZ)** - Ph.D. Thesis: "Towards multi-material strain and crystal orientation mapping with Scanning Reflectance Anisotropy Microscopy" in the Laboratory for Nanometallurgy under the supervision of Prof. Ralph Spolenak.
2015-2017	*Master in Physics* **Eidgenössische Technische Hochschule Zürich (ETHZ)** - Master Thesis: "Linear and nonlinear UV spectroscopy of hybrid nanostructures" in the Optical Nanomaterial Group under the supervision of Prof. Rachel Grange.
2011-2015	*Bachelor in Engineering Physics* **Universitat Politècnica de Catalunya (UPC)** - Bachelor Thesis: "Development of a scalable, point-of-care and label free microarray platform for rapid detection of sepsis" in the Optoelectronics Group under the supervision of Prof. Valerio Pruneri and Prof. José Trull.

Selected Scientific Contributions

- **Sendra, J.**, Haake, F., Calvo, M., Galinski, H., & Spolenak, R. (2023). Scanning Reflectance Anisotropy Microscopy for Multi-Material Strain Mapping. arXiv preprint arXiv:2302.04095. Under review in *Advanced Functional Materials.*
- Timpu, F., **Sendra, J.**, Renaut, C., Lang, L., Timofeeva, M., Buscaglia, M. T., ... & Grange, R. (2019). Lithium niobate nanocubes as linear and nonlinear ultraviolet Mie resonators. Acs Photonics, 6(2), 545-552.
- Mattich, I., **Sendra, J.**, Galinski, H., Isapour, G., Demirörs, A. F., Lattuada, M., ... & Studart, A. R. (2023). Magnetic manipulation of superparamagnetic colloids in droplet-based optical devices. arXiv preprint arXiv:2303.15336. Under review in *Advanced Optical Materials*
- **Sendra, J.**, Haake, F., Calvo, M., Galinski, H., Spolenak, R., "Multi-Material Differential Strain Mapping with Reflectance Anisotropy Spectroscopy Microscopy", Materials Research Society spring meeting, Honolulu 2022. **Contributed talk**
- **Sendra, J.**, Abando, N., Volpi, M., Galinski, H., Spolenak, R., "Micro reflectance anisotropy spectroscopy as a new tool for stress and crystal orientation mapping in thin films", Materials Research Society spring meeting, Seattle 2021. **Contributed talk**